ANL-12/33

Technical Letter Report of Slow-Strain-Rate Tensile Tests on Irradiated Stainless Steels in a PWR Environment

Nuclear Engineering Division

About Argonne National Laboratory

Argonne is a U.S. Department of Energy laboratory managed by UChicago Argonne, LLC under contract DE-AC02-06CH11357. The Laboratory's main facility is outside Chicago, at 9700 South Cass Avenue, Argonne, Illinois 60439. For information about Argonne, see http://www.anl.gov.

ANL-12/33

Technical Letter Report of Slow-Strain-Rate Tensile Tests on Irradiated Stainless Steels in a PWR Environment

Manuscript Completed: June 2012

Y. Chen, W. Soppet, B. Alexandreanu, and K. Natesan

Argonne National Laboratory, Argonne, IL 60439

A. S. Rao, Project Manager, U.S. Nuclear Regulatory Commission

This page is intentionally left blank.

Abstract

Slow-strain-rate tensile (SSRT) tests have been performed on irradiated specimens in a simulated pressurized water reactor (PWR) environment. The samples are miniature tensile specimens of various austenitic stainless steels (SSs) with different thermal-mechanical treatments commonly used for reactor core internal components. Neutron irradiation was carried out in the BOR-60 reactor, a sodium-cooled, fast breeder reactor in Russia, at ~320°C. The damage doses of the specimens are 5, 10, and 48 dpa (displacements per atom). All irradiated materials show significant irradiation hardening and loss of ductility in the SSRT tests. The yield strengths of cold-worked are higher than that of solution-annealed samples at all doses up to 48 dpa. While the irradiation hardening seems to saturate between ~5 and ~10 dpa, the loss of ductility continues to increase above 10 dpa. Strain softening is also observed for all irradiated materials above 5 dpa. Fractographic examinations show that ductile dimple fracture is the dominant morphology for all SSRT tests in the PWR environment. Small areas of transgranular, mixed-mode and cleavage fractures are seen on most fracture surfaces in PWR water tests. Intergranular cracking is also observed in 48-dpa Types 316 and 347 SSs. Cracking susceptibility of the tested materials was evaluated with fracture morphology and time to failure. In general, high-doses cold-worked SSs are more susceptible to transgranular cleavage cracking in the PWR environment. Solution-annealed Type 347 SS is susceptible to intergranular cracking at 45 dpa in the PWR environment.

This page is intentionally left blank.

Contents

This page is intentionally left blank.

Figures

Tables

This page is intentionally left blank.

Executive Summary

Exposed simultaneously to fast neutron bombardments and high-temperature water, reactor internal components made of stainless steels (SSs) are susceptible to irradiation-assisted stress corrosion cracking (IASCC). Service failures resulting from IASCC have been reported in both boiling water reactors and pressurized water reactors (PWRs). Irradiation-induced microstructural and microchemical changes, along with changes in water chemistry are believed to be responsible for IASCC. Because failures of major internal components could seriously impair the safe and economic operation of nuclear power plants, IASCC has become an increasingly important issue in recent years for license renewal and aging management.

In this study, slow-strain-rate tensile (SSRT) tests are performed on miniature tensile specimens in a simulated PWR environment at three doses (5, 10, 48 displacements per atom, dpa). The samples are miniature tensile specimens of various SSs commonly used in reactor internals. Solution-annealed, cold-worked and grain-boundary engineered materials are included in the study. The specimens are irradiated in the BOR-60 reactor, a sodium-cooled, fast breeder reactor located in the Research Institute of Atomic Reactor (RIAR) in Dimitrovgrad, Russia. During irradiation, the specimens were in direct contact with sodium coolant and the irradiation temperature was controlled by the inlet and outlet temperature, which were kept at 315°C and 325°C, respectively.

A total of 29 specimens from 15 materials were tested in a simulated PWR environment in this study. Several specimens were also tested in air atmosphere for reference. All SSRT tests were carried out in a hot-cell facility at Argonne National Laboratory. The tests were conducted at a constant strain rate of 7.4×10^{-7} s^{-1}. The simulated PWR environment was provided by a recirculation loop at a flow rate of 10-20 ml/min. The autoclave temperature is maintained at 315-320°C, and the pressure during the tests is between 1,750 and 1,800 psig. After each SSRT test, the fractured specimen was decontaminated and transferred to a lead-shielded scanning electronic microscope for fractographic examination. Using fracture morphology and time to failure, cracking susceptibility was assessed at three doses for different materials and thermal-mechanical treatments.

All SSRT curves and fractographic observations are analyzed in this report. The irradiated SSRT tests show significant hardening at all doses. The saturation of irradiation hardening appears to be below ~10 dpa. Using a dispersion hardening model, irradiation-induced strengthening observed in this study can be reasonably accounted for by faulted dislocation loops. Although little difference in irradiated yield strength can be seen between 10 and 48 dpa, the total elongation continues to decline slowly beyond 10 dpa. The effects of prior cold-work on strength and ductility remain unchanged after irradiation up to 48 dpa. In addition to irradiation-induced hardening, work-hardening capability also decreases considerably in the irradiation specimens. Above 10 dpa, work hardening is essentially absent among all tested materials. This stress-strain behavior contributes to irradiation embrittlement. Dislocation channeling is believed to be the micro-mechanism responsible for the loss of ductility.

Fractographic analyses of tested samples reveal that ductile dimple is the dominant fracture morphology for all SSRT tests in PWR water. Small areas of transgranular (TG) and cleavage cracking can be seen in most cold-worked and high-dose samples. Cleavage cracking seems to develop readily in most of the materials tested in this study. The observation of cleavage indicates severe irradiation embrittlement. Meanwhile, since many cleavage areas are located at the sample/water interfaces, an environmental contribution is also speculated. Intergranular (IG) cracking is observed in high-dose solution-annealed Types 316 and 347 SSs. Flow localization resulting from dislocation channeling seems to be crucial for IG cracking. Overall, the fraction of brittle fracture is low for these SSRT tests, suggesting a low cracking susceptibility of SSs in a PWR environment.

The cracking susceptibility of different materials and thermal-mechanical treatment is also evaluated with time to failure (TF). The values of TF vary considerably from one test to another. At a given dose, the TFs of Alloy 690 are higher than those of 304 and 316 SSs with a few exceptions. The TFs of 347 SS are among the lowest at each dose level. Despite a large variation among different materials, a general trend of declining TFs with increasing dose is evident. Solution-annealed samples also show longer TFs than cold-worked materials. A general trend of increasing susceptibility to cracking is found with increasing dose and cold-work.

Acknowledgments

The authors would like to thank Drs. O. K. Chopra, H. M. Chung and W. J. Shack for their invaluable contribution to this project. Special thanks also go to Drs. Raj Pathania and Peter Scott for arranging irradiation experiments through the Cooperative IASCC Research (CIR) program in the BOR-60 reactor. The authors would like to thank Dr. Regis P. Shogan of Westinghouse, Mr. Jenssen Anders of Studsvik Nuclear AB, and Ms. Miroslava Ernestova of Nuclear Research Institute Rez for transferring the irradiated specimens from Russia to Argonne National Laboratory. L. A. Knoblich, E. E. Gruber, R. Clark, and E. J. Listwan are acknowledged for their contributions to the experimental effort. We are also grateful to Drs. W. H. Cullen, Jr., R. Tregoning and S. Crane for many helpful discussions and suggestions. This work is sponsored by the Office of Nuclear Regulatory Research, U.S. Nuclear Regulatory Commission, under Job Code N6519; Program Manager: A. S. Rao.

This page is intentionally left blank.

Acronyms and Abbreviations

BWR	Boiling Water Reactor
CGR	Crack Growth Rate
CSL	Coincident Site Lattice
CW	Cold Worked
DO	Dissolved Oxygen
ECP	Electrochemical Potential
GBE	Grain-Boundary Engineered
HP	High Purity
HWC	Hydrogen Water Chemistry
IASCC	Irradiation-Assisted Stress Corrosion Cracking
IG	Intergranular
LWR	Light Water Reactor
NWC	Normal Water Chemistry
PWR	Pressurized Water Reactor
RIAR	Research Institute of Atomic Reactor
RA	Reduction of Area
RIS	Radiation-Induced Segregation
SA	Solution Annealed
SCC	Stress Corrosion Cracking
SEM	Scanning Electron Microscopy
SS	Stainless Steel
SSRT	Slow-Strain-Rate Tensile
TE	Total Elongation
TF	Time to failure
TEM	Transmission Electron Microscope
TG	Transgranular
UTS	Ultimate Tensile Strength
WW	Warm Worked
YS	Yield Strength

Units of Measure

cm	centimeter(s)
dpa	displacement(s) per atom
hr	hour(s)
kV	kilovolt(s)
lbs	pounds
meV	million electron volts
min	minute(s)
ml	milliliter
mm	millimeter
MPa	megapascal(s)
ppb	parts per billion
ppm	parts per million
psig	pounds per square inch gauge
s	second(s)
µ	micron

1 Introduction

Stress corrosion cracking (SCC) is one of the most important degradation mechanisms for reactor components in light water reactors (LWRs). A systematic analysis of power plant information conducted by NRC shows that approximately 40 percent of aging-related phenomena concerning reactor vessel, internals and piping systems involve SCC.[1] Exposed to fast neutron bombardments, internal components in reactor core regions are even more vulnerable to this form of environmental attack, leading to irradiation-assisted stress corrosion cracking (IASCC). Service failures resulting from IASCC have been reported in absorber tubes, core shrouds, and top guides in boiling water reactors (BWRs), and fuel cladding, control rod cladding, and baffle former bolts in pressurized water reactors (PWRs).[2-6] Because repair or replacement of structural components around the reactor core regions is extremely difficult and expensive, failures of major internal components could seriously impair the safe and economic operation of nuclear power plants. In recent years, as nuclear power plants age and accumulated neutron fluence increases, IASCC has become an increasingly important issue for license renewal and aging management of LWRs.

Neutron irradiation plays a key role in IASCC process, and nonsensitized stainless steels (SSs) can become susceptible to SCC after extended neutron exposure.[7] Irradiation-induced microstructural (e.g., radiation defects) and microchemical (e.g., radiation-induced segregation) changes, along with changes in water chemistry (e.g., radiolysis), are believed to be responsible for IASCC.[8-10] A sharp rise in cracking susceptibility has been observed above a dose of 0.75 displacements per atom (dpa, or 5×10^{20} n/cm^2, E>1 MeV) in BWRs, and 3 dpa (2×10^{21} n/cm^2, E>1 MeV) in PWRs.[11,12] In high dissolved-oxygen (DO) water, cracking has even been found at doses as low as 0.3 dpa (2×10^{20} n/cm^2, E>1 MeV).[13] Because of the complex nature of multi-variable dependence, an absolute dose limit for IASCC may be not justified.[10] Nonetheless, exposure to fast neutron irradiation is a critical condition for reducing the cracking resistance of nonsensitized SSs that would otherwise show excellent mechanical properties under normal conditions.

Thanks to a low corrosion potential of hydrogenated water environments, IASCC occurs at higher doses in PWR than in BWR environments. Similarly, crack growth rates (CGRs) in hydrogen water chemistry (HWC) have also been found much lower than that in normal water chemistry (NWC) in BWRs. This effect of corrosion potential has been widely reported for nonirradiated SSs, and has been explained within the framework of slip-dissolution theory.[6,14,15] The observation of a higher dose "threshold" for PWR environments seems to suggest that IASCC is on a continuum with SCC and may share a common dependence on a set of environmental variables with SCC.

In LWR environments, SCC is also sensitive to local metallurgical conditions at crack tip. Early mechanistic studies of IASCC focus on the depletion of Cr at grain boundaries and its influence on the passivity of SSs at crack tip. [9,16] Radiation-induced segregation (RIS) led to narrow Cr depletion zones at grain boundaries. The roles of impurity elements such as Si, P, and S on IASCC susceptibility have also been investigated. [6, 8] Chung et al. showed that, in a high-DO environment, S content contributes to the IASCC susceptibility in low-C SSs, but is less critical in high-C SSs. [13,17] Andersen and Morra also showed that Si segregation at grain boundaries may be critical for cracking susceptibility of cold-worked SSs.[18] Although a redistribution of impurities due to RIS does occur, clear correlations have not been found between the bulk concentration of impurities and IASCC susceptibility. No systematic study has been performed to test for the metallurgical variables on the IASCC susceptibility in low-potential environments (i.e. in HWC or PWR water).

More recently, Busby et al. [19] demonstrated that, in post-irradiation annealing tests, the reversal of IASCC susceptibility occurs much earlier than does the recovery of RIS. This "out-of-phase" annealing behavior suggested that small irradiation defects or defect clusters rather than RIS may be the controlling

variable for IASCC. Detailed analyses of the deformation mode of irradiated specimens further revealed that the development of localized plastic flow in irradiated materials is associated with an increased trend in IASCC susceptibility.[20] Was et al. suggested that localized deformation contributes to the rupture of the oxide film near grain boundaries, and therefore, may be a critical factor for IASCC susceptibility.[10,21] The higher dose "threshold" of IASCC in PWR seems to imply that localized plastic flow may play an even more important role in low-potential environments (e.g., HWC or PWR primary water environments). At present, the database for PWR internals is still very limited, and the key metallurgical variables for IASCC in the PWR environment have not been clearly identified. The exact mechanism operating under the PWR environment is not clear. A better mechanistic understanding of cracking in the PWR environment is crucial not only for establishing possible countermeasures to mitigate IASCC but also for developing a predictive and regulatory methodology.

In the current study, slow-strain-rate tensile (SSRT) tests are performed on miniature tensile specimens in a simulated PWR environment at three doses (5, 10, 48 dpa). The samples are various austenitic SSs with different thermal-mechanical treatments commonly used for the core internal components of PWRs. The SSRT results are used to access irradiation hardening and embrittlement under PWR-relevant conditions (e.g., dose, temperature, and environment). The cracking susceptibility of the tested materials is also evaluated as a function of dose, material chemistry, and thermal-mechanical treatments.

2 Experimental

2.1 Specimens and Materials

Slow-strain-rate tensile specimens used in this study are miniature coupon samples as shown in Fig. 1. The nominal dimensions for the sample are 0.3", 0.06" and 0.03" for gauge length, width, and thickness, respectively. Two loading pin holes of 0.08" diameter are drilled on sample shoulders. The overall length of the sample is about 1".

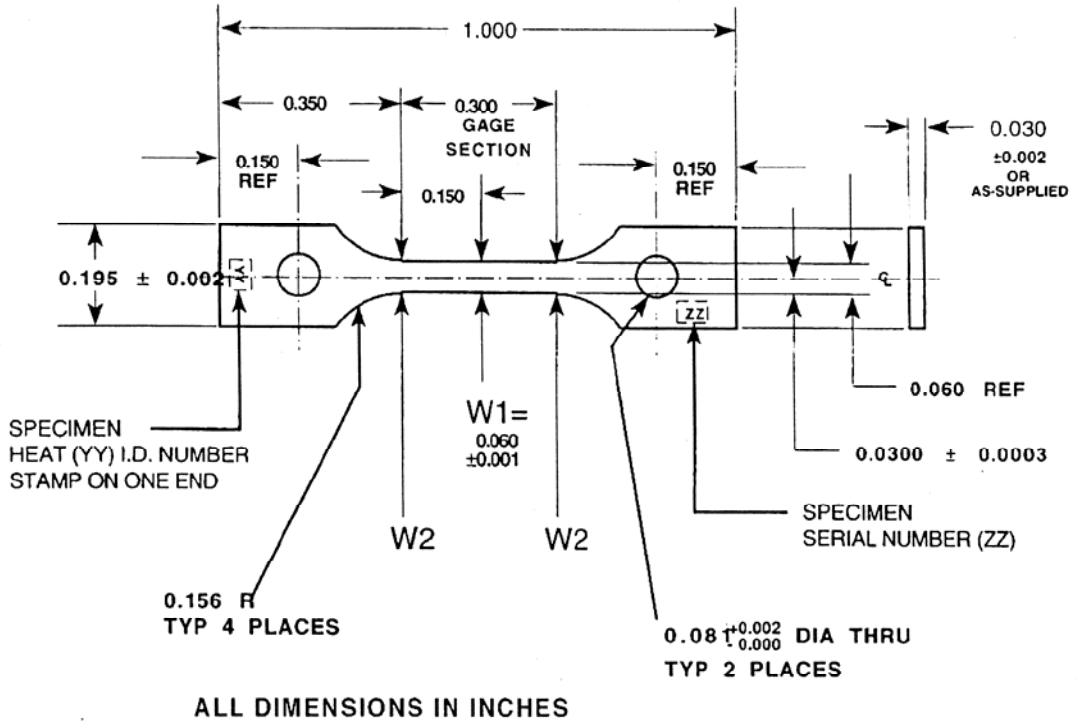

Figure 1. Schematic of BOR-60 flat SSRT specimen.

A total of 29 materials that include Types 304, 316, and 347 SSs; cast SSs; Alloy 690; and a model alloy were selected for irradiation. The chemical compositions of these alloys are given in Table 1. To investigate the effects of thermal-mechanical treatments, specimens in cold-worked (CW) and solution-annealed (SA) conditions were included. Grain-boundary engineering (GBE) is another thermal-mechanical process to be evaluated. By increasing the fraction of coincident site lattice (CSL) boundaries, GBE treatment is thought to be beneficial for improving SCC resistance.[22-24] Several GBE alloys and their non-GBE base materials are included in this study to assess the effect of GBE treatment.

Previous SSRT results obtained in a BWR environment indicate that impurities, such as sulfur and oxygen, could have significant effects on cracking behavior. To evaluate their effects in the low-potential PWR environment, several SSs with different levels of sulfur and oxygen content were included in this study. Type 304 SS with normal and low carbon content are also selected for evaluating the effect of carbon. In addition, Type 316LN SSs with and without titanium and a 304-like model alloy with high chromium content are also included.

Table 1. Materials irradiated in the BOR-60 reactor (wt.%).

Material Type[a]	Heat ID	Material Code	Composition (wt.%)								
			Ni	Si	P	S	Mn	C	N	Cr	Other Elements [b]
347 SA	316642	D1	10.81	0.29	0.023	0.014	1.56	0.030	0.021	18.06	Nb 0.60, Mo 0.29, Cu 0.09
347 CW	316642CW	D2	10.81	0.29	0.023	0.014	1.56	0.030	0.021	18.06	Nb 0.60, Mo 0.29, Cu 0.09
304 SA	2333	B1	8.5	0.65	0.031	0.029	1.38	0.035	0.068	18.30	Mo 0.37
304 CW	2333CW	B2	8.5	0.65	0.031	0.029	1.38	0.035	0.068	18.30	Mo 0.37
316 LN SA	623	B3	12.20	0.70	0.007	0.002	0.97	0.019	0.103	17.23	Mo 2.38, Cu 0.21
316 LN-Ti SA	625	B4	12.30	0.72	0.007	0.002	0.92	0.012	0.064	17.25	Mo 2.38, Ti 0.027, Cu 0.21
316 SA	C21	B5	10.24	0.51	0.034	0.001	1.19	0.060	0.020	16.28	Mo 2.08, B<0.001
316 CW	C21 CW	B6	10.24	0.51	0.034	0.001	1.19	0.060	0.020	16.28	Mo 2.08, B<0.001
316 WW	C21 WW	B7	10.24	0.51	0.034	0.001	1.19	0.060	0.020	16.28	Mo 2.08, B<0.001
CF-3 cast SS	52	C1	9.40	0.92	0.012	0.005	0.57	0.009	0.052	19.49	Mo 0.35, δ 13.5%
CF-8 cast SS	59	C2	9.34	1.08	0.008	0.007	0.60	0.062	0.045	20.33	Mo 0.32, δ 13.5%
CF-3 cast SS	69	C3	8.59	1.13	0.015	0.005	0.63	0.023	0.028	20.18	Mo 0.34, δ 23.6%
CF-8 cast SS	68	C4	8.08	1.07	0.021	0.014	0.64	0.063	0.062	20.64	Mo 0.31, δ 23.4%
304 SA	C1	A1	8.12	0.50	0.038	0.002	1.00	0.060	0.060	18.11	B 0.001
304 SA	C9	A2	8.75	0.39	0.013	0.013	1.72	0.062	0.065	18.48	B <0.001
304 SA	C12	A3	8.23	0.47	0.018	0.002	1.00	0.060	0.070	18.43	B <0.001
304 CW	C1 CW	A4	8.12	0.50	0.038	0.002	1.00	0.060	0.060	18.11	B 0.001
304 CW	C12 CW	A5	8.23	0.47	0.018	0.002	1.00	0.060	0.070	18.43	B <0.001
304 GBE	304 GBE	A6	8.43	0.46	0.014	0.003	1.54	0.065	0.088	18.38	Mo 0.51, Co 0.22
316 GBE	316 GBE	B8	11.12	0.57	0.011	0.022	1.85	0.070	0.056	16.57	Mo 2.27, Co 0.10
690 GBE	690 GBE	E1	59.40	0.30	-	0.003	0.42	0.010	-	29.10	Fe 10.26
304 BASE	304 BASE	A7	8.46	0.41	0.013	0.014	1.56	0.065	0.086	18.32	Mo 0.36, Co 0.12
316 BASE	316 BASE	B9	10.30	0.43	0.013	0.020	1.53	0.055	0.054	16.42	Mo 2.19, Co 0.10
690 BASE	690 BASE	E2	61.49	0.05	-	<0.01	0.15	0.030	-	29.24	Fe 9.02
HP 304L SA	945	A8	9.03	0.03	<0.005	0.005	1.11	0.005	0.003	19.21	O 0.047, Mo <0.005
HP 304L SA	1327	A9	9.54	0.01	0.001	0.002	1.12	0.006	<0.001	19.71	O 0.008, Mo 0.02
304L SA	C3	A10	8.91	0.46	0.019	0.004	1.81	0.016	0.083	18.55	B< 0.001
304L CW	C3 CW	A11	8.91	0.46	0.019	0.004	1.81	0.016	0.083	18.55	B< 0.001
304-like alloy	L5	A12	9.66	0.90	0.113	0.028	0.47	0.006	0.033	21.00	B<0.001

[a] SA = solution annealed; CW = cold worked; WW = warm worked at 400°C; SS = stainless steel; GBE = grain boundary engineered; BASE = base heat for GBE modification; HP = high purity.
[b] δ = ferrite content.

2.2 Irradiation

All SSRT specimens were irradiated in the BOR-60 reactor, a sodium-cooled fast breeder reactor located in the Research Institute of Atomic Reactor (RIAR), Dimitrovgrad, Russia. Two irradiation experiments, Boris-6 and -7, were carried out between 2001 and 2004 in this study.[25] The Boris-6 irradiation included eight irradiation sub-cycles and several maintenance shut-down periods, and the Boris-7 irradiation had six irradiation sub-cycles. The irradiations were conducted in the fifth row of the reactor core.

Neutron fluence was monitored by five dosimeters loaded into the central channel of the irradiation rig and in baskets with the specimens. The dosimeters were analyzed by RIAR after irradiations.[25] The samples were tied into bundles (4 to 5 samples in each bundle) using stainless steel wires and loaded into irradiation baskets. The specimens were in direct contact with sodium coolant during irradiations. The irradiation temperature was controlled by the inlet and outlet sodium, which were kept at 315°C and

325°C, respectively. Magnesium-Zinc eutectic thermal monitors were also placed among specimens in several baskets to ensure that the irradiation temperature was below 343°C throughout the entire irradiation experiments.

The irradiation specimens were discharged at different times between 2001 and 2004 according to their target doses. All SSRT specimens were first cleaned of residual sodium and then transferred to Argonne National Laboratory via Westinghouse and Studsvik in 2005 (Boris-6 specimens) and 2009 (Boris-7 specimens). Table 2 lists all SSRT samples irradiated in the BOR-60 reactor and the damage dose each received in dpa.

Table 2. Displacement damage dose for specimens irradiated in Boris-6 and Boris-7 irradiation cycles.

Irradiation	Bundle ID	Specimen IDs	Dose (dpa-NRT) [a]
Boris-6	D1-1/B3-1	D1-1, D2-1, D2-2, B3-1	5.5
	A5-1/E1-1	A5-1, A6-1, B8-1, E1-1	5.5
	B4-1/B6-2	B4-1, B5-1, B6-1, B6-2	5.5
	A7-1/A8-1	A7-1, B9-1, E2-1, A8-1	4.8
	A1-1/A4-1	A1-1, A2-1, A3-1, A4-1	4.8
	A9-1/A12-1	A9-1, A10-1, A11-1, A12-1	4.8
	D1-2/D2-4	D1-2, D1-3, D2-3, D2-4	10.2
	B1-1/B2-2	B1-1, B1-2, B2-1, B2-2	10.2
	B3-2/B4-3	B3-2, B3-3, B4-2, B4-3	11.8
	B5-2/B6-3	B5-2, B5-3, B5-4, B6-3	11.8
	B6-4/B7-2	B6-4, B6-5, B7-1, B7-2	10.4
	C1-1/C2-2	C1-1, C1-2, C2-1, C2-2	10.4
Boris-7	A1-2 / A2-3	A1-2, A1-3, A2-2, A2-3	9.1
	A3-2 / A4-3	A3-2, A3-3, A4-2, A4-3	9.1
	A5-2 / A6-3	A5-2, A5-3, A6-2, A6-3	9.1
	B8-2 / E1-3	B8-2, B8-3, E1-2, E2-3	9.6
	A7-2 / B9-3	A7-2, A7-3, B8-2, B9-3	9.6
	E2-2 / A8-3	E2-2, E2-3, A8-2, A8-3	9.6
	A9-2 / A10-3	A9-2, A9-3, A10-2, A10-3	9.6
	A11-2 / A12-3	A11-2, A11-3, A12-2, A12-3	9.1
	B4-4 / C4-2	B4-4, B4-5, C3-2, C4-2	47.5
	A5-4 / A11-4	A5-4, E1-4, A9-5, A11-4	47.5
	C3-1 / B8-4	C3-1, C4-1, A6-4, B8-4	47.5
	A8-4 / A12-5	A8-4, A9-4, A12-4, A12-5	47.5
	D1-4 / D2-6	D1-4, D1-5, D2-5, D2-6	45.0
	B4-6 / B6-6	B4-6, B5-5, B5-6, B6-6	47.2
	B2-3 / A12-6	B2-3, B7-3, B7-4, A9-6, A12-6	48.1

[a] Estimated by RIAR, Norgett-Robinson-Torrens model.

2.3 Slow-Strain-Rate Tensile Tests

Table 3 shows the irradiated SSRT specimens at three doses in the current study. Among them, a total of 29 specimens were tested in a simulated PWR environment at 315-320°C, and six specimens were tested in air atmosphere at 320°C. Several tests were also performed on nonirradiated specimens in the PWR environment.

All SSRT tests on irradiated specimens were carried out in a test facility located in hot Cell 1 of the Irradiated Materials Laboratory at Argonne. This test facility is equipped with a worm gear actuator, a set of gear reducers, and a variable speed motor. The tests were conducted at a constant strain rate of 7.4×10^{-7} s^{-1}. The simulated PWR environment was provided by a recirculation loop, as shown in Fig. 2. The main components of the loop include a storage tank, a high-pressure pump, two regenerative heat

exchangers, several preheaters, an autoclave, a back-pressure regulator, two ion-exchange cartridges, and a cover-gas supply system. The high pressure portion of the system extends from the high-pressure pump through the back-pressure regulator. Over-pressurization of the high-pressure portion of the system including the autoclave is prevented by two rupture disks installed upstream of the high-pressure pump. One rupture disk is located close to the pump, and another one is located inside the hot cell. The ion-exchange cartridges are installed in the low-pressure portion of the system to trap any possible corrosion product or loose activity that may be picked up by water flowing around the irradiated test specimens. Two hydrogen leak sensors are installed above the cover-gas supply system and the storage tank to detect any leakage of hydrogen.

Table 3. Number of SSRT specimens received from the BOR-60 irradiation.

Material Type [a]	Heat ID	Material Code	Number of specimens		
			5 dpa [b]	10 dpa [b]	40 dpa [b]
347 SA	316642	D1	1	2	2
347 CW	316642CW	D2	2	2	2
ABB 304 SA	2333	B1	- [c]	2	-
ABB 304 CW	2333 CW	B2	-	2	1
316LN SA	623	B3	1	2	-
316LN-Ti SA	625	B4	1	2	3
316 SA	C21	B5	1	3	2
316 CW	C21 CW	B6	2	3	1
304 CW, low S	C12 CW	A5	1	2	1
304 GBE	304 GBE	A6	1	2	1
316 GBE	316 GBE	B8	1	2	1
690 GBE	690 GBE	E1	1	2	1
304 BASE	304 BASE	A7	1	2	-
316 BASE	316 BASE	B9	1	2	-
690 BASE	690 BASE	E2	1	2	-
HP 304L SA, high O	945	A8	1	2	1
HP 304L SA, low O	1327	A9	1	2	3
304L SA	C3	A10	1	2	-
304L CW	C3 CW	A11	1	2	1
304-like alloy	L5	A12	1	2	3

[a] SA = solution annealed; CW = cold worked at room temperature; WW = warm worked at 400°C; GBE = grain boundary engineered; BASE = base heat for GBE modification; HP = high purity.

[b] Target doses. The actual received doses are given in Table 2.

[c] "-" = No specimens available.

During the SSRT tests, water is circulated at a flow rate of 10-20 ml/min in the system. The autoclave temperature is maintained at 315-320°C and the pressure is between 1,750 and 1,800 psig. The simulated PWR environment is composed of high-purity deionized water containing 2 ppm lithium, 1,000 ppm boron, and ≈2 ppm dissolved hydrogen and less than 10 ppb dissolved oxygen. The conductivity of the water is about 20 μS/cm, and its pH is about 6.7 at room temperature. Prior to each test, the specimen is exposed to the PWR environment for 24 to 30 hours to stabilize test conditions.

Because of the small dimension of the irradiated specimens, extreme caution was required when installing them remotely with manipulators. To avoid bending or twisting during installation, a special

sample grip system was designed (Fig. 3). The sample grip includes two guiding rods that were inserted into the holes in both top and bottom halves to maintain a proper alignment during the test. The specimen was centered between two loading pins on the sample grip. After the two cover clips were tightened, the specimen could be loaded under tension and was protected from bending or twisting. The sample grip was then inserted into the tube autoclave and engaged with pull rods from both ends. The assembled autoclave was hung on the test frame without the lower pin in place to maintain a stress-free condition until the desired temperature and pressure were achieved. Using this sample grip system, remote handling of small samples becomes much easier, and a good alignment can be maintained throughout the tests. Figure 4 shows a fractured BOR-60 sample tested in the PWR environment. A strain rate of 7.4×10^{-7} s^{-1} was used for all tests in the PWR environment.

1. Cover gas supply cylinder
2. Two stage high-pressure regulator
3. Flash arrestor
4. Safety solenoid valve
5. Hydrogen alarm control panel
6. Hydrogen leak sensors
7. Excess flow valve
8. Low-pressure regulator
9. Flow meter
10. Check valve
11. Pressure gauge
12. Pressure relief valve
13. Vent to ventilation system
14. Feedwater storage tank
15. Sparge tube
16. Water sample port
17. Feedwater port
18. Recirculation pump
19. Ion exchange cartridge
20. Solenoid valve
21. High-pressure pump
22. Pressure transducer
23. High pressure gauge
24. Rupture disk
25. Accumulator
26. Heat exchanger
27. Autoclave preheater
28. Autoclave preheater thermocouple
29. Rupture disk
30. Tube autoclave
31. Thermocouple well
32. Seal retainers
33. Electrochemical potential (ECP) cell preheater
34. ECP cell
35. Air cooled coil
36. Heat exchanger
37. Back-pressure regulator thermocouple
38. Back-pressure regulator
39. pH meter
40. Conductivity meter
41. Heat exchanger thermocouple
42. ECP preheater thermocouple
v**. Flow control valves

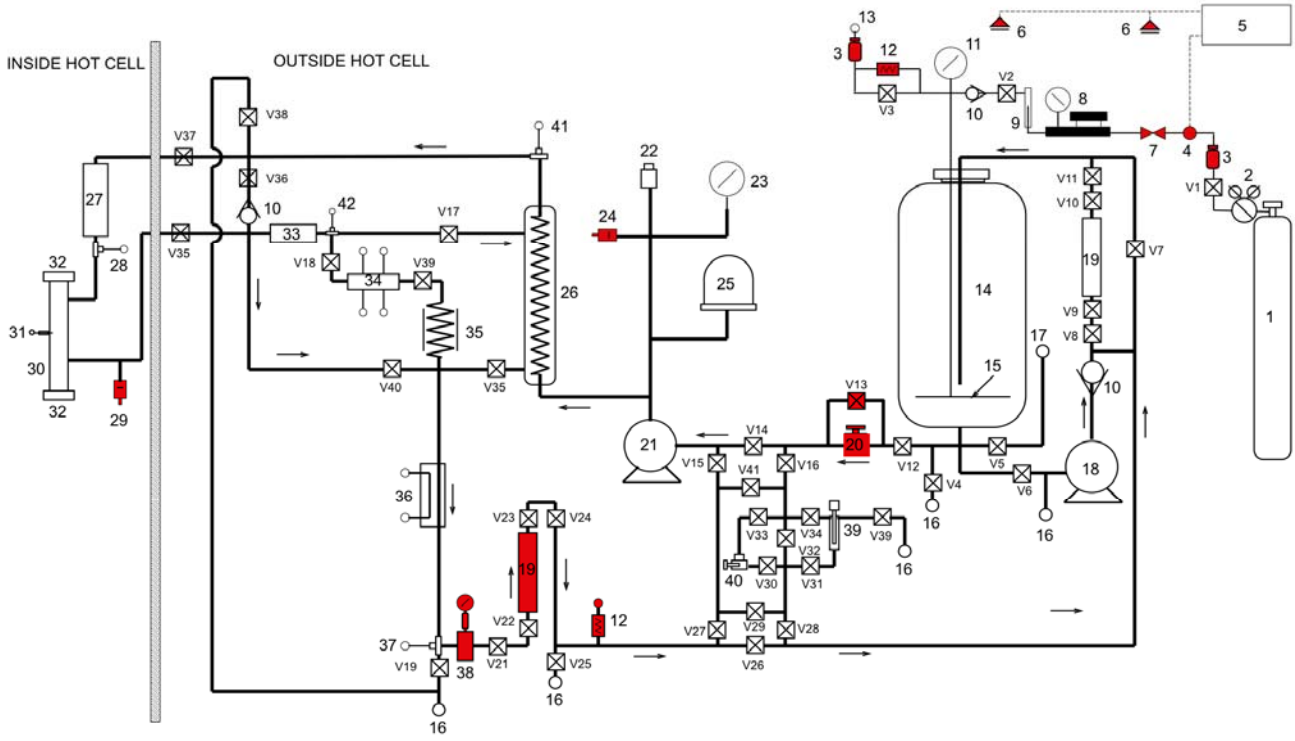

Figure 2. Schematic of water recirculation system.

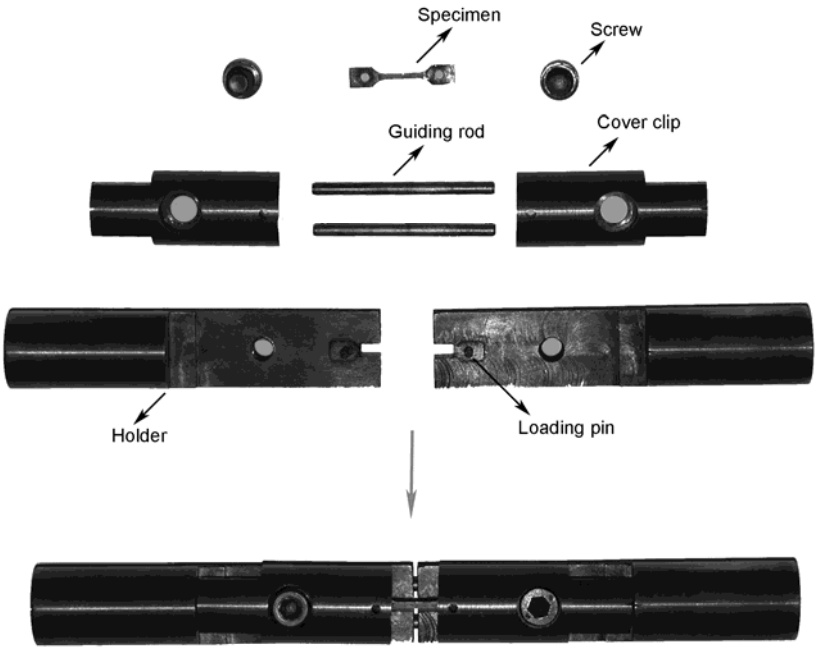

Figure 3. Sample grip system for the BOR-60 specimen.

Figure 4. A BOR-60 sample tested in the simulated PWR environment.

2.4 Fractographic Examination

After the SSRT tests, the fractured specimens were cleaned to remove radiological contaminations. The decontaminated specimens were then transferred to a scanning electronic microscopy (SEM) facility for fractographic examinations. The SEM used in this study is a lead-shielded FEI XL-30 located in a radiological controlled area. To minimize radiation exposure, the shoulders of the tested specimens were often removed prior to examinations. Secondary electron imaging at 10-kV or 15-kV acceleration voltage with 15- to 20-mm work distance was used for most of the observations.

3 Results

3.1 Tests in Air Atmosphere

Several baseline tests were conducted on Types 304, 316 and 347 SSs in air atmosphere at two doses (~5 and 10 dpa). Both SA and CW specimens were included, and a nonirradiated test was also carried out on a Type 316 in SA condition. The purpose of these air tests was to establish a reference for the SSRT tests in water. The test temperature and strain rate were 320°C and 7.4×10^{-7} s^{-1}, respectively. Figure 5 shows the engineering stress-strain curves obtained from these tests. The tensile properties of these specimens are summarized in Table 4. Strain-softening is observed for all irradiated specimens. If a yield point can be seen on the stress-strain curve below 0.2% plastic strain, this stress is reported as yield strength (YS) in the table. Otherwise, the stress at 0.2% plastic strain is reported. The ultimate tensile strength (UTS) is the maximum stress in the engineering stress-strain curve, and the total elongation (TE) is the final plastic strain before fracture. A time to failure (TF) is also estimated for each test and is shown in Table 4.

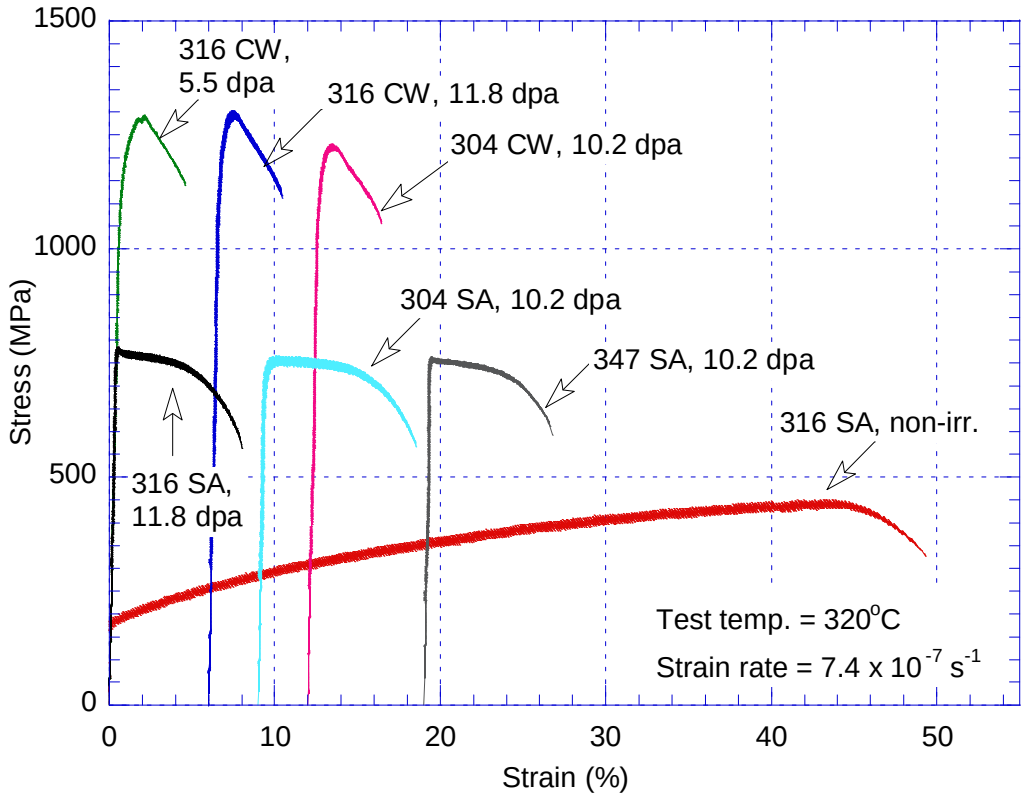

Figure 5. Tests in air atmosphere on SA and CW Types 304, 316, and 347 SSs.

Irradiation hardening is evident among all air tests. At about 10 dpa, the YS of SA 316 SS is nearly 600 MPa higher than that of the nonirradiated SA sample. The YS of the irradiated CW specimen is even higher. It is clear that the strength of the materials can be increased considerably by neutron irradiation. In the meantime, the ductility of irradiated materials is greatly reduced. For the SA 316 SS, the overall elongation is lowered from ~50% before irradiation to less than 8% at ~10 dpa. The decrease in TE is also greater for the CW specimens. This considerable loss of plasticity is a clear indication of severe embrittlement caused by irradiation damage.

As shown in Fig. 5, the nonirradiated 316 SS can be hardened considerably with increasing strain, and its UTS is much higher than its YS. For the irradiated SSs, however, strain-hardening is completely absent in the SA Types 316 and 347 SSs and very limited for all CW specimens and the SA Type 304 specimen. The lack of work-hardening leads to a very low uniform deformation and an earlier onset of plastic instability (i.e., necking).

With the same thermal-mechanical treatment (i.e., SA or CW), the differences in strength and ductility are quite small among different types of SSs (304, 316 and 347 SSs) tested in the air atmosphere. It is clear that irradiation hardening and embrittlement are the dominant effects for all austenitic SSs in air tests. In addition, for CW Type 316 SS, the strengths of the 5.5-dpa and 11.8-dpa specimens are similar, suggesting that irradiation hardening had already saturated at ~5 dpa in these tests.

Table 4. Tensile properties of SSRT tests in air for selected BOR-60 specimens at 320°C.

Material Type	Heat Treatment	Spec. ID	Dose (dpa)	YS [a] (MPa)	UTS [a] (MPa)	TE [a] (%)	RA [a] (%)	Time to failure (hr)
316	SA	B5-N3	-	180	439	49.3	-	206
316	SA	B5-3	11.8	778	778	7.7	59	41
316	CW	B6-2	5.5	1174	1287	3.9	26	48
316	CW	B6-3	11.8	1236	1295	3.8	30	37
304	SA	B1-1	10.2	740	755	9.2	63	52
304	CW	B2-1	10.2	1159	1225	3.8	19	40
347	SA	D1-3	10.2	758	758	7.5	44	49

[a] YS = yield strength; UTS = ultimate tensile strength; TE = total elongation; RA = reduction of area.

Fractographic examination is carried out on these specimens, and the results are shown in Figs. 6-11. All samples exhibit ductile failure, and the dominant fracture morphology is dimples of various sizes. The dimple structure appears very similar among all tested samples. On average, more of the large dimples can be seen in Type 304 SSs than in Types 316 or 347 SSs. Small brittle areas and mixed-mode fracture can be seen at the center of the specimens (e.g., Figs. 6c, 7c, 9a and 10a) where a triaxial state of stress is developed. In addition, transgranular cracking (TG) areas are present in all CW specimens at both doses (Figs. 7b, 8b, and 10b). Compared to the 5.5-dpa CW 316 specimen, a slightly larger TG area can be seen in the 11.8-dpa specimen. Similar TG areas can be seen in all SA specimens as well (Figs. 6d, 9c, and 11d). An area of mixed-mode fracture can be seen at one corner of the 10.2-dpa Type 347 SS specimen (Fig. 11c). The cross-section area of fracture surface is measured from SEM images, and a reduction of area is estimated for each sample. These values are also included in Table 4 as another measure of ductility in irradiated specimens.

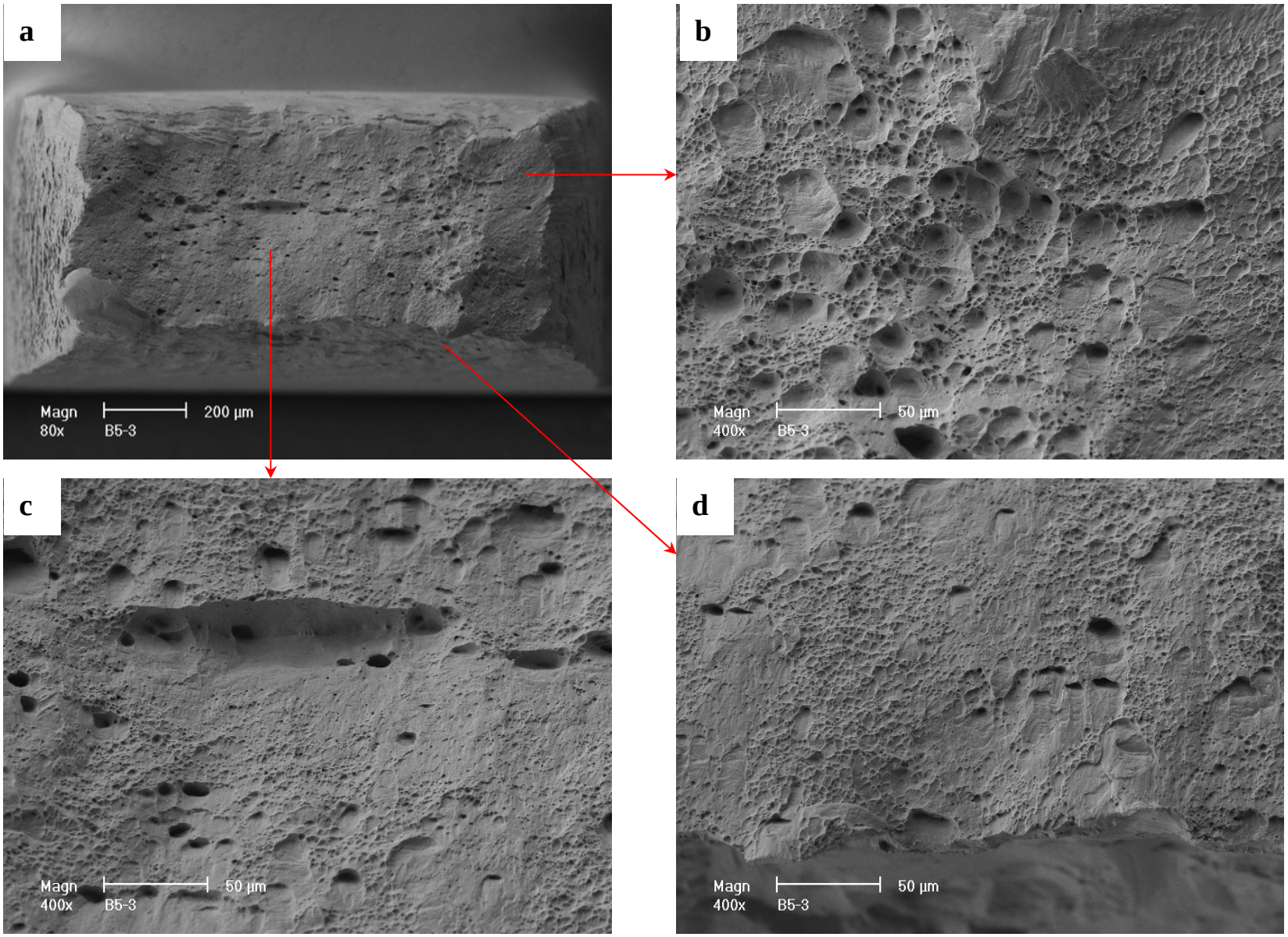

Figure 6. Fracture surface of SA Type 316 SS irradiated to 11.8 dpa and tested in air (specimen B5-3).

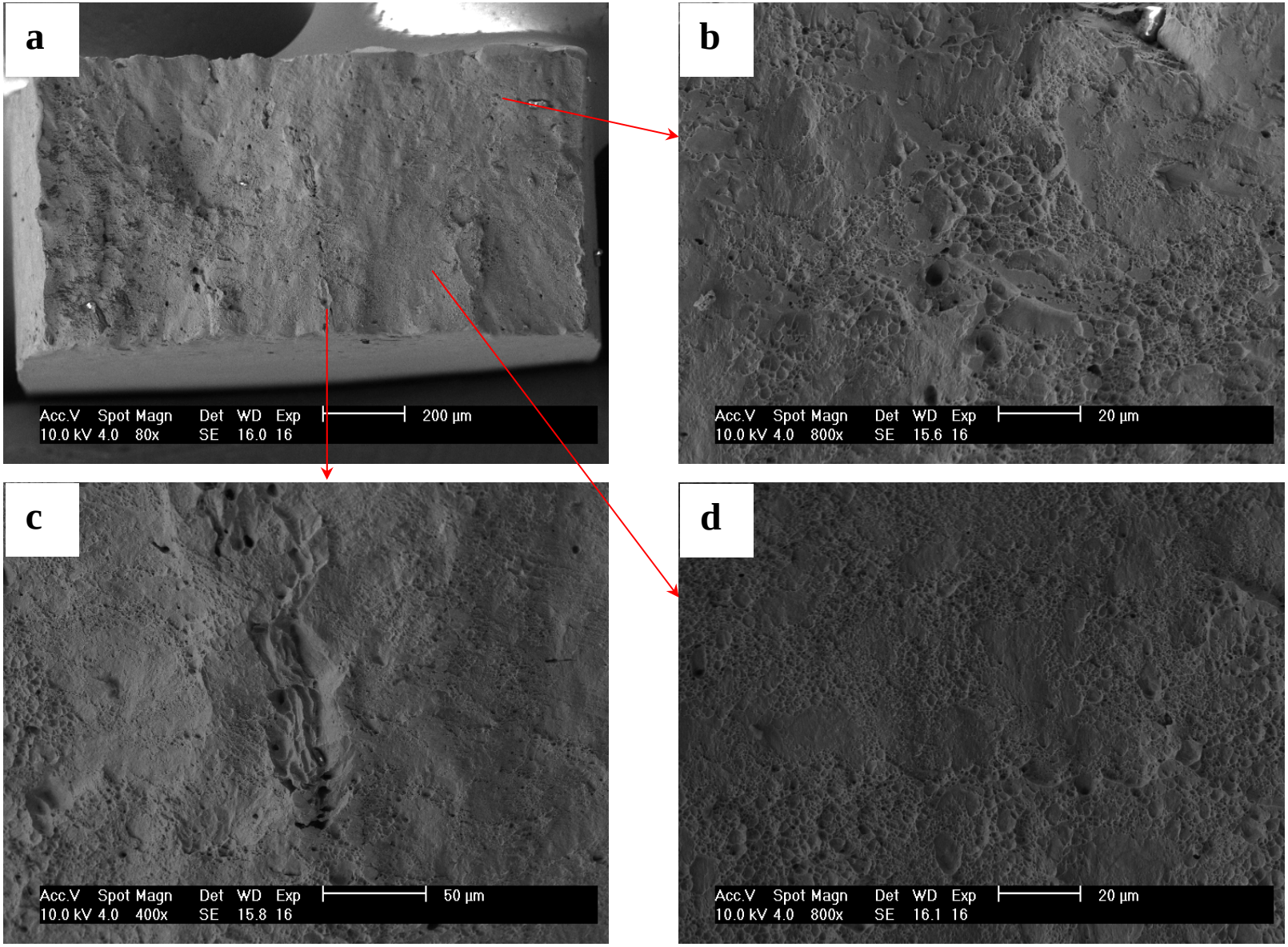

Figure 7. Fracture surface of CW Type 316 SS irradiated to 5.5 dpa and tested in air (specimen B6-2).

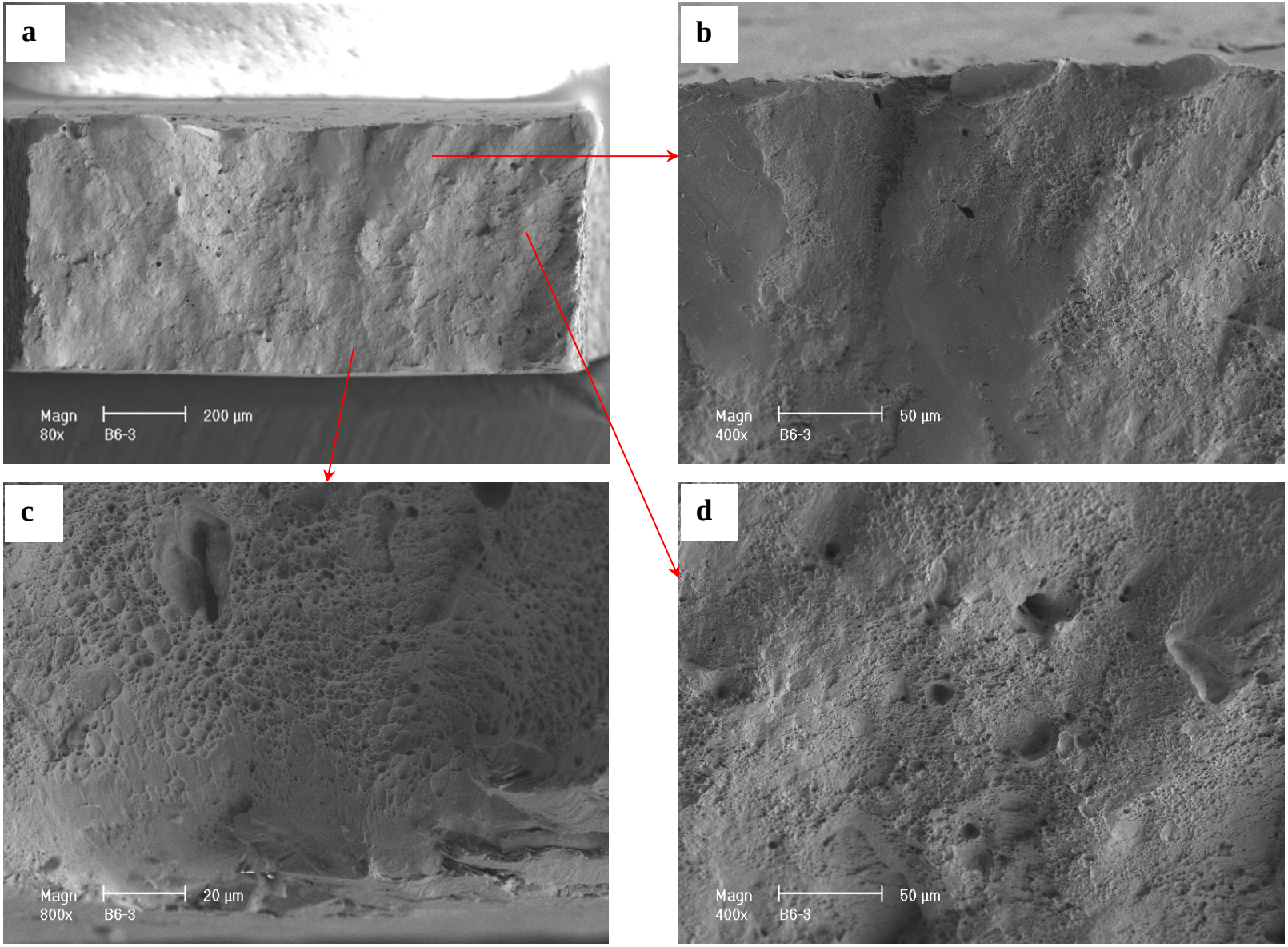

Figure 8. Fracture surface of CW Type 316 SS irradiated to 11.8 dpa and tested in air (specimen B6-3).

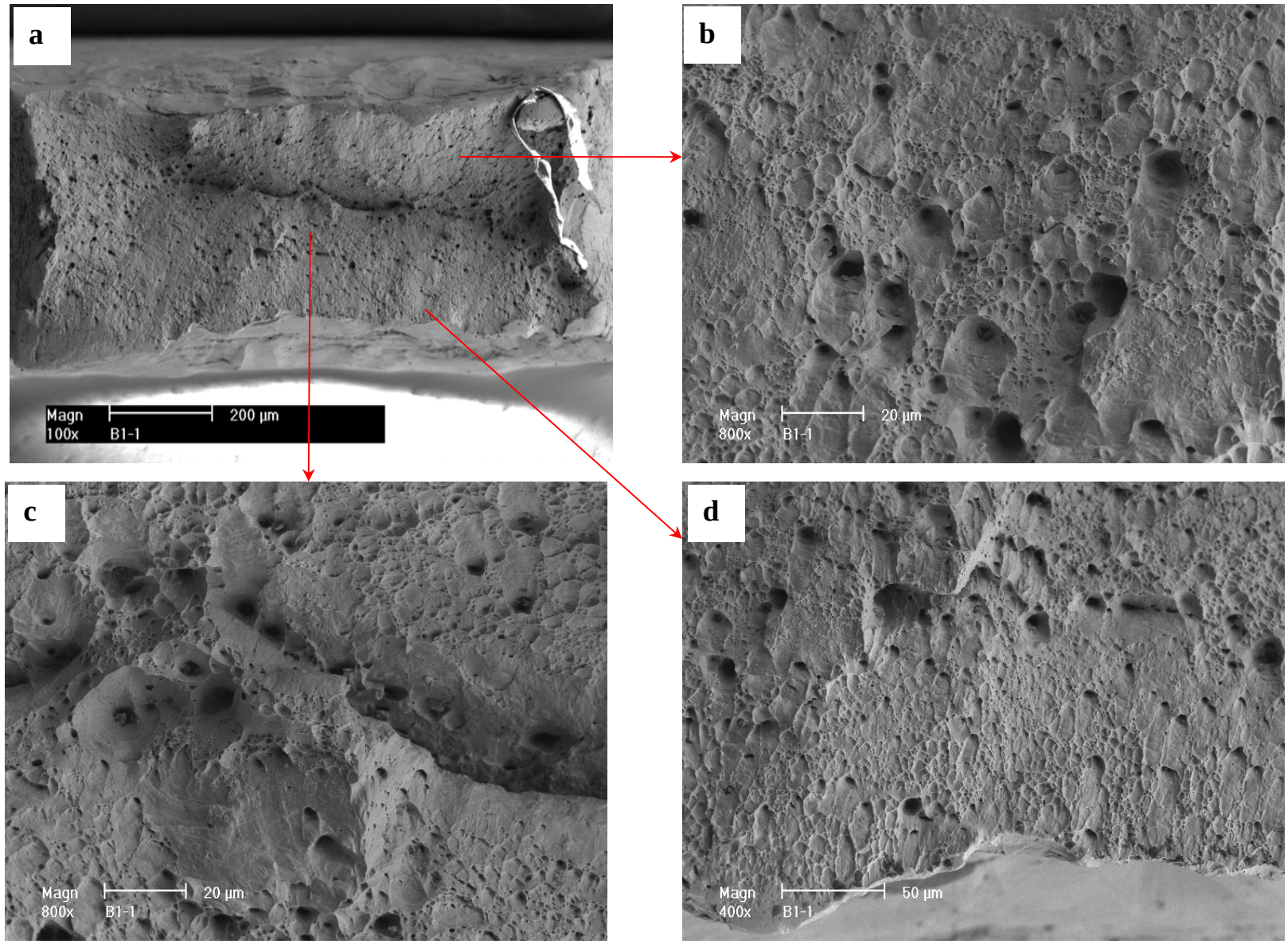

Figure 9. Fracture surface of SA Type 304 SS irradiated to 10.2 dpa and tested in air (specimen B1-1).

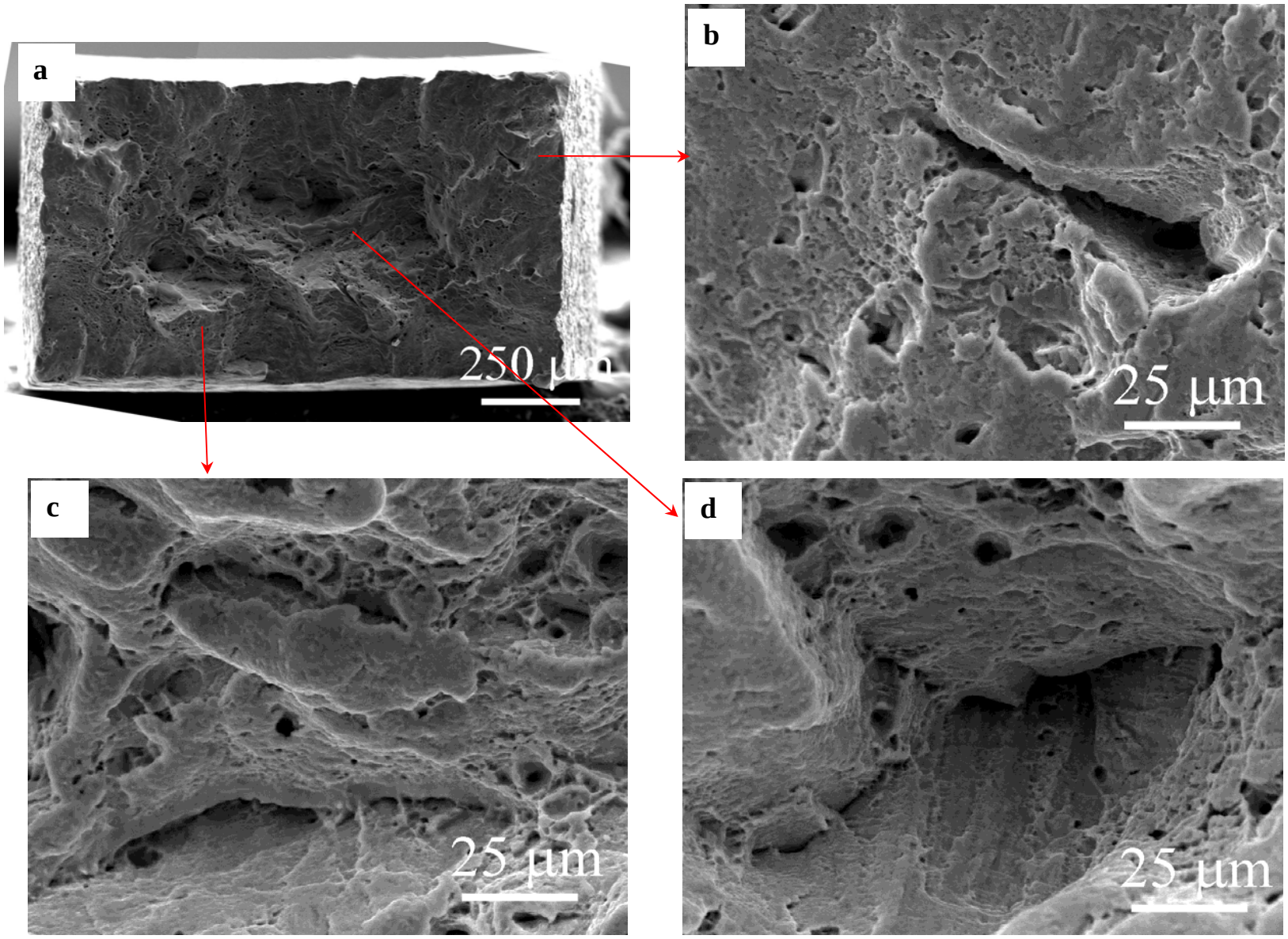

Figure 10. Fracture surface of CW Type 304 SS irradiated to 10.2 dpa and tested in air (specimen B2-1).

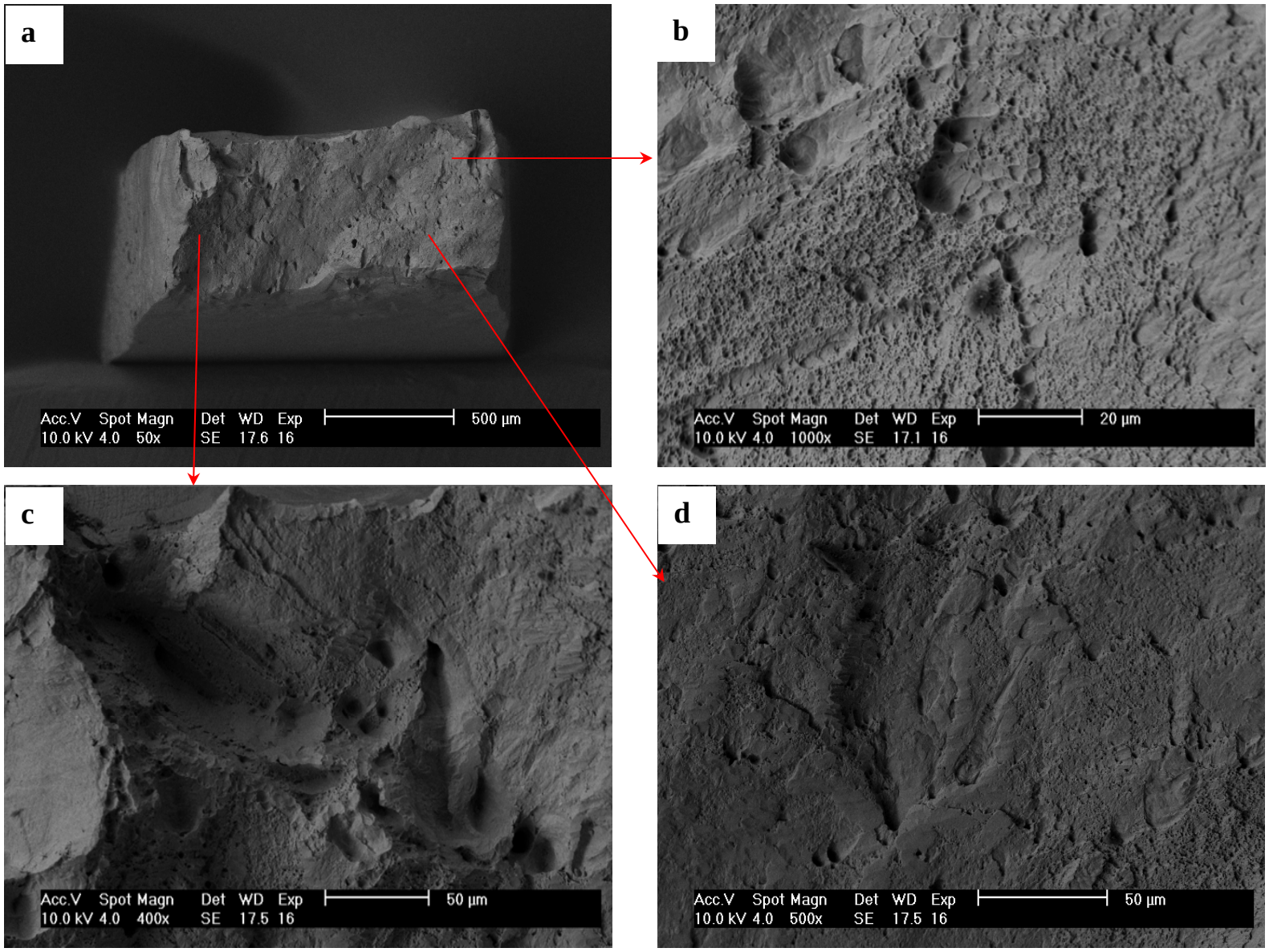

Figure 11. Fracture surface of SA Type 347 SS irradiated to 10.2 dpa and tested in air (specimen D1-3).

3.2 SSRT Tests in PWR Water on Types 316 and 316LN SSs

A total of seven SSRT tests at three doses were carried out in PWR water on SA and CW 316 SSs, and low-carbon, nitrogen-strengthened 316 SSs (316LN), both with and without the addition of titanium. The tests were performed at 315°C with a constant strain rate of 7.4E-7 1/s. Figure 12 shows the stress-strain curves obtained from these tests. The tensile results are also summarized in Table 5.

For Type 316 SS, three CW specimens at 5.5, 10.4 and 47.2 dpa and one SA specimen at 47.2 dpa were tested in a simulated PWR environment. As shown in Fig. 12a, the YSs are similar at all three doses for the CW specimens, indicating a saturation behavior of irradiation hardening below ~5 dpa. In the meantime, the TE declines from ~10.4 to 47.2 dpa, suggesting a continue trend of irradiation embrittlement (e.g. loss of ductility) for the CW 316 SS. Comparing the specimens with different thermal-mechanical treatments, the yield stress of the SA sample is significantly lower than that of the CW samples at the same dose (47.2 dpa). The TE is also much larger for the SA than for the CW materials. The impact of cold work on plastic deformation behavior is expected for nonirradiated materials. The results on irradiated specimens show that the effects of thermal-mechanical treatment remain the same after irradiation up to 47.2 dpa. A yield point was shown in the SSRT curve of the SA 316 specimen at 47.2 dpa, and no strain hardening was observed beyond the yield point. In contrast, a small increase in strength was still observed for the CW 316 specimen at the same dose.

Two 316LN specimens at 5.5 and 11.8 dpa and a titanium-stabilized 316LN specimen at 47.5 dpa were tested. As shown in Fig. 12b, the YS and UTS of Type 316LN SS increase slightly from 5.5 dpa to 11.8 dpa, indicating that irradiation hardening has not saturated at ~5 dpa for this material. The TE of the 5.5-dpa specimen is also about 40% higher than that of the 11.8-dpa sample. Despite its higher dose (47.5 dpa), the 316LN-Ti specimen shows a similar SSRT behavior as does the 316LN sample at 11.8 dpa. The YS and TE are comparable for both the 47.5-dpa 316LN-Ti specimen and 11.8-dpa 316LN specimen. At 47.5 dpa, no work-hardening is observed in the 316LN-Ti SS, and its UTS is slightly lower than that of 316LN SS at 11.8 dpa.

Table 5. Slow-strain-rate tensile tests on Types 316 and 316LN SSs in PWR water at 315-320°C.

Material Type	Heat Treatment	Spec. ID	Dose (dpa)	YS [a] (MPa)	UTS [a] (MPa)	TE [a] (%)	RA [a] (%)	Time to failure (hr)
316	SA	B5-5	47.2	794	794	6.8	40	39
316	CW	B6-1	5.5	1110	1257	3.5	29	35
316	CW	B6-4	10.4	1201	1291	4.0	29	51
316	CW	B6-6	47.2	1201	1257	2	21	44
316LN	SA	B3-1	5.5	925	925	7.7	53	51
316LN	SA	B3-2	11.8	1006	1062	4.8	41	46
316LN-Ti	SA	B4-4	47.5	1017	1017	4.9	47	40

[a] YS = yield strength; UTS = ultimate tensile strength; TE = total elongation; RA = reduction of area.

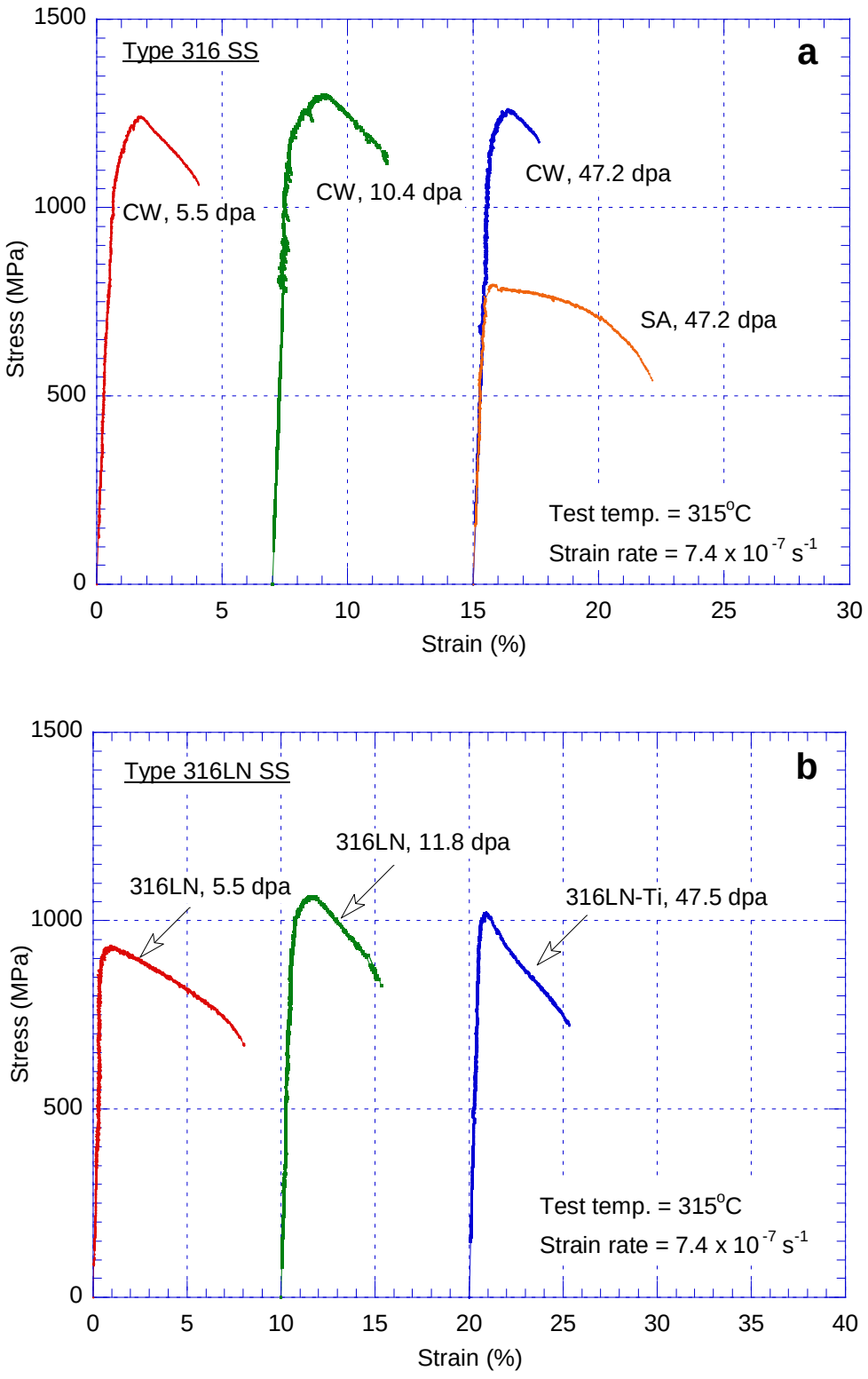

Figure 12. Stress-vs.-strain curves of SSRT tests on Types 316 and 316LN SSs in PWR water at 315°C.

Figures 13-16 show the fracture surfaces of the tested Type 316 SS specimens. The dominant fracture morphology is ductile dimples for both the CW and SA specimens. Although the size of the dimples varies significantly from one area to another, the CW samples on average have much finer dimples than those of the SA sample (e.g., Figs. 15d vs. 16b). For the CW 316 SS, small brittle areas can be seen at all doses at the interior of the specimens (Figs. 13c-d, 14b-d, and 15c-d). In contrast, several areas of cleavage and mixed mode fracture can be seen on the surface of the 47.2-dpa SA 316 SS (Fig. 16c-g). Some intergranular (IG) facets are also visible (Fig. 16c and 16e). Despite a much lower TE of the CW sample in the SSRT tests at 47.2 dpa, its fracture surface does not appear to be more susceptible to cracking than that of the SA sample at the same dose.

The three Type 316LN SSs tested in PWR water have similar fracture surfaces as shown in Figs. 17-19. Fine dimples less than 1 μm are the main fracture morphology among these samples. The 47.5-dpa specimen with the Ti addition has an area with much larger dimples, as shown in Fig. 19c. Small cleavage and mixed-mode fracture can be seen in the 5.5- (Fig. 17b-c) and 11.8-dpa (Fig. 18b-c) 316LN specimens. Although small brittle areas are present (Fig. 19d) in the 47.5-dpa 316LN-Ti sample, no cleavage cracking can be seen on its fracture surface.

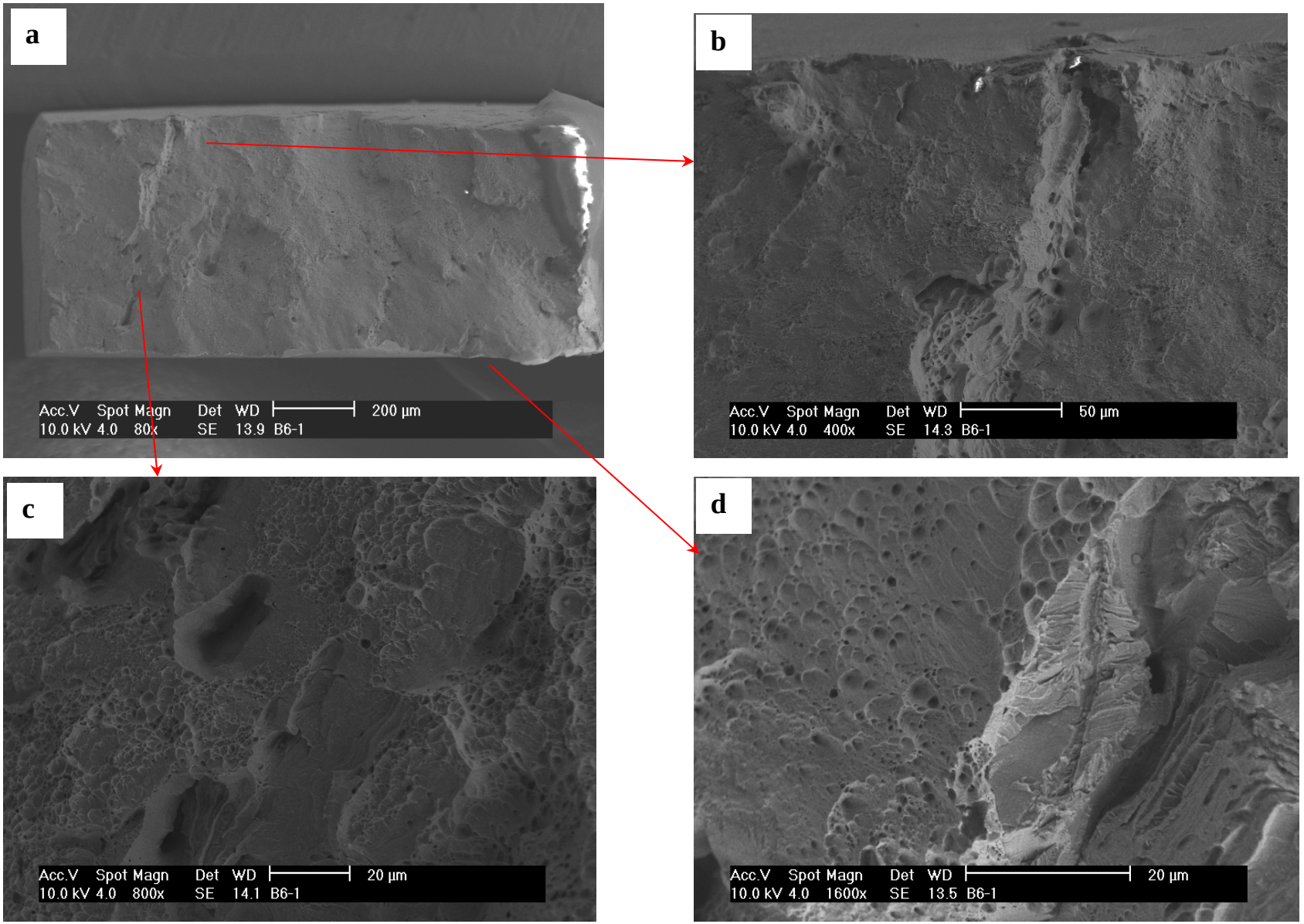

Figure 13. Fracture surface of CW Type 316 SS irradiated to 5.5 dpa and tested in PWR water (specimen B6-1).

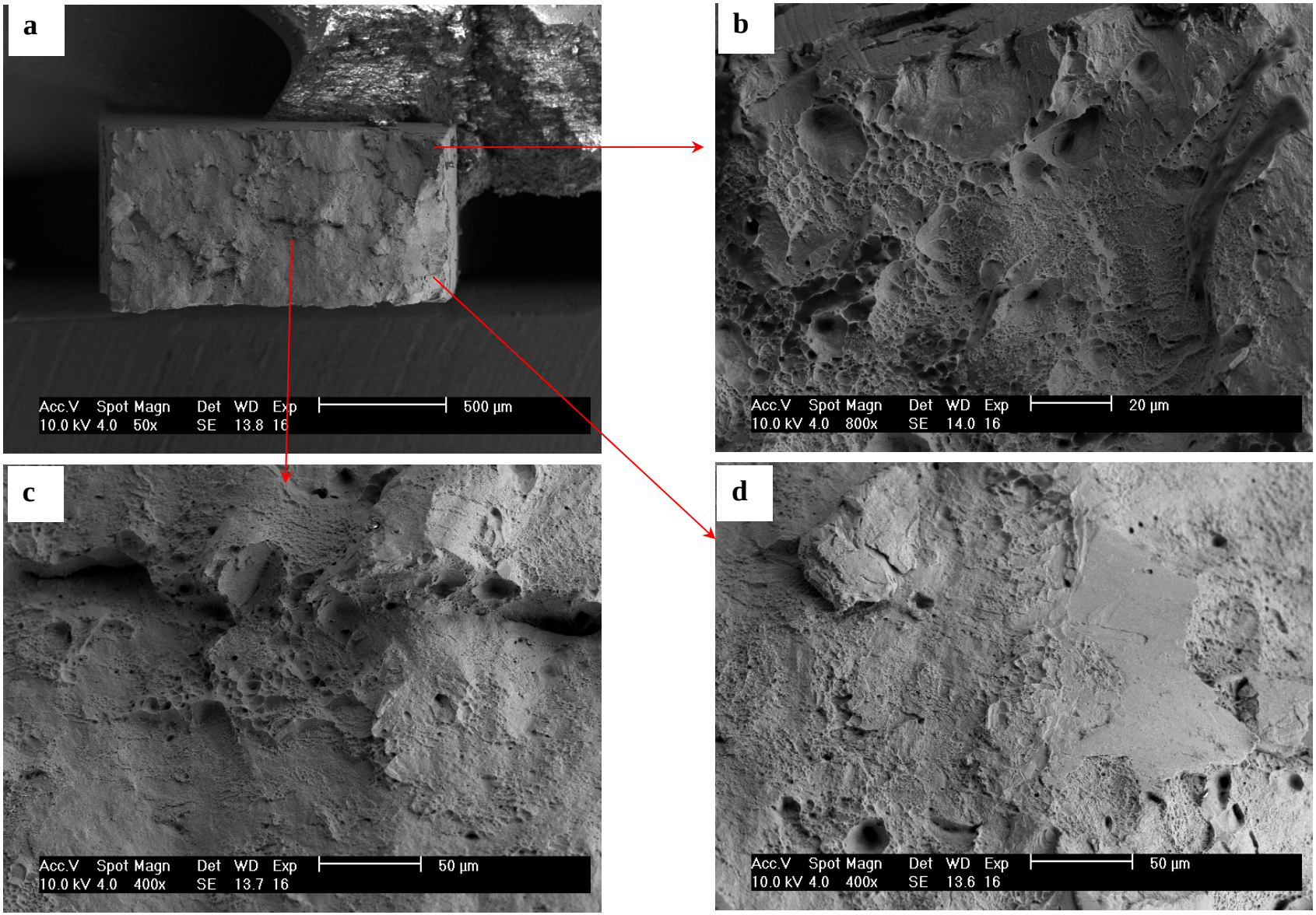

Figure 14. Fracture surface of CW Type 316 SS irradiated to 10.4 dpa and tested in PWR water (specimen B6-4).

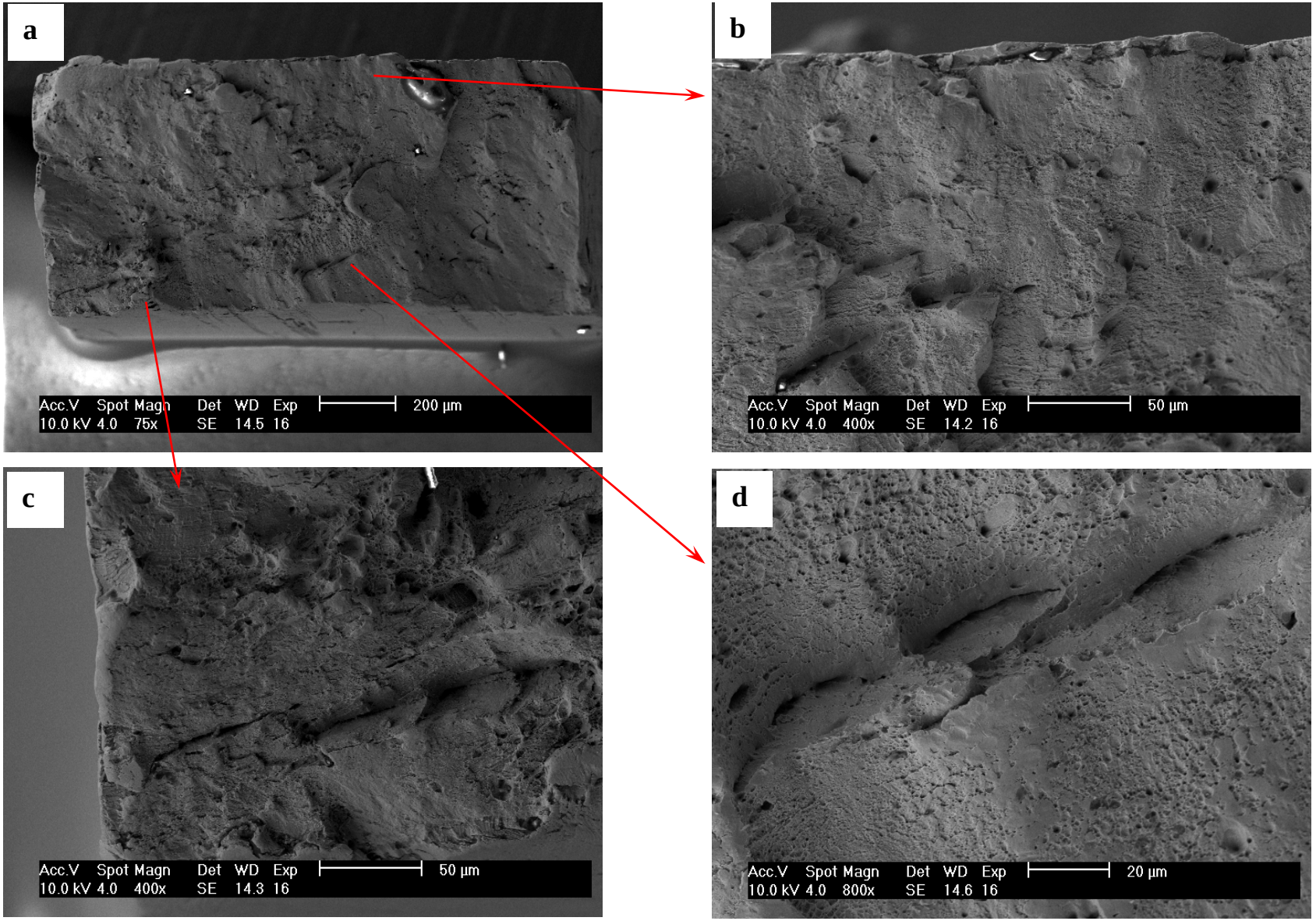

Figure 15. Fracture surface of CW Type 316 SS irradiated to 47.2 dpa and tested in PWR water (specimen B6-6).

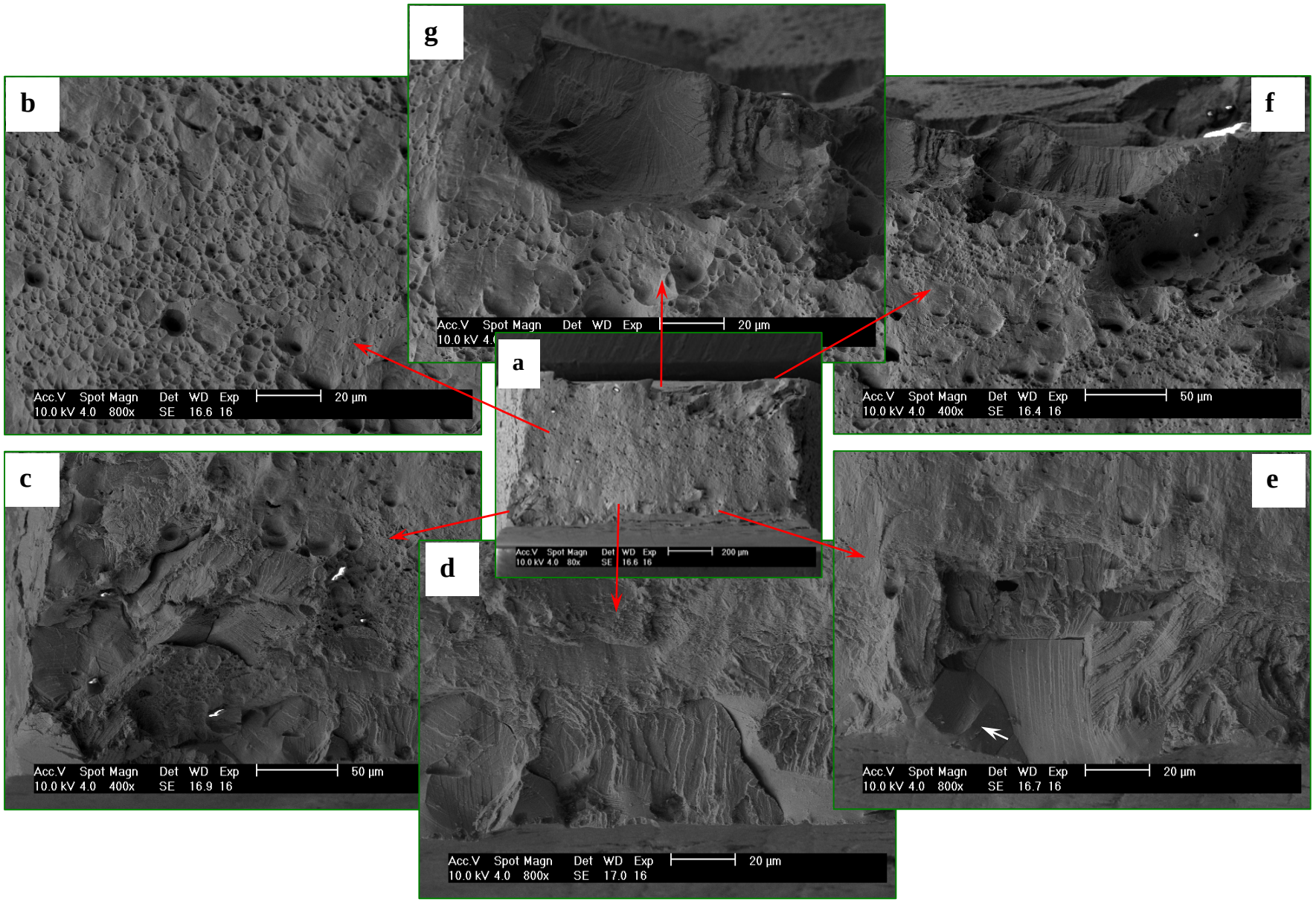

Figure 16. Fracture surface of SA Type 316 SS irradiated to 47.2 dpa and tested in PWR water (specimen B5-5).

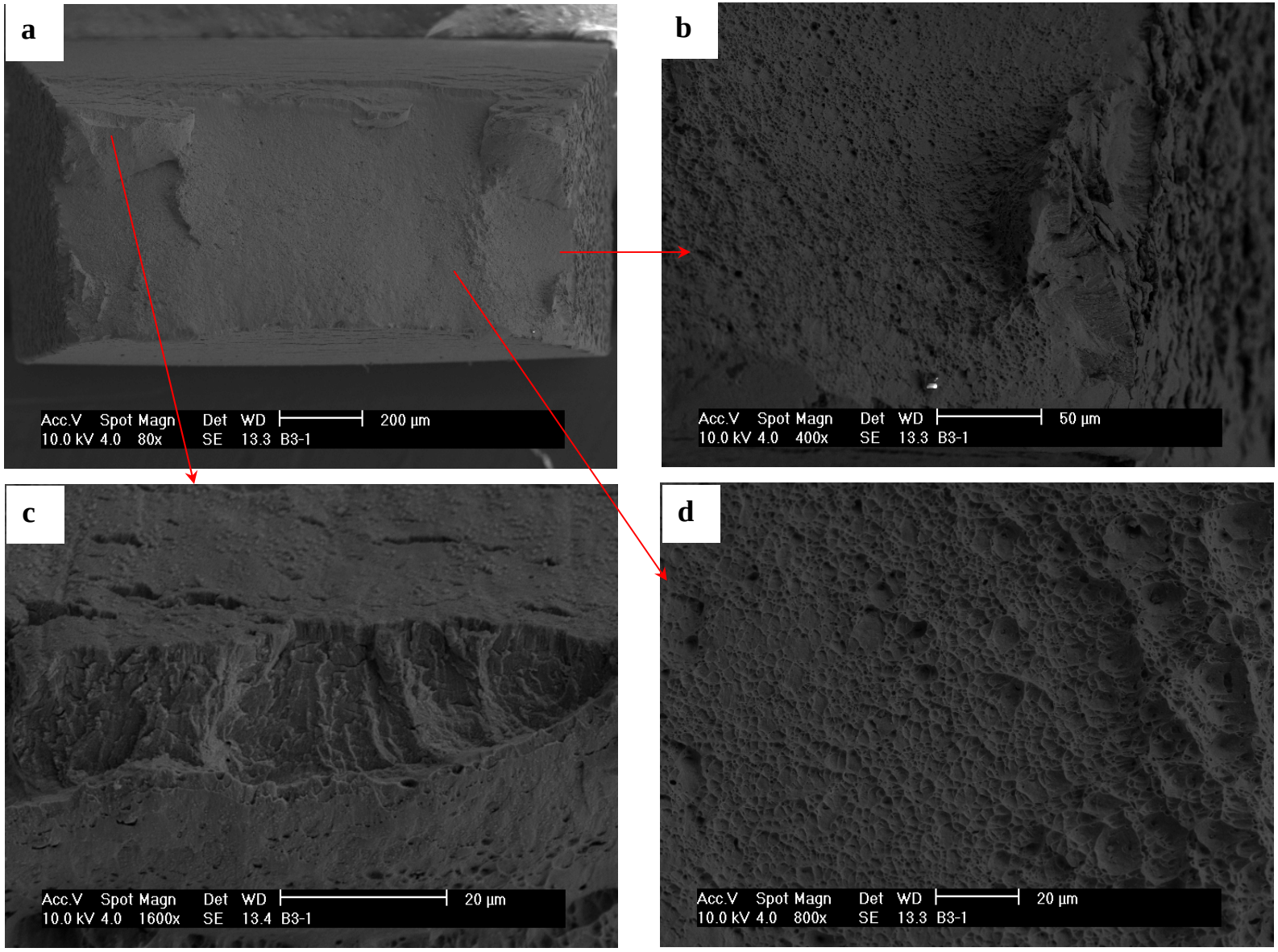

Figure 17. Fracture surface of SA Type 316LN SS irradiated to 5.5 dpa and tested in PWR water (specimen B3-1).

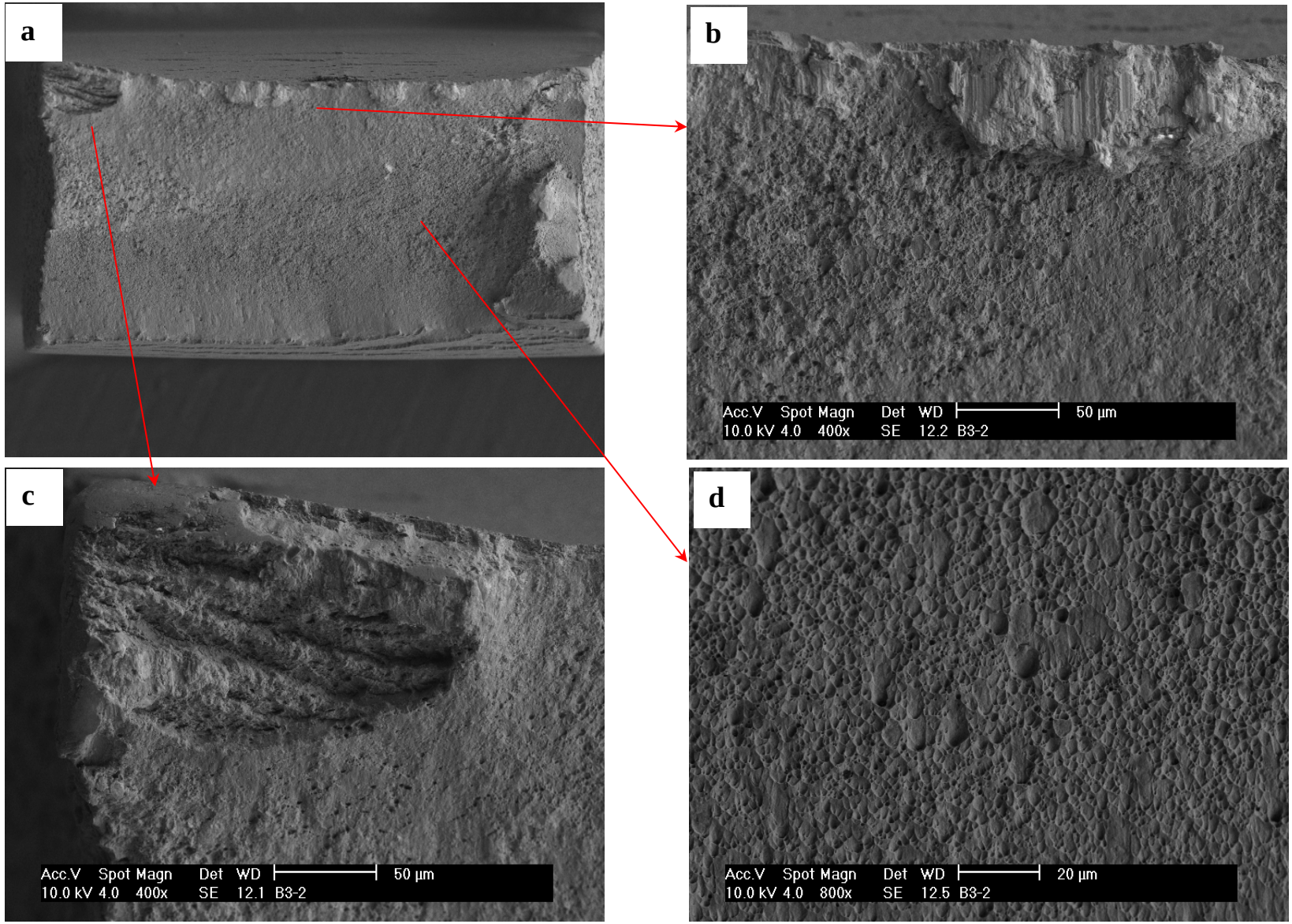

Figure 18. Fracture surface of SA Type 316LN SS irradiated to 11.8 dpa and tested in PWR water (specimen B3-2).

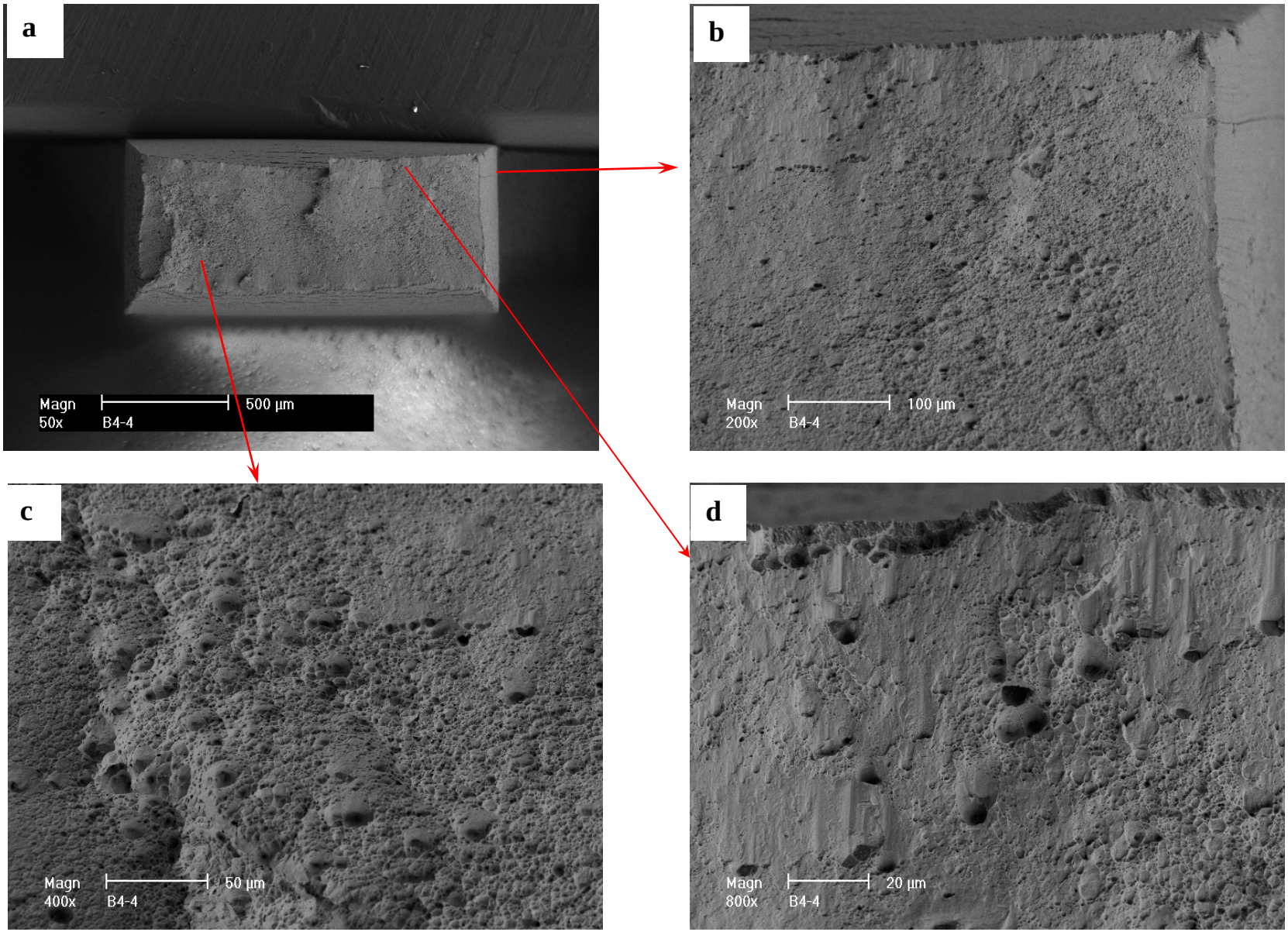

Figure 19. Fracture surface of SA Type 316LN-Ti SS irradiated to 47.5 dpa and tested in PWR water (specimen B4-4).

3.3 SSRT Tests in PWR Water on Type 304 and 304L SSs

A total of ten SSRT tests at two doses were carried out in PWR water on Types 304 and 304L SSs, a 304-like model alloy with higher Cr content, and two high-purity (HP) 304L SSs with different levels of oxygen content. These tests were performed at 315°C with a constant strain rate of 7.4×10^{-7} s^{-1}. Figure 20 shows the stress-strain curves obtained from these tests, and the tensile results are also summarized in Table 6.

Table 6. Slow-strain-rate tensile tests on Type 304L SS in PWR water at 315-320°C.

Material Type	Heat Treatment	Spec. ID	Dose (dpa)	YS [a] (MPa)	UTS [a] (MPa)	TE [a] (%)	RA [a] (%)	Time to failure (hr)
304L	SA	A10-2	9.6	745	745	7.8	57	45
304L	CW	A11-2	9.1	1035	1044	3.9	28	39
304L	CW	A11-4	47.5	1090	1090	3.1	23	42
304, low S	CW	A5-4	47.5	1215	1256	3.61	19	45
304-like	SA	A12-2	9.1	945	945	7.92	50	52
304-like	SA	A12-4	47.5	962	962	9.06	57	59
HP 304L, high O	SA	A8-2	9.6	615	615	6.32	60	34
HP 304L, high O	SA	A8-4	47.5	593	593	4.17	58	18
HP 304L, low O	SA	A9-2	9.6	652	652	6.91	82	36
HP 304L, low O	SA	A9-4	47.5	644	644	6.32	76	33

[a] YS = yield strength; UTS = ultimate tensile strength; TE = total elongation; RA = reduction of area.

For Type 304L SS (shown in Fig. 20a), both SA and CW specimens were tested at ~9 dpa. The CW sample shows a much higher YS and less TE than does the SA sample. At 47.5 dpa, only the CW specimen was tested. Compared to the 9.6-dpa CW specimen, it has a slightly higher YS and shorter TE. Although all three tests on Type 304L SS show strain softening, a well-defined yield point can be seen for the SA sample.

The SSRT results of a CW Type 304 SS at 47.5 dpa and a 304-like model alloy at 9.1 and 47.5 dpa are shown in Fig. 20b. Very little strain hardening remains at 47.5 dpa for the CW 304 SS, and its TE was only 3.6%. Compared to the CW Type 304L SS, the YS of the CW Type 304 SS with normal-carbon content is higher, illustrating the effect of carbon on the strength of irradiated SS. The differences in ductility (TE and reduction of area, RA) and time to failure (TF) between the 304L and 304 SS are too small to reveal any effect of carbon on the SSRT behavior. The two specimens of SA 304-like model alloy have much lower YSs and longer elongations than those of the CW specimens. At approximately the same dose, the SA 304-like model alloy has a much higher YS than that of the Type 304L SS. The higher strength of the model alloy can be attributed to its higher Cr and Ni contents. In the meantime, the TE results are similar between the 304-like model alloy and Type 304L SS (Fig. 20a). The SSRT curves of the model alloy are similar at 9.1 and 47.5 dpa, suggesting a saturated behavior above 9.1 dpa for this material.

The SSRT curves of HP 304L SSs with high and low level of oxygen content are notably different from other 304 and 304L alloys, as shown in Fig. 20c. The YSs of both HP 304L SSs are about 100 MPa lower than that of the SA Type 304L SS, and are among the lowest in all SSRT tests performed in this study. In addition, a well-defined yield point followed by a significant load-drop can be seen in all SSRT curves of the HP 304L SSs regardless their oxygen content levels. The observed load-drops can be as

much as 100 MPa at the yield points, suggesting an unstable deformation mode in these materials beyond yield. No strain hardening is observed for all HP 304L specimens. At both 9.6 and 47.5 dpa, the low-O HP 304L has slightly higher YSs and TEs than that of the high-O alloy. Although the TEs are similar at two doses for the low-O alloy, a lower elongation can be seen for the high-O SS at 47.5 dpa (Fig. 20c). The lower TE is mainly attributed to the smaller thickness of the 47.5-dpa specimen with high-O (about half the value of all other SSRT specimens). Thus, the TE of this particular sample is not directly comparable to other SSRT specimens. Nonetheless, it appears that irradiation hardening (i.e., an increase in YS) has become saturated below 9.6 dpa, while the TE continues to decline slightly from 9.6 to 47.5 dpa in the HP 304L SSs.

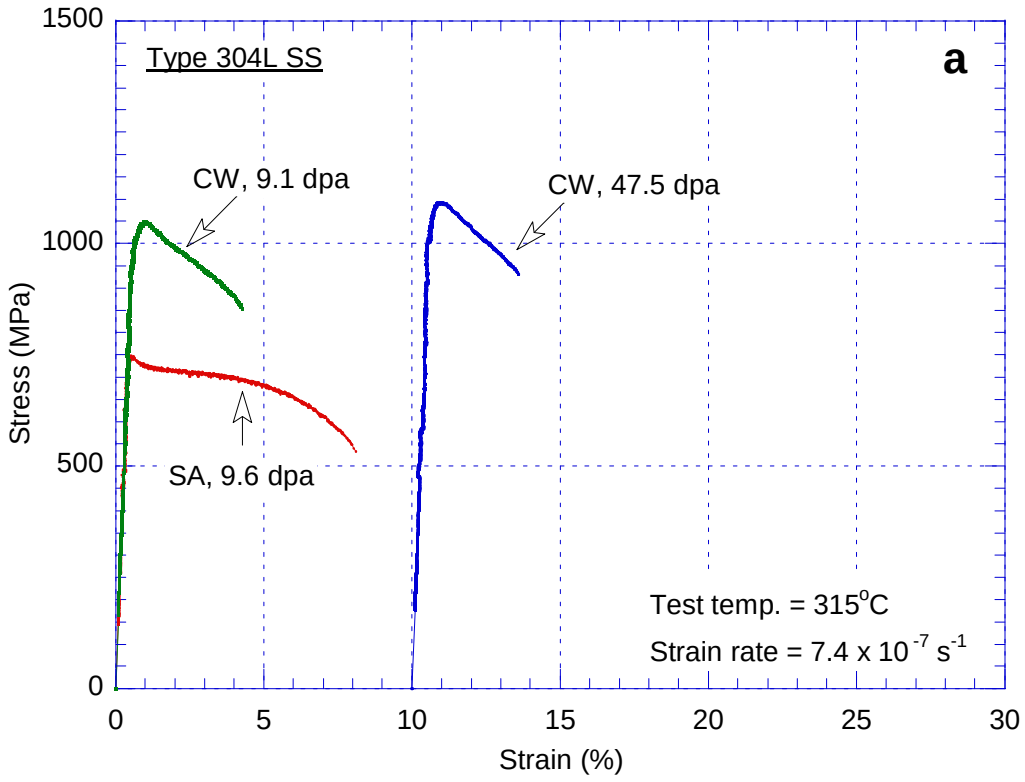

Figure 20. Stress-vs.-strain curves of SSRT tests on (a) Type 304L SS, (b) Type 304 SS and 304-like model alloys, and (c) HP 304L SSs with high- and low-O content levels, in PWR water at 315°C.

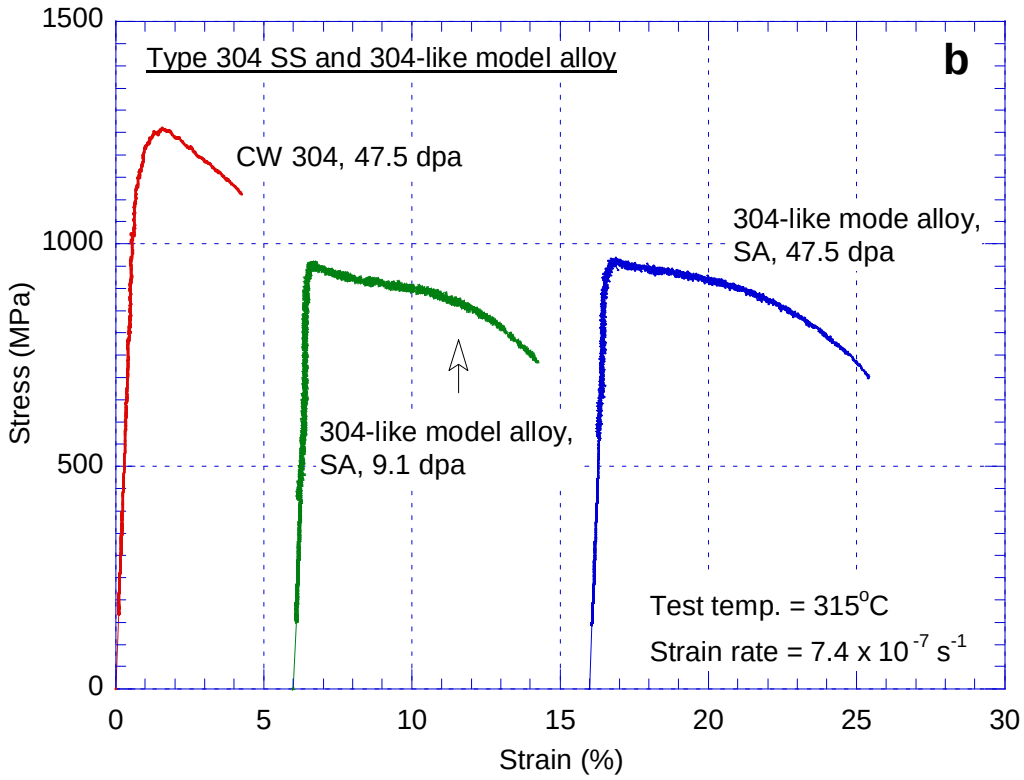

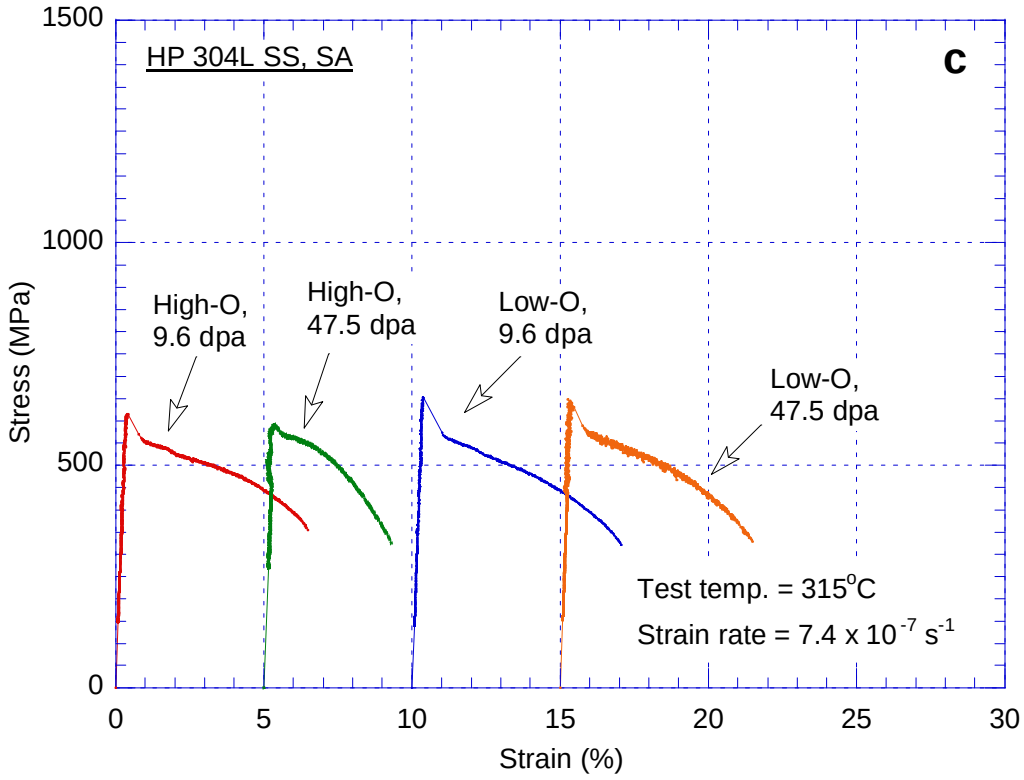

Figure 20. (Contd.)

The fracture surfaces of Types 304L and 304 SSs are shown in Figs. 21-24. The principal fracture morphology is ductile dimples among these samples. Transgranular, cleavage, and mixed-mode cracking can also be seen in some areas on the fracture surfaces. For Type 304L SS, the SA and CW samples are compared at about 10 dpa (Figs. 21 and 22). The SA 304L SS has relatively larger dimples, and brittle fracture areas (e.g., Fig. 22c-d) are more often seen in the CW sample. The reduction of area of the CW sample is only a half that of the SA sample, indicating that irradiation embrittlement is more severe for the CW 304L SS. At 47.5 dpa, small cleavage cracks can be seen on the fracture surface close to the sample surface (e.g., the bottom two images in Fig. 23). This brittle cracking feature is not present in ~10-dpa or SA 304L SS samples. Comparing Figs. 23 and 24, the fracture surfaces of CW 304 SS and CW 304L SS are similar at 47.5 dpa, and both specimens consist of dimples and small TG areas. Although the CW 304 SS has a higher YS than that of the CW 304L SS, its fracture surface does not appear more brittle than that of the 304L SS. This observation suggests that carbon content may not be a key factor for the cracking susceptibility of irradiated 304 SS in a PWR environment.

The fracture surfaces of the SA 304-like model alloy — with higher levels of Cr and Ni content than typical 304 SSs — are shown in Figs. 25 and 26. Again, the main fracture morphology is ductile dimples, and small brittle fracture areas can be seen on the fracture surfaces at both 9.1 and 47.5 dpa. Compared with Type 304L and 304 SSs, the dimple size is slightly larger in the model alloy. Cleavage cracking can be seen on the surfaces of both 9.1- and 47.5-dpa specimens. This result differs from those of the 304L SS specimens, where cleavage cracking is absent in the SA specimens. The 47.5-dpa model alloy shows a slightly higher RA than that of the 9.1-dpa sample. The reason for this unexpected result is not clear. It is possible that small variations in sample geometry and surface conditions contribute to this difference. Nonetheless, the measured RAs of the model alloy are similar to that of 304L SS, showing a good ductility at both doses.

Figures 27-30 show the fracture surfaces of HP 304L SSs with different levels of oxygen content. Microvoid coalescence is the dominant fracture mode of all HP 304L specimens regardless their oxygen content. Significant local plastic deformation can be seen on the fracture surfaces of all HP samples, leading to severe necking. Intensive plastic flow in these samples is also evident from ripples on dimple walls resulting from slip steps (Figs. 27b and 28b). No brittle fracture is observed in the samples until the end of the tests. It is clear that the load drops observed in Fig. 20c are resulting from the localized plastic deformation — but not from cracking. For the high-O samples, elongated dimples can be seen on the fracture surfaces at both doses (Figs. 27 and 28). The size of the dimples is more than 10 μm in the high-O samples, significantly larger than those of the other SSRT samples. These large dimples may be associated with inclusions in the high-O HP304L SS. This speculation cannot be verified at present. The measured RA from the fracture surface is about 60% at both doses, suggesting good plasticity even at 47.5 dpa. For the low-O specimens, necking is more evident. The cross-sections of the sample gauges are reduced to narrow edges at fracture (shown in Figs. 29 and 30), suggesting an even higher degree of localized deformation in these samples beyond yield. Because the plastic flow occurs locally near the necking, the TEs of the low-O samples are not affected strongly. Accordingly, the measured RA is about 80% for the low-O SS, which is considerably higher than that of the high-O SS. Despite the difference in RA, the fracture surfaces reveal little difference, and both HP 304L SSs display dimple fractures regardless of their doses.

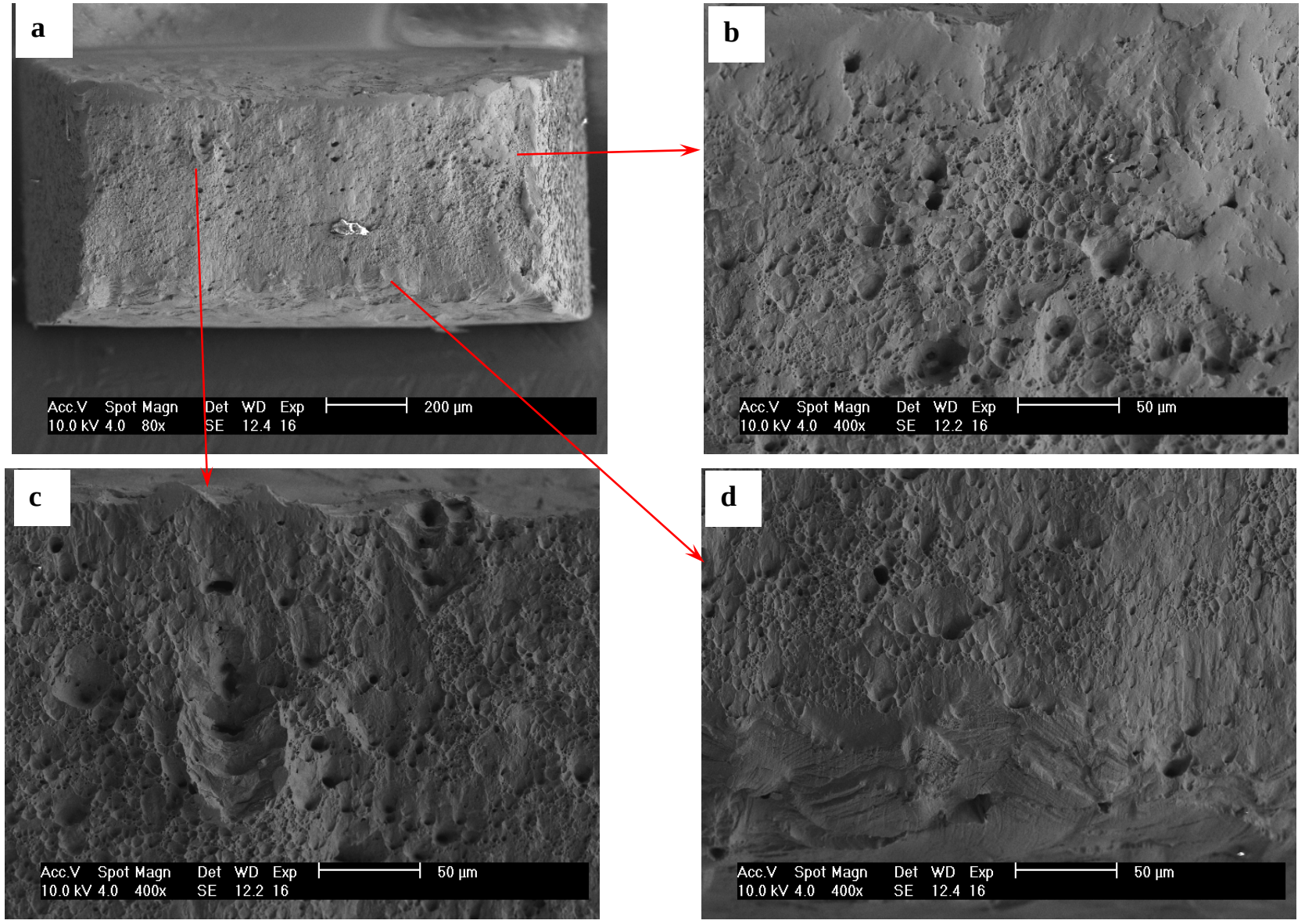

Figure 21. Fracture surface of SA Type 304L SS irradiated to 9.6 dpa and tested in PWR water (specimen A10-2).

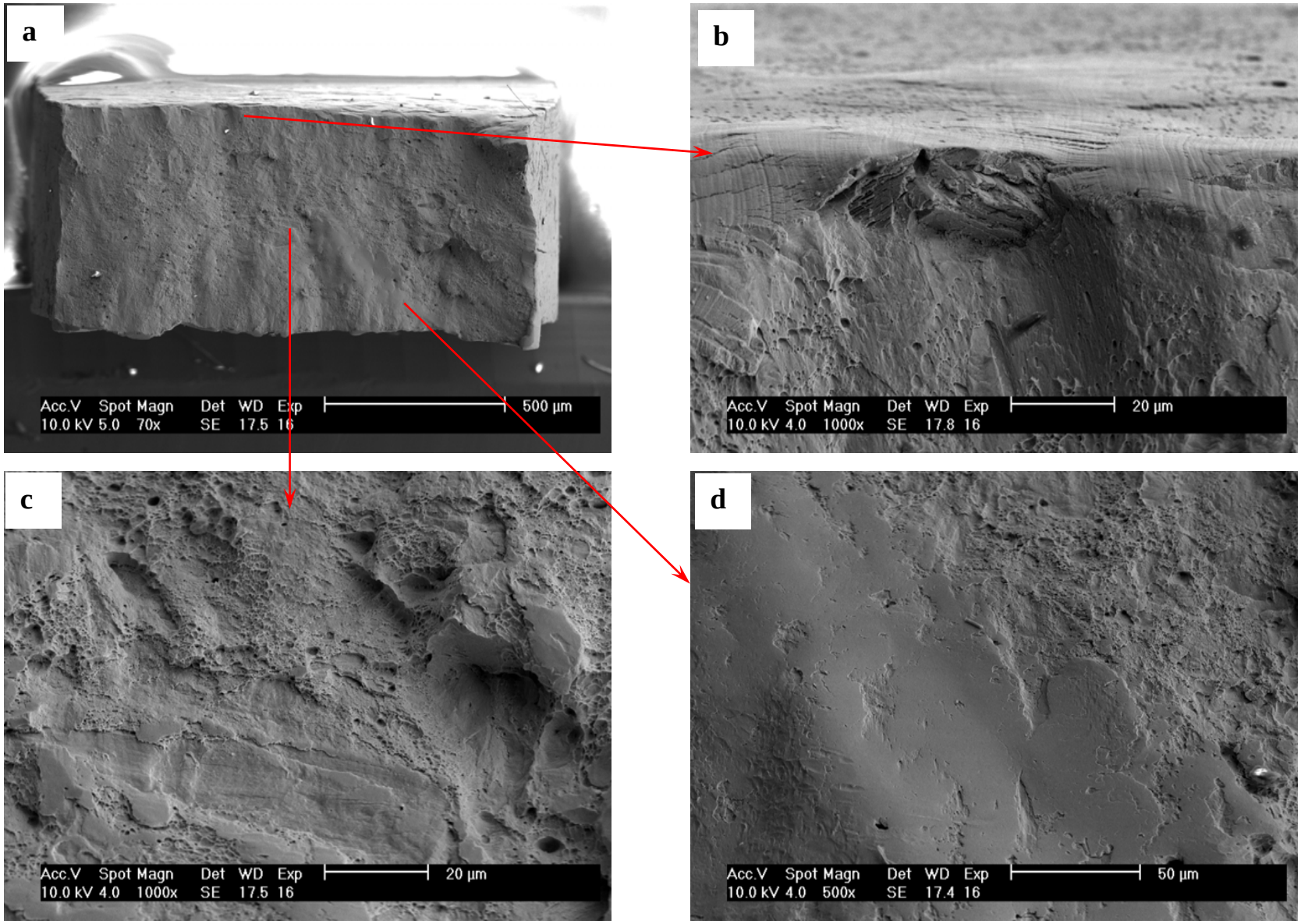

Figure 22. Fracture surface of CW Type 304L SS irradiated to 9.1 dpa and tested in PWR water (specimen A11-2).

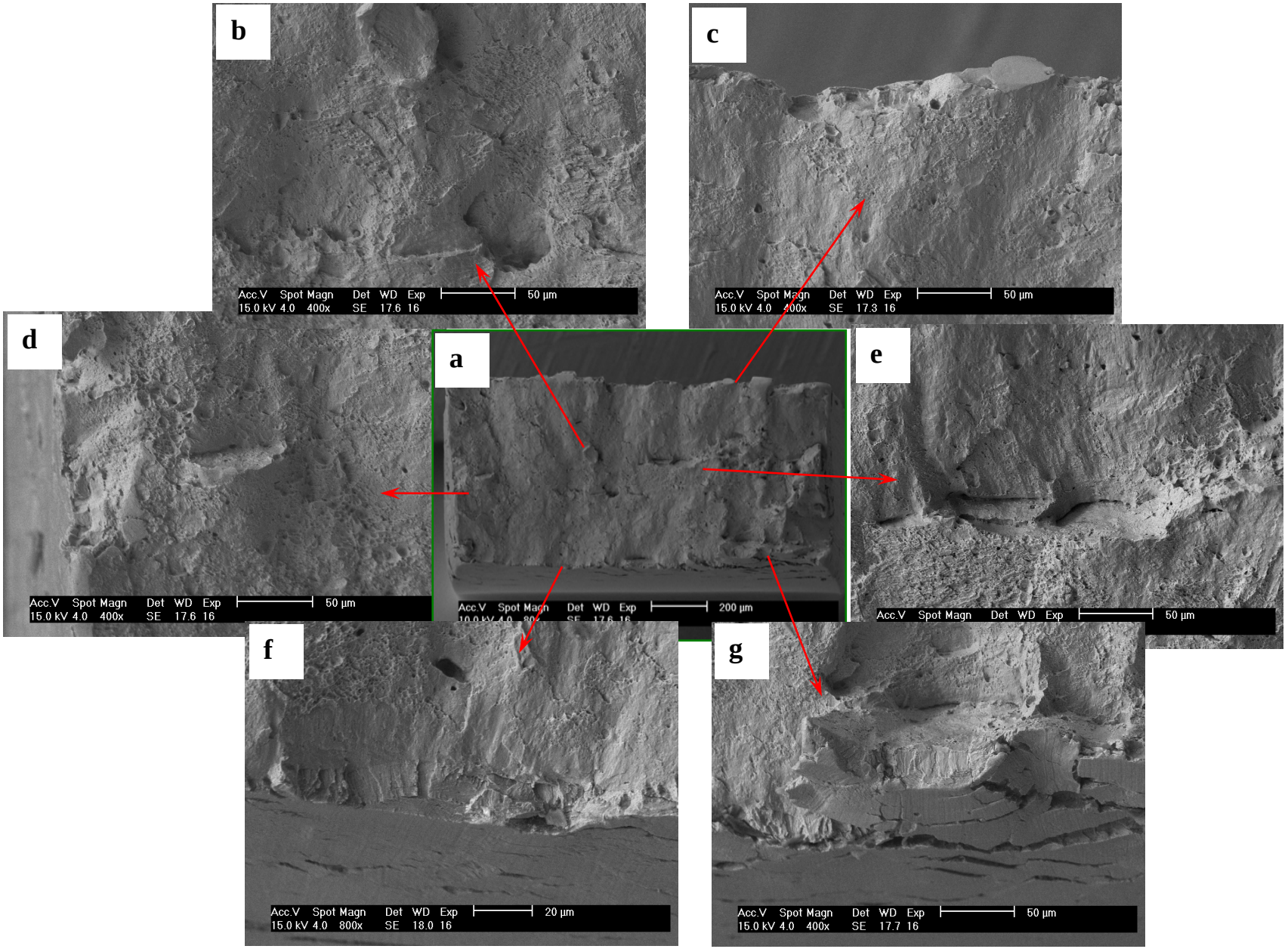

Figure 23. Fracture surface of CW Type 304L SS irradiated to 47.5 dpa and tested in PWR water (specimen A11-4).

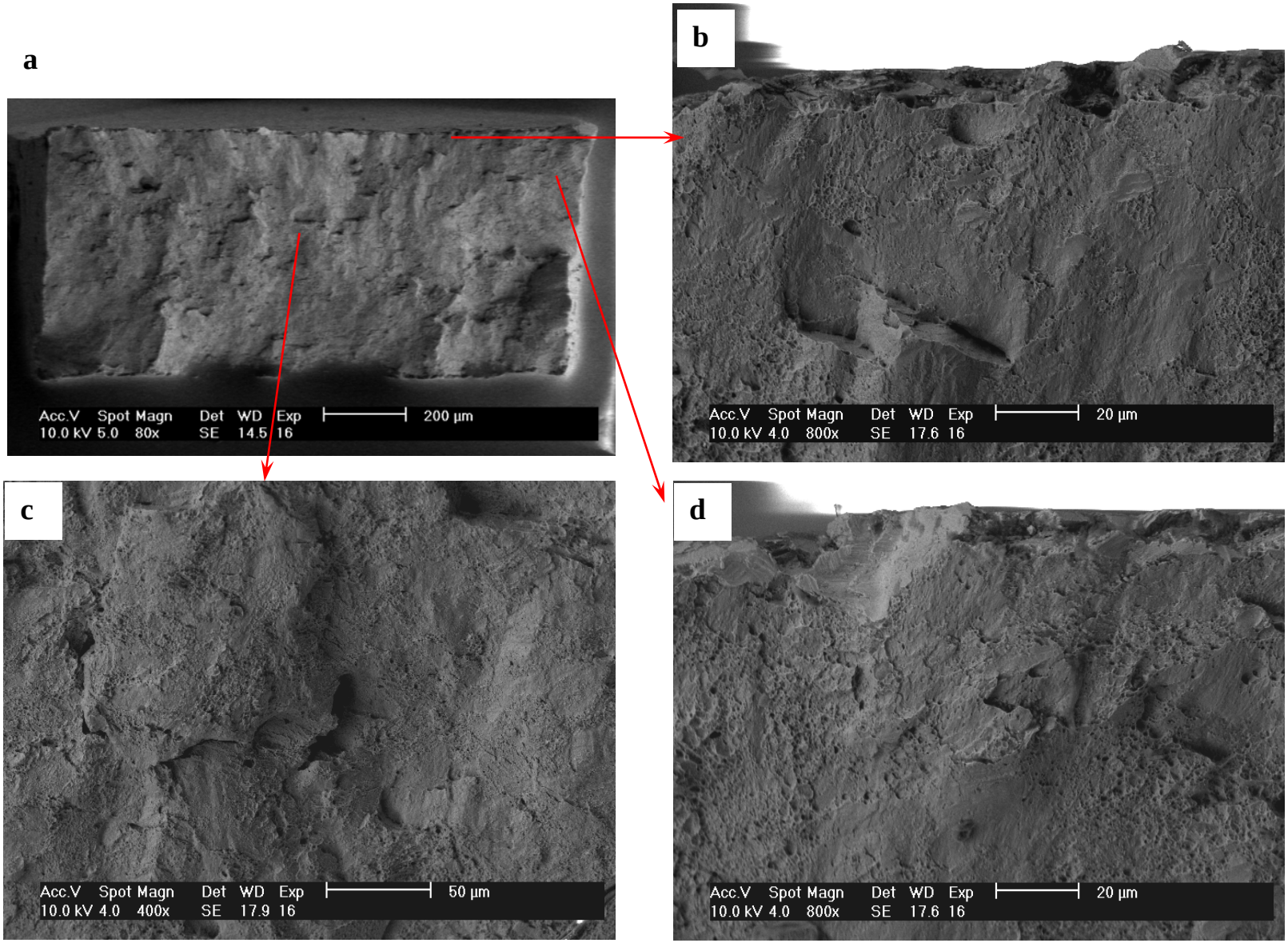

Figure 24. Fracture surface of CW Type 304 SS irradiated to 47.5 dpa and tested in PWR water (specimen A5-4).

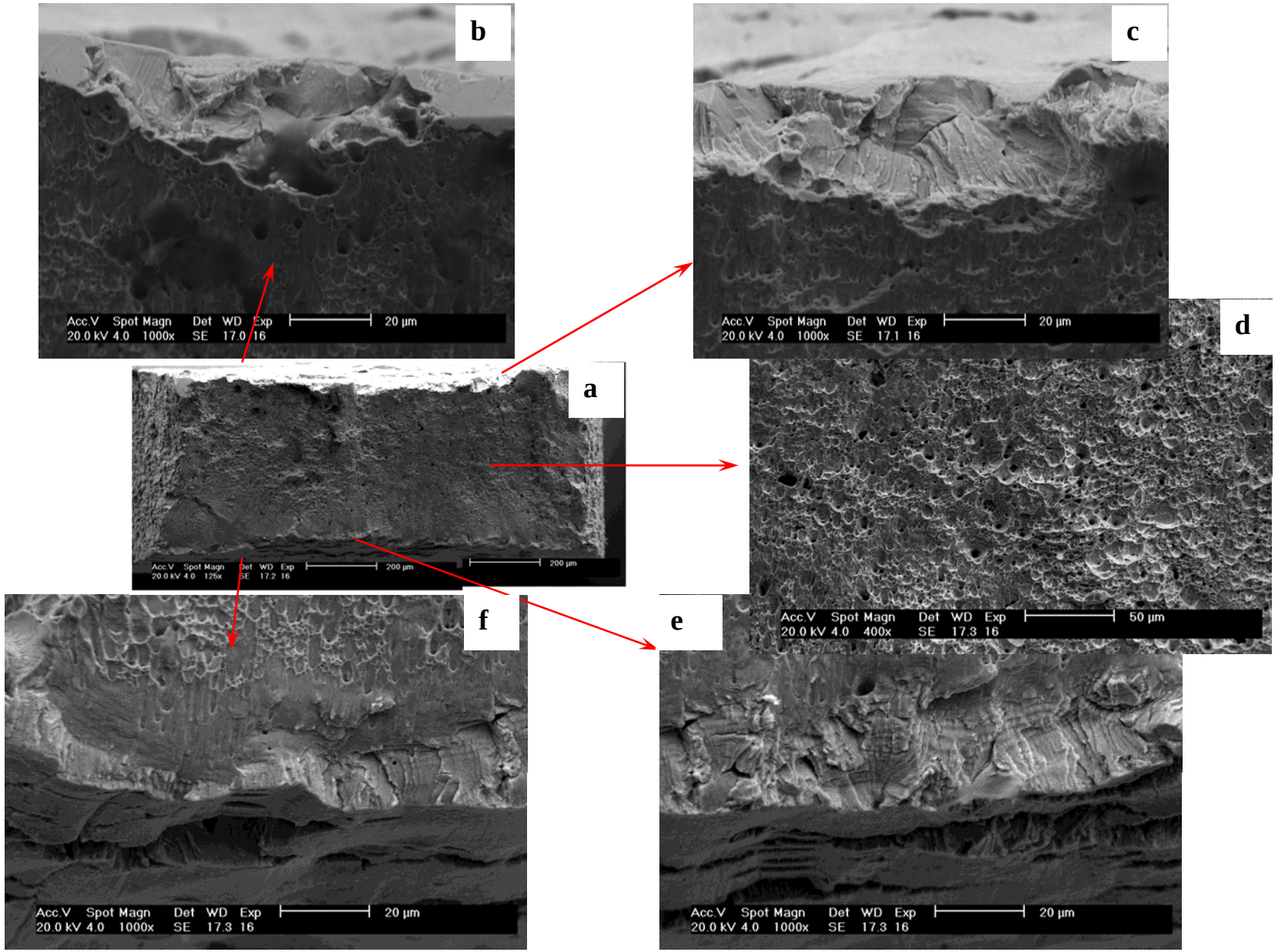

Figure 25. Fracture surface of an SA 304-like model alloy irradiated to 9.1 dpa and tested in PWR water (specimen A12-2).

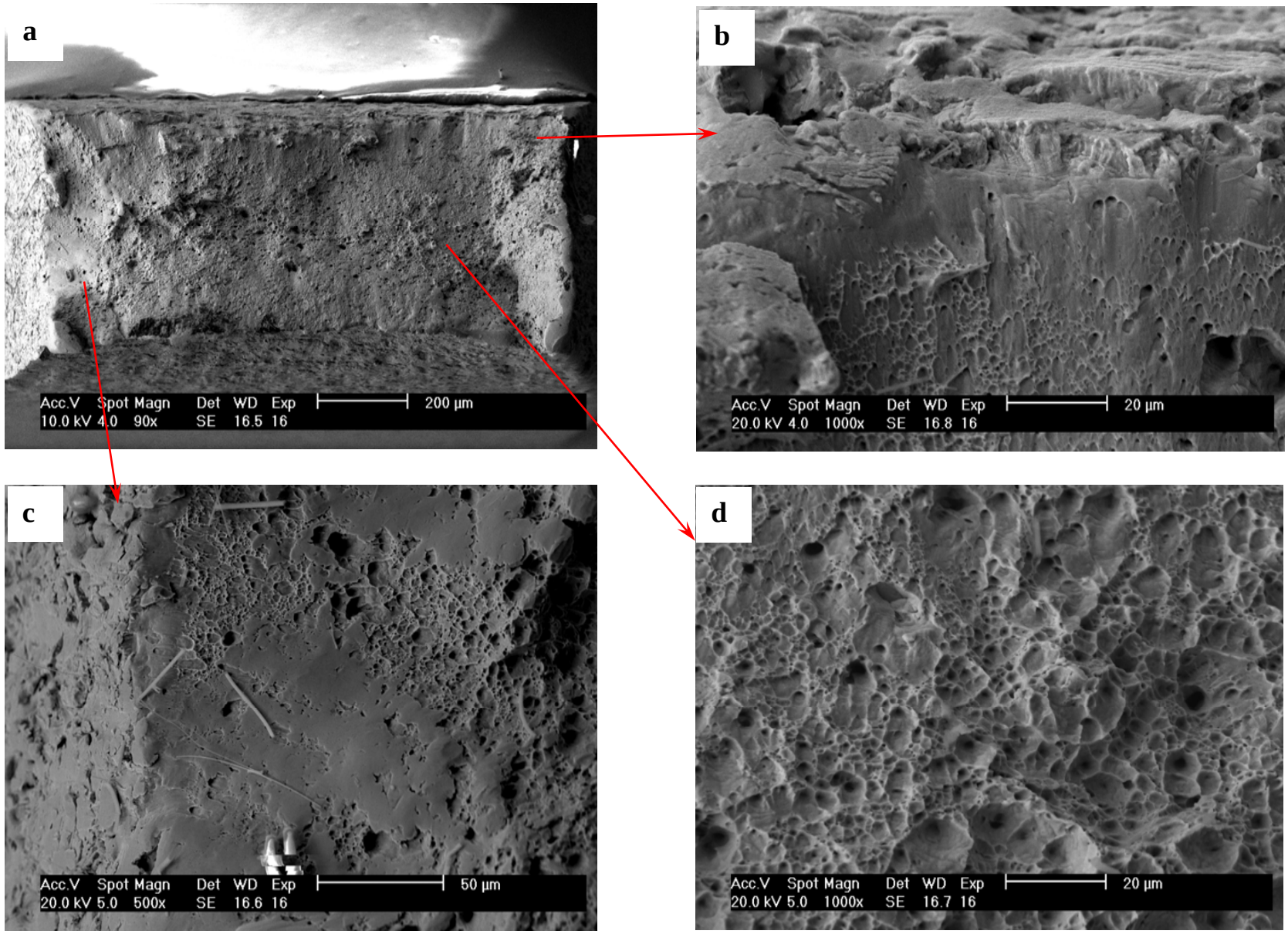

Figure 26. Fracture surface of an SA 304-like model alloy irradiated to 47.5 dpa and tested in PWR water (specimen A12-4).

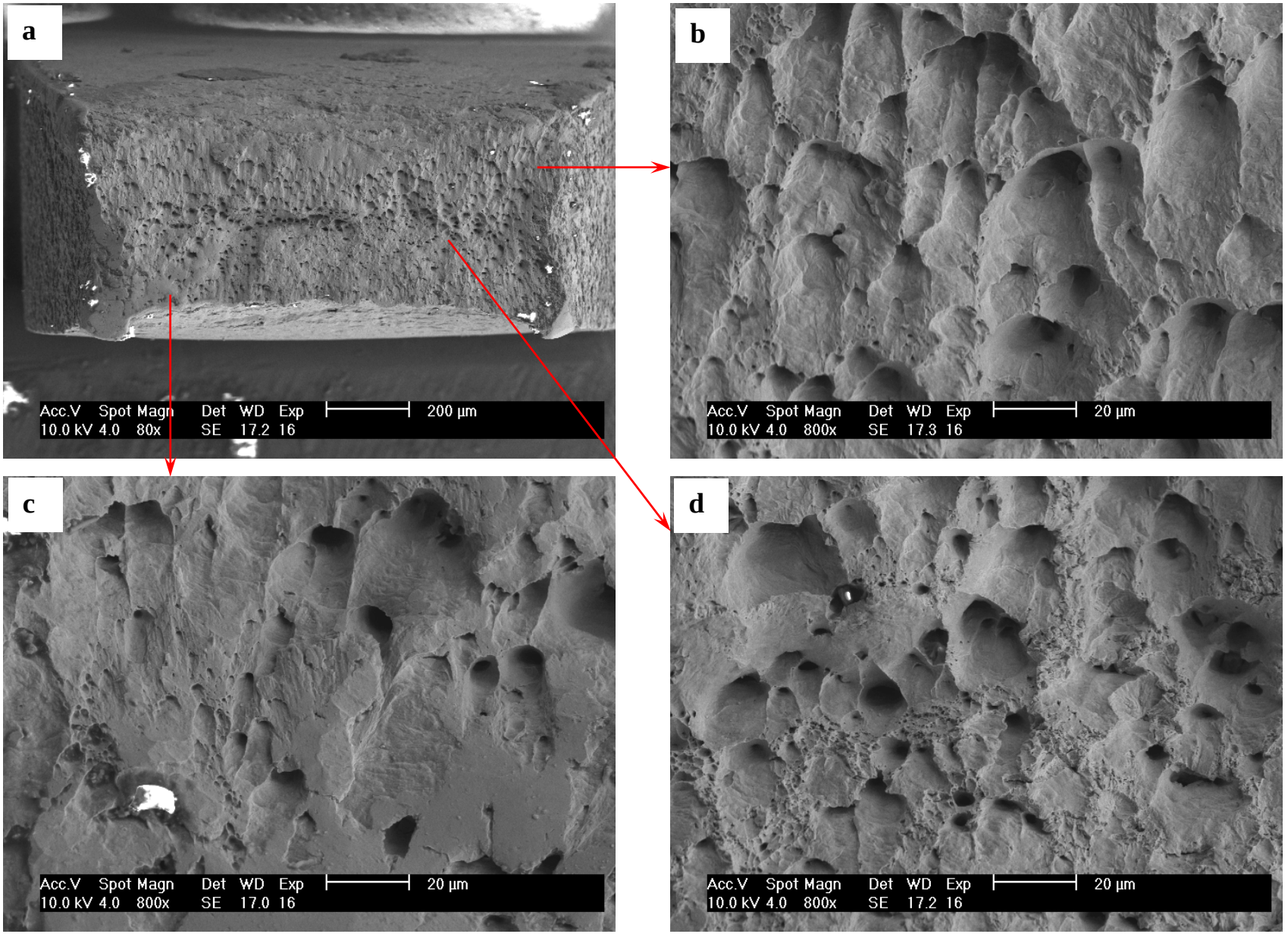

Figure 27. Fracture surface of SA HP 304L SS with high-O irradiated to 9.6 dpa and tested in PWR water (specimen A8-2).

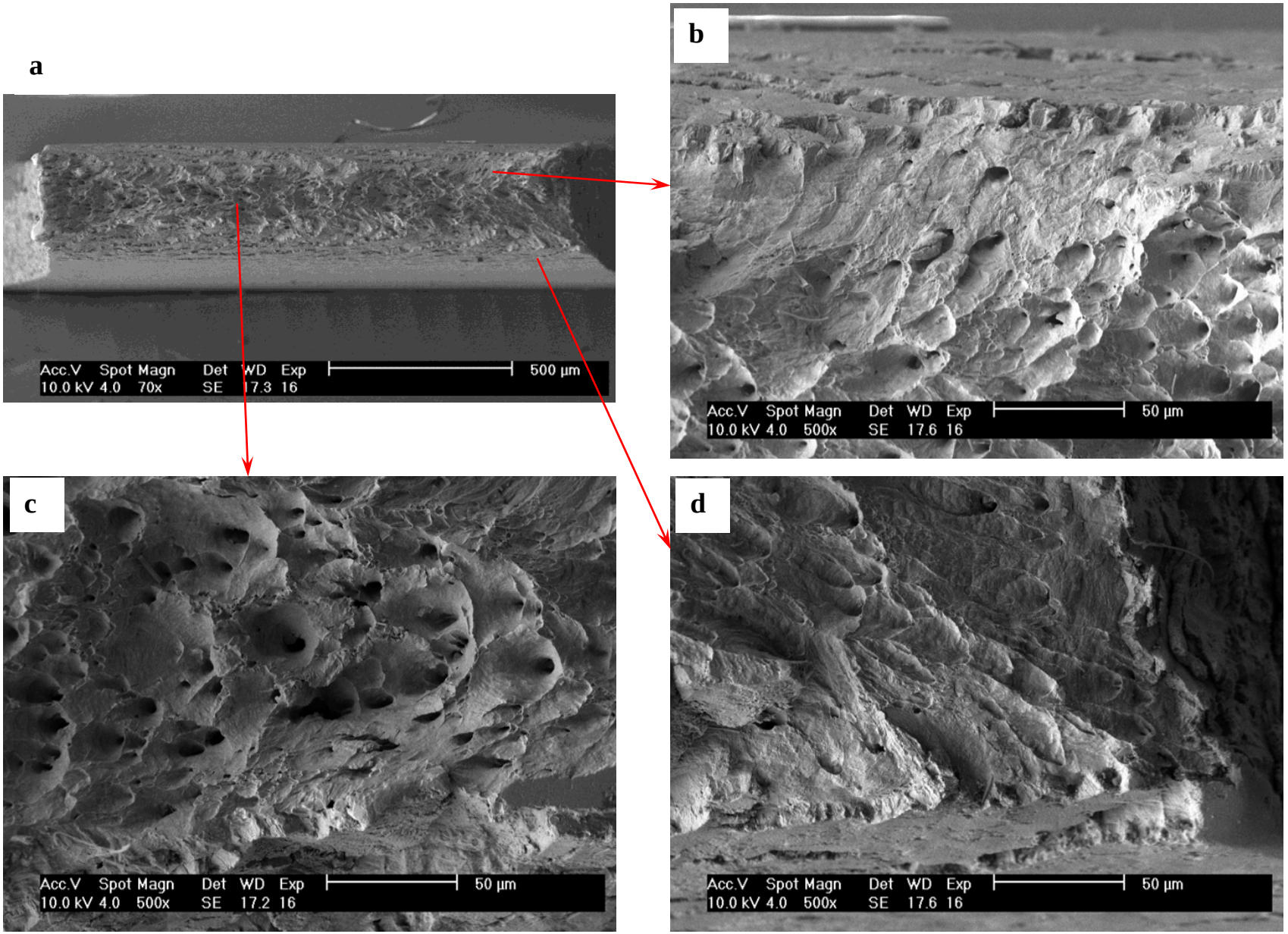

Figure 28. Fracture surface of SA HP 304L SS with high-O irradiated to 47.5 dpa and tested in PWR water (specimen A8-4).

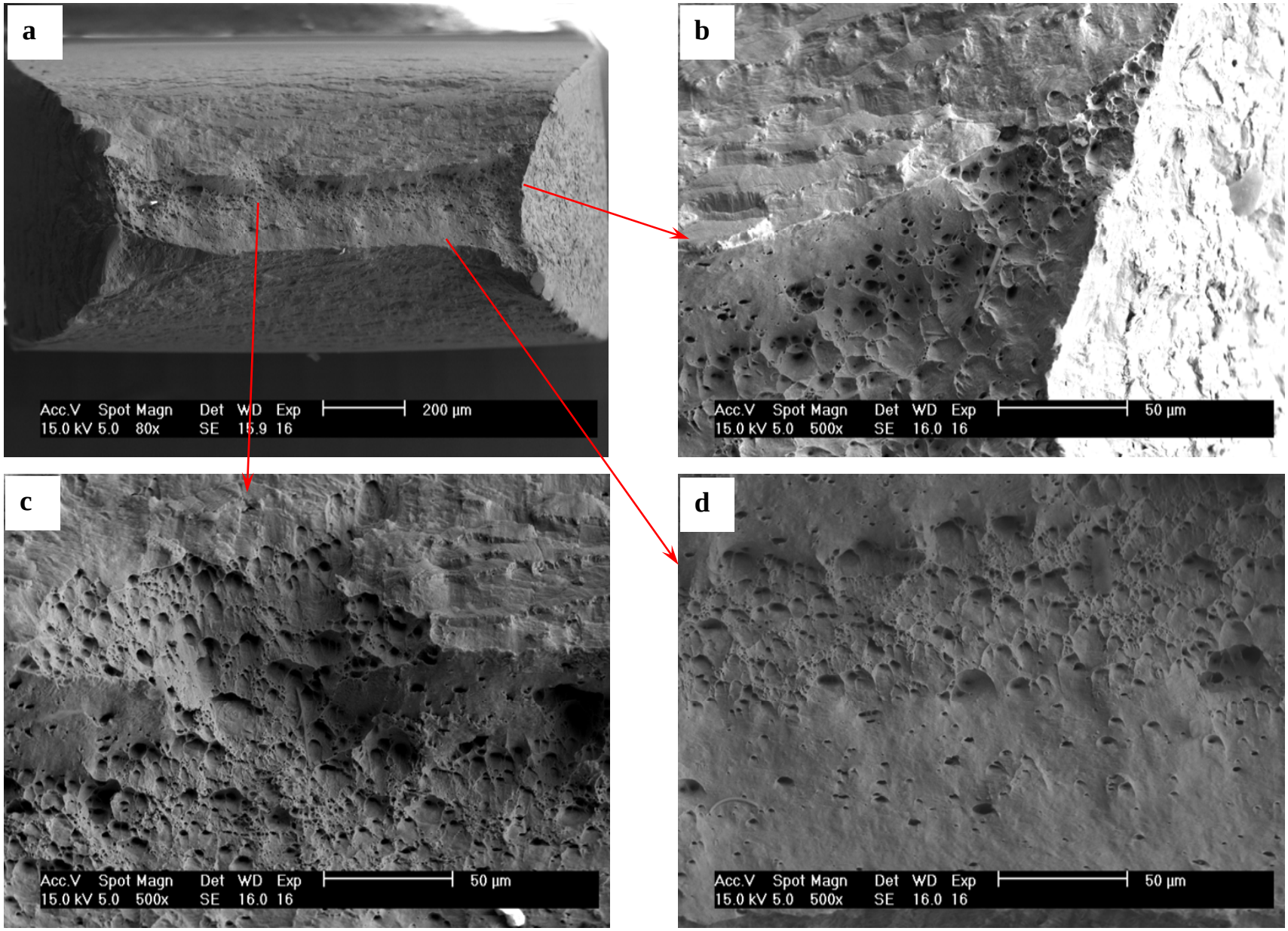

Figure 29. Fracture surface of SA HP 304L SS with low-O irradiated to 9.6 dpa and tested in PWR water (specimen A9-2).

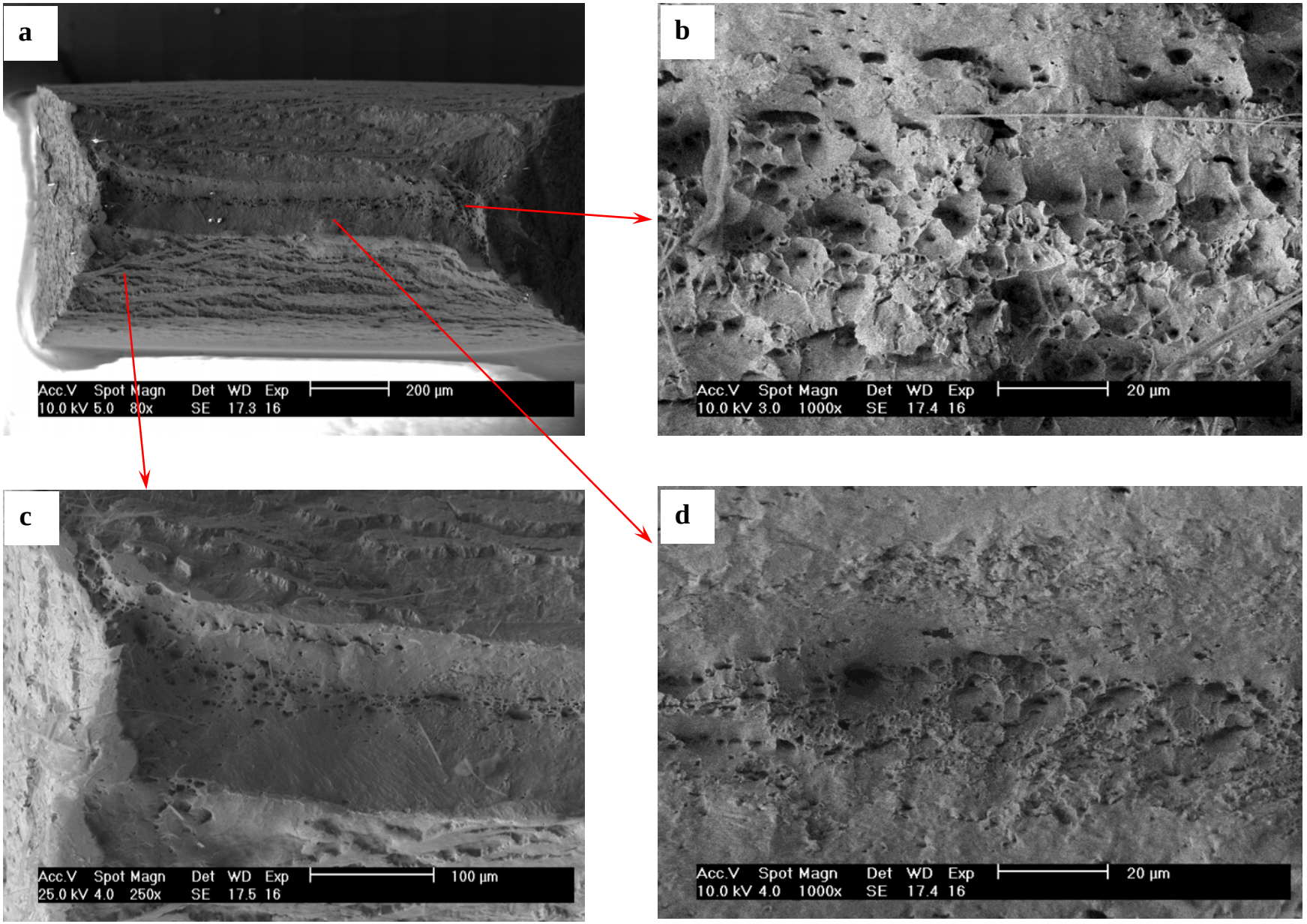

Figure 30. Fracture surface of SA HP 304L SS with low-O irradiated to 47.5 dpa and tested in PWR water (specimen A9-4).

3.4 SSRT Tests in PWR Water on Type 347 SSs

Four SSRT tests were performed on SA and CW Type 347 SSs in a PWR environment at 315°C and a constant strain rate of 7.4×10^{-7} s^{-1}. The SA samples were tested at three doses (5.5, 10.2, and 45 dpa), and the CW was tested at 10.2 dpa. Figure 31 shows the stress-strain curves obtained from these tests, and the tensile results are also summarized in Table 7.

For the SA specimens, the irradiated YS increases from 5.5 to 10.2 dpa but declines slightly from 10.2 to 45 dpa. No strain hardening can be seen in all SA specimens, and the flow stress continues to decrease beyond yield in the SSRT tests. It is of note that the test on the 10.2-dpa specimen was interrupted because of a problem with the autoclave temperature (the green curve in Fig. 31). Thus, the TE and TF reported for this test are estimated values. Compared to the 5.5- and 10.2-dpa tests, a well-defined yield point can be seen in the 45-dpa test followed by a more rapid decline in flow stress (the orange curve in Fig. 31). For the CW Type 347 SS, the test was conducted at 10.2 dpa only (the blue curve in Fig. 31). The YS of the CW sample is much higher than that of the SA sample at the same dose. Limited strain hardening is also observed for the CW sample, and the TE is shorter than for any of the SA samples.

Table 7. Slow-strain-rate tensile tests on Type 347 SS in PWR water at 315-320°C.

Material Type	Heat Treatment	Spec. ID	Dose (dpa)	YS [a] (MPa)	UTS [a] (MPa)	TE [a] (%)	RA [a] (%)	Time to failure (hr)
347	SA	D1-1	5.5	638	638	6.17	51	46
347	SA	D1-2	10.2	760	760	(5.95) [b]	51	(40) [b]
347	SA	D1-4	45	718	718	4.72	44	30
347	CW	D2-3	10.2	868	1040	3.39	33	37

[a] YS = yield strength; UTS = ultimate tensile strength; TE = total elongation; RA = reduction of area.
[b] Estimated values. Autoclave temperature tripped during the test.

Fracture surfaces of the SA and CW Type 347 SS are shown in Figs. 32-34. Ductile dimples are still the major microstructural features on the fracture surfaces. While fine dimples resulting from microvoid coalescence cover the most dimple fracture regions, some large dimples likely associated with pre-existing inclusions can also be seen in all Type 347 specimens. Besides dimples, brittle cracking areas are also observed on the fracture surfaces. For the SA 5.5-dpa specimen, small isolated cleavage cracking (~50 μm) with typical river patters and cleavage steps are found at sample surface in contact with water (Fig. 32b-d). The development of cleavage cracking at such a low dose and low stress suggests a poor resistant of this material to cracking. The same type of cracking is also seen in the 10.2-dpa SA sample, as shown in Fig. 33. The cracking areas remain small at this dose level and are surrounded by fine dimples, as shown in Fig. 33b. The fracture surface of the CW 10.2-dpa 347 SS is shown in Fig. 34. Compared with the SA sample at the same dose, cleavage cracking is more extensive (Fig. 34b,d), suggesting a detrimental effect of cold-work. At 45 dpa, more than half of the fracture surface of the SA 347 SS is covered by brittle cracking, as shown in Fig. 35. The morphology of the cracking area is poorly defined and is a mixture of transgranular cracking, cleavage steps, and IG facets. Some shear dimples can also be seen between TG areas in Fig. 35c. The extent of cracking of this SA sample is more severe than that of the other SSs examined in this study, suggesting a high susceptibility to cracking of Type 347 SS in PWR water at 45 dpa.

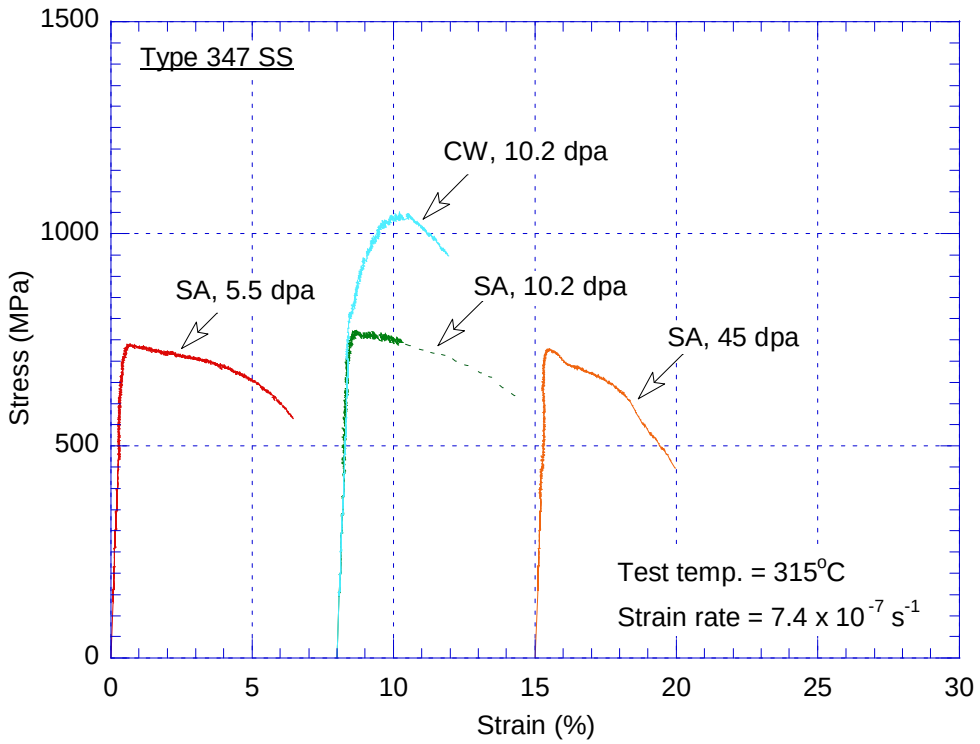

Figure 31. Stress-vs.-strain curves of SSRT tests on Type 347 SS in PWR water at 315°C (the dashed line for the SA 10.2-dpa sample is estimated).

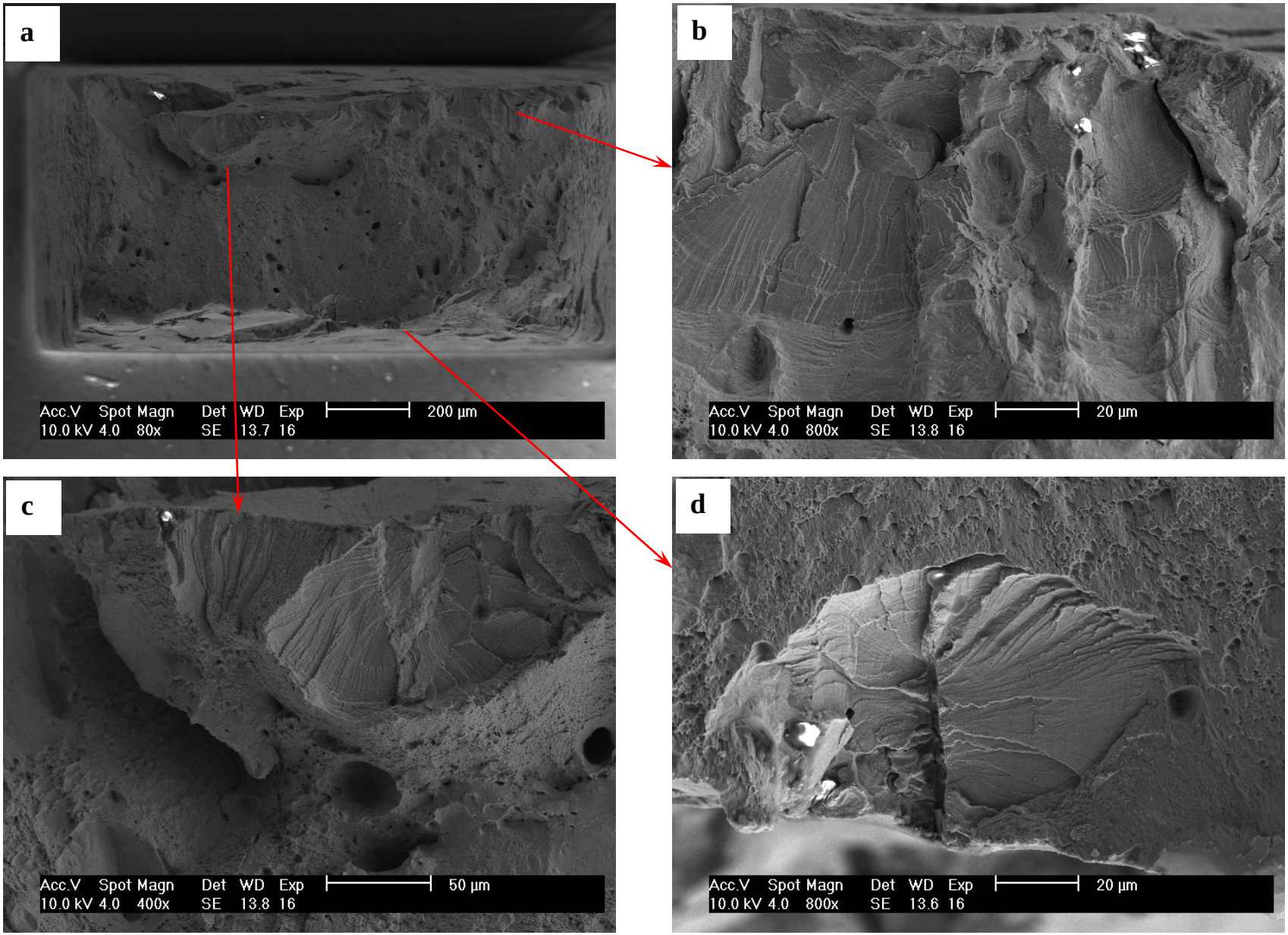

Figure 32. Fracture surface of SA Type 347 SS irradiated to 5.5 dpa and tested in PWR water (specimen D1-1).

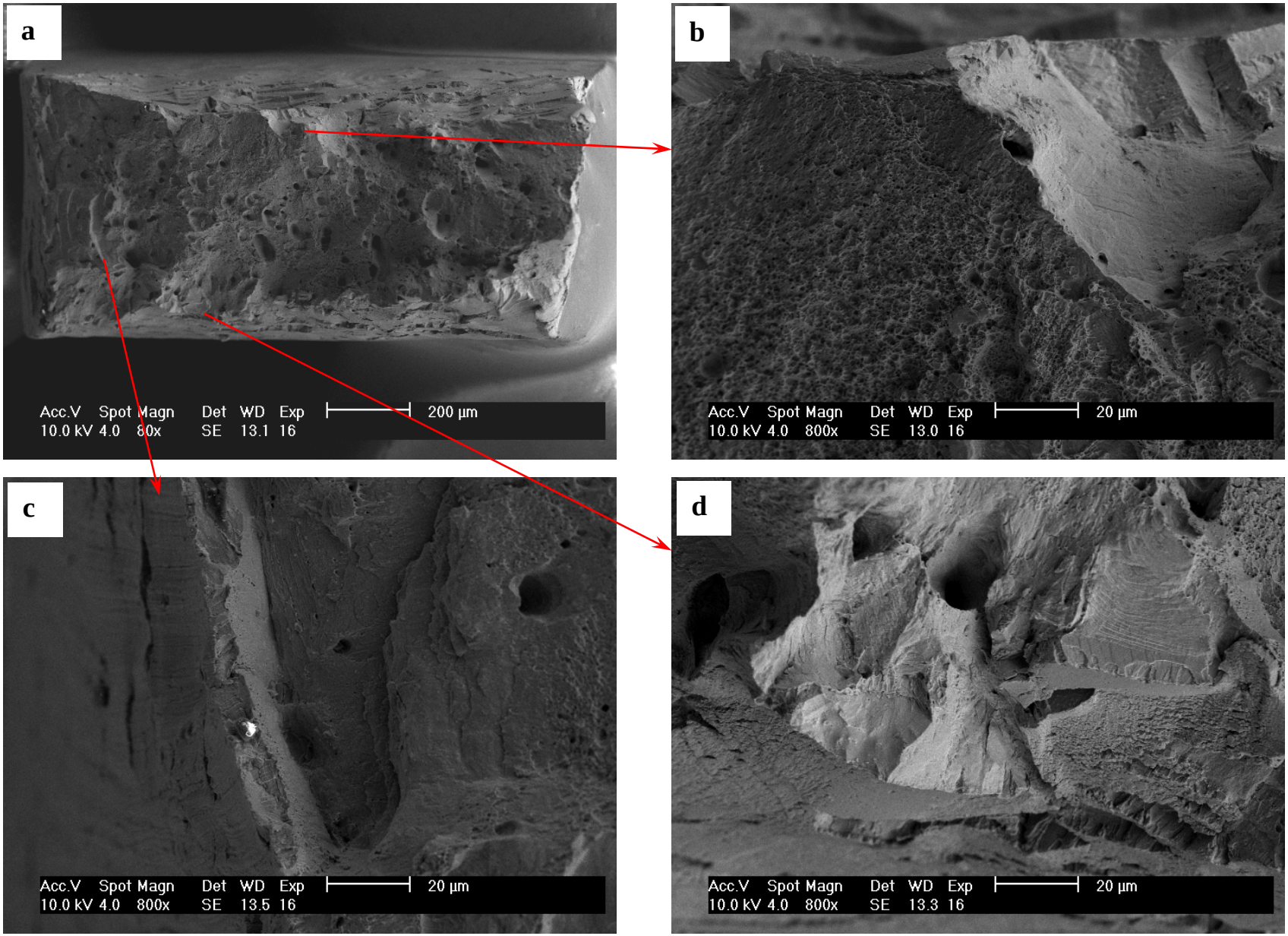

Figure 33. Fracture surface of SA Type 347 SS irradiated to 10.2 dpa and tested in PWR water (specimen D1-2).

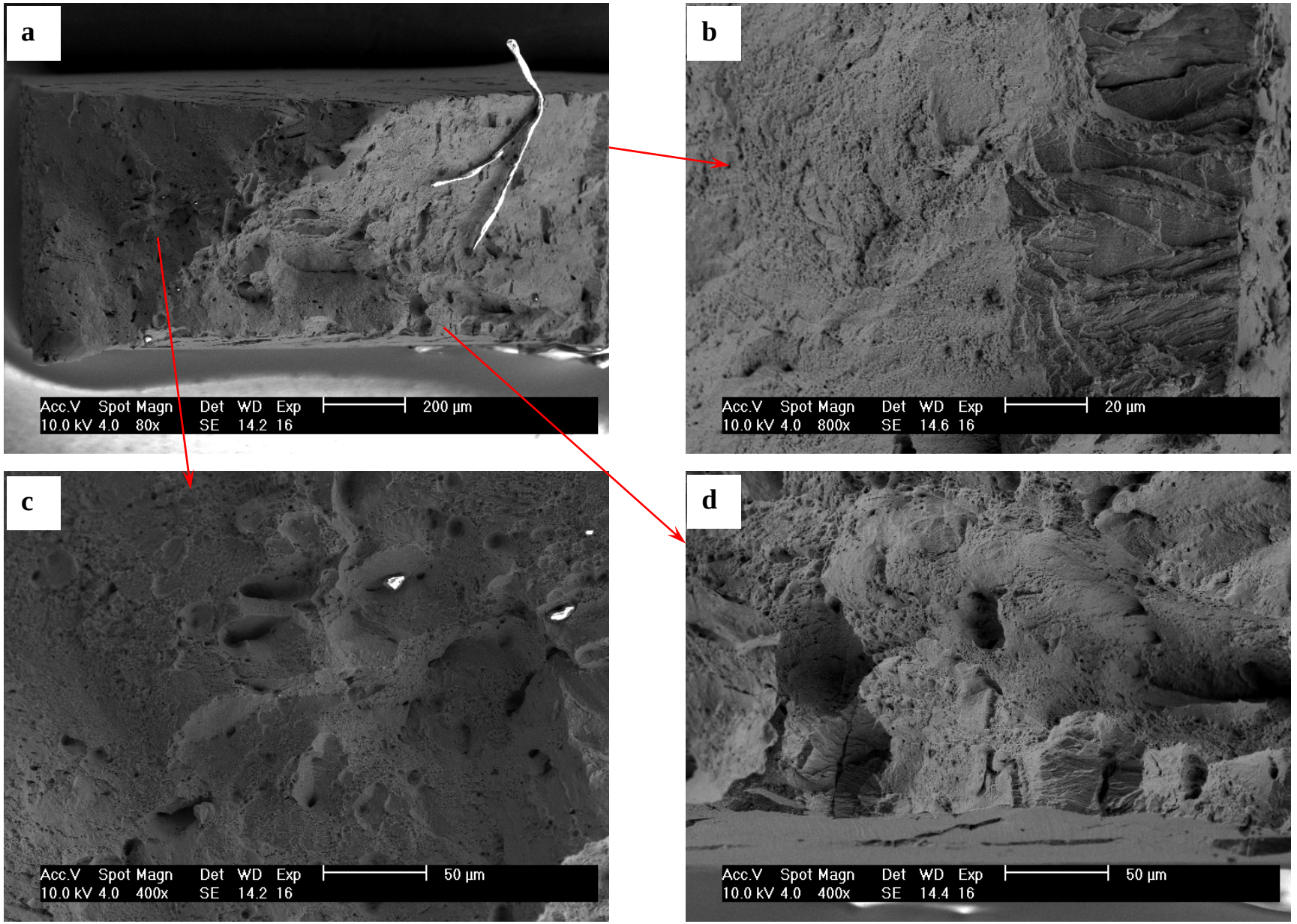

Figure 34. Fracture surface of CW Type 347 SS irradiated to 10.2 dpa and tested in PWR water (specimen D2-3).

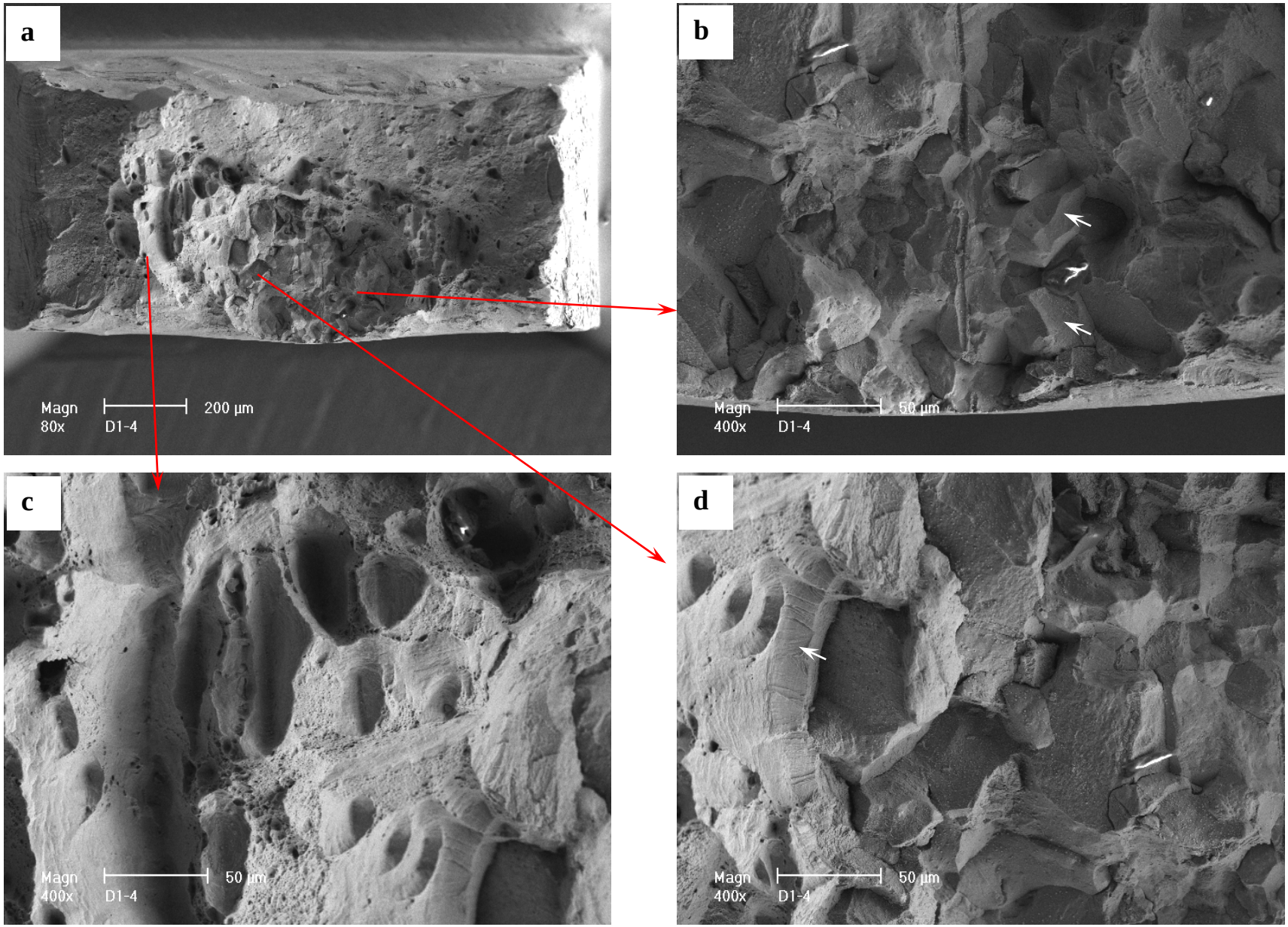

Figure 35. Fracture surface of SA Type 347 SS irradiated to 45 dpa and tested in PWR water (specimen D1-4).

3.5 SSRT Tests in PWR Water on GBE Alloys

The effect of GBE treatment was evaluated for Types 304, 316 SSs and Alloy 690. Three pairs of GBE/non-GBE specimens were tested in the PWR environment at 315°C. Among them, Types 304 and 316 SSs were evaluated at ~5 dpa, and Alloy 690 was evaluated at ~5 and 9.6 dpa. Figure 36 shows the stress-strain curves obtained from these tests, and the tensile results are summarized in Table 8.

Grain-boundary engineering, or GBE, is a thermal-mechanical treatment that involves a series of deformation-annealing iterations to systematically increase the population of coincident site lattice (CSL) boundaries in materials. A GBE treatment is considered beneficial for IG resistance because CSL boundaries have much lower interface energies than those of random high-angle grain boundaries. It has been shown that the low-Σ^* CSL boundaries in this study were approximately 60% for GBE 304 and 316 SSs and 70% for GBE 690.[26] The red curves in Fig. 36 are the GBE alloys, and the green curves are the non-GBE base materials (in SA conditions). For Types 304 and 316 SSs, well-defined yield points can be seen in the tests, and no strain hardening is observed at ~5 dpa (Fig. 36a). While the GBE SSs have slightly lower YSs, the TEs of GBE 304 and 316 SSs are about 32% and 69%, respectively — higher than their non-GBE base alloys. This effect of GBE on elongation suggests that the GBE treatment may be beneficial for the SSRT behaviors of Types 304 and 316 SSs in PWR water.

For Alloy 690, a small amount of strain hardening remains at ~5 and 9.6 dpa for both GBE and non-GBE materials (Fig. 36b). The YS and UTS of GBE 690 are slightly lower than that of Alloy 690 at both doses. The TE of GBE 690 is also 10% greater at ~5 dpa and 5% greater at 9.6 dpa. While the beneficial effect of GBE treatment is still present at both doses, the effect seems to be weakening with increasing dose for Alloy 690.

Table 8. Slow-strain-rate tensile tests on alloys with and without GBE treatment in PWR water at 315-320°C.

Material Type	Heat Treatment	Spec. ID	Dose (dpa)	YS [a] (MPa)	UTS [a] (MPa)	TE [a] (%)	RA [a] (%)	Time to failure (hr)
304	GBE	A6-1	5.5	796	796	8.38	81	45
304	SA	A7-1	4.8	825	825	6.34	51	45
316	GBE	B8-1	5.5	753	753	11.5	49	66
316	SA	B9-1	4.8	813	813	6.81	48	45
A690	GBE	E1-1	5.5	812	835	9.8	58	55
A690	GBE	E1-2	9.6	825	845	8.44	61	54
A690	SA	E2-1	4.8	840	860	8.9	59	53
A690	SA	E2-2	9.6	840	860	8.0	62	55

[a] YS = yield strength; UTS = ultimate tensile strength; TE = total elongation; RA = reduction of area.

[*] Σ is the reciprocal of the fraction of coincident sites, which defines the geometrical relation between the two neighbor grains.

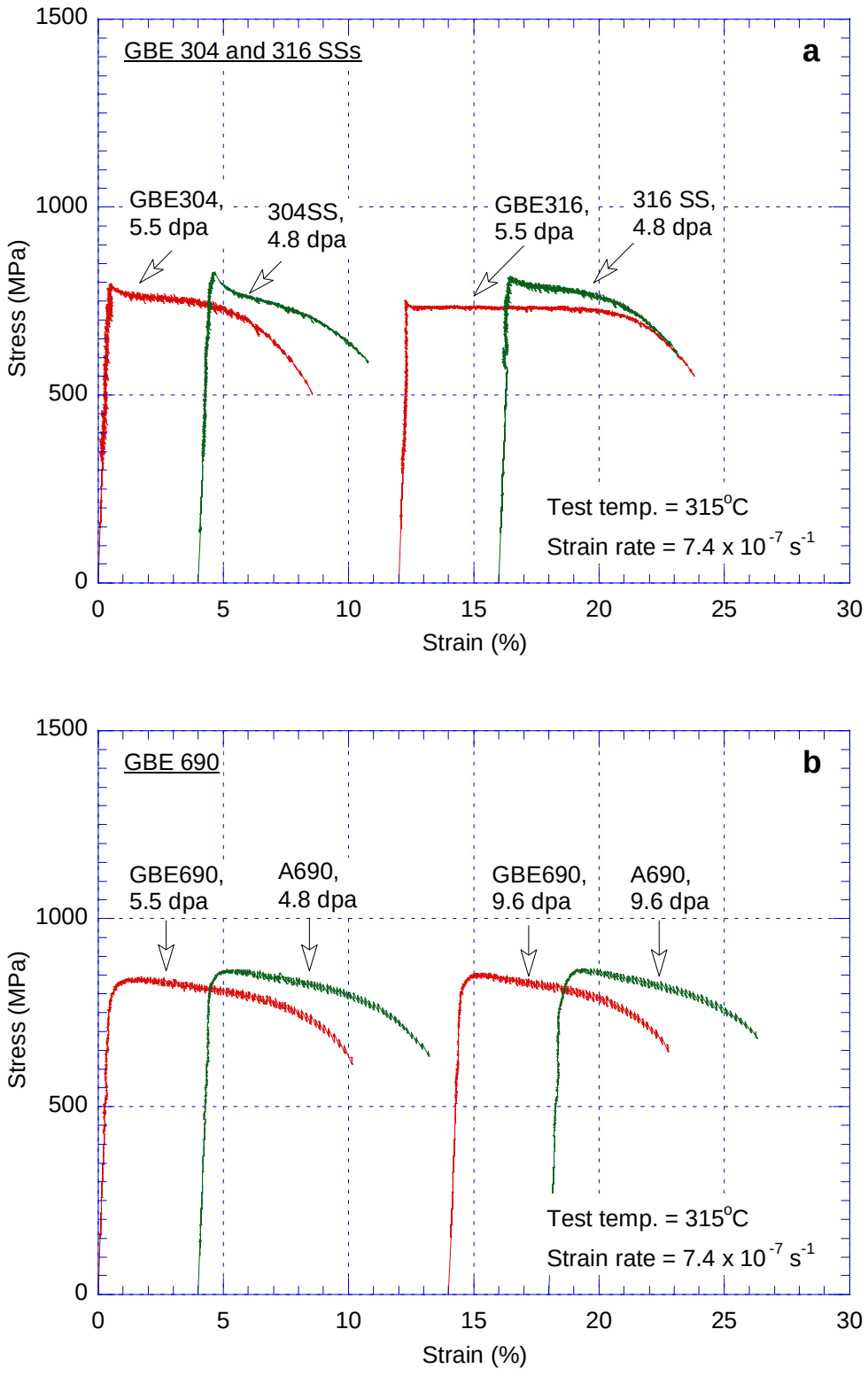

Figure 36. Stress-vs.-strain curves of SSRT tests on (a) GBE 304 and 316 SSs, and (b) Alloy 690 in PWR water at 315°C.

The fracture surfaces of GBE and non-GBE base alloys are shown in Figs. 37-44. For Type 304 SS, the main fracture morphology is ductile dimples, and isolated and shallow cleavage cracks are observed for both GBE and non-GBE base specimens at ~5 dpa. The cracks are less than 50 μm deep, and limited to sample skin in contact with water. Although slightly more cracking areas can be seen in the GBE 304 specimen, it seems to have no impact on the overall plasticity. In fact, the GBE 304 specimen (Fig. 37) shows a higher RA than that of the 304 SS (Fig. 38). The fracture surfaces are also similar for GBE and non-GBE 316 SS at ~5 dpa. Ductile dimple fracture is the dominant morphology, and isolated cleavage cracking areas can be seen on the sample surfaces (Figs. 39b-c and 40b-c). It appears that the dimples of the GBE 316 specimen are larger than those of the non-GBE 316 specimen (Figs. 39d and 40d). Despite this difference, the measured RAs are nearly identical for both the GBE and non-GBE 316 SSs.

For the GBE and non-GBE 690 specimens, the fracture surfaces are almost entirely covered by dimples at both ~5 and 9.6 dpa (Figs. 41-44). Spherical and elongated dimples can be seen even at sample surfaces (Figs. 41c, 42d, 43c, and 44b-c). No brittle cracking is observed except at the center of the 9.6-dpa non-GBE 690 specimen where a severe triaxial state of stress may have developed (Fig. 44d). The lack of cracking on the sample surfaces suggests a good resistance to crack initiation for these alloys in PWR environments.

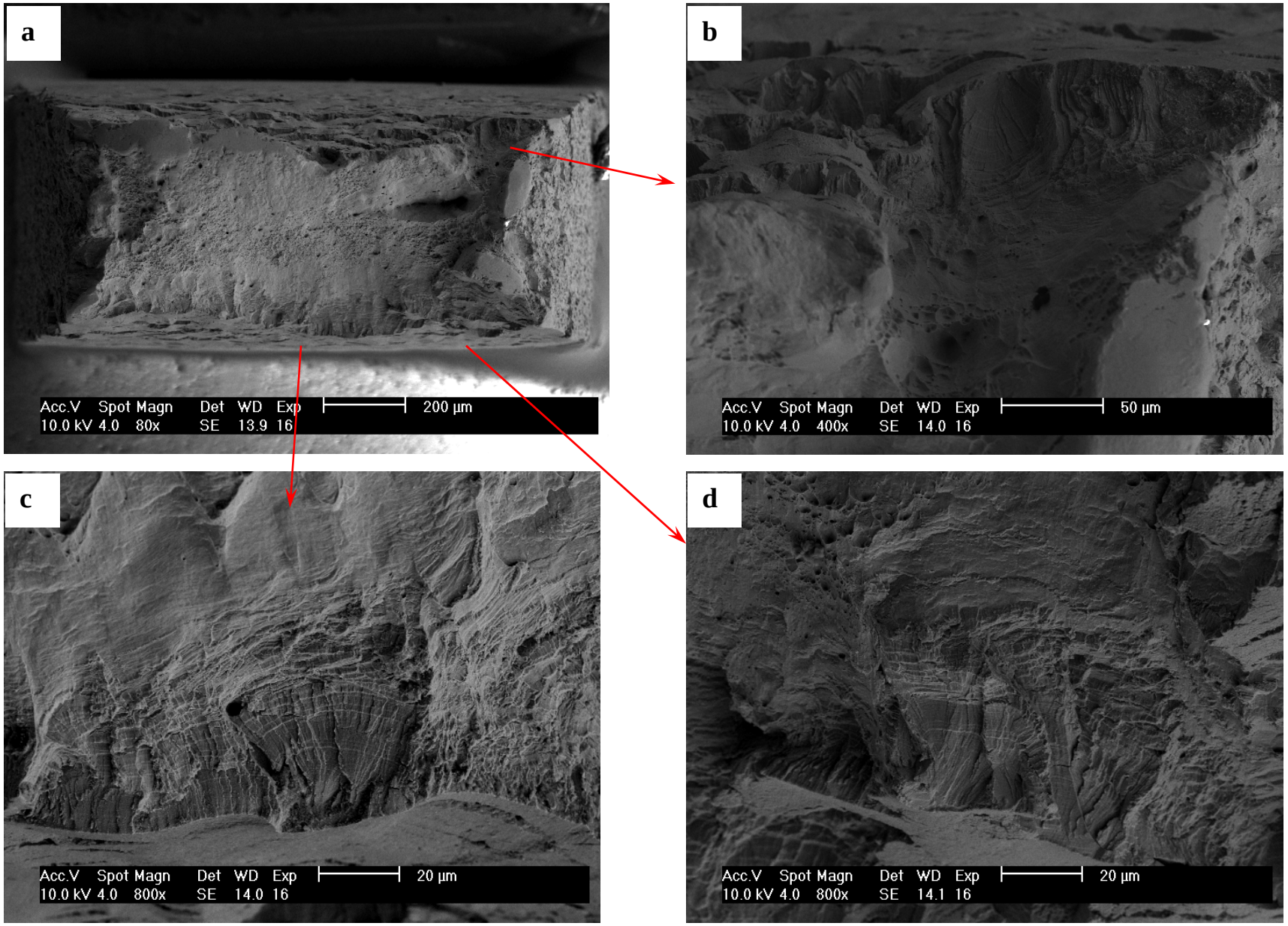

Figure 37. Fracture surface of GBE 304 SS irradiated to 5.5 dpa and tested in PWR water (specimen A6-1).

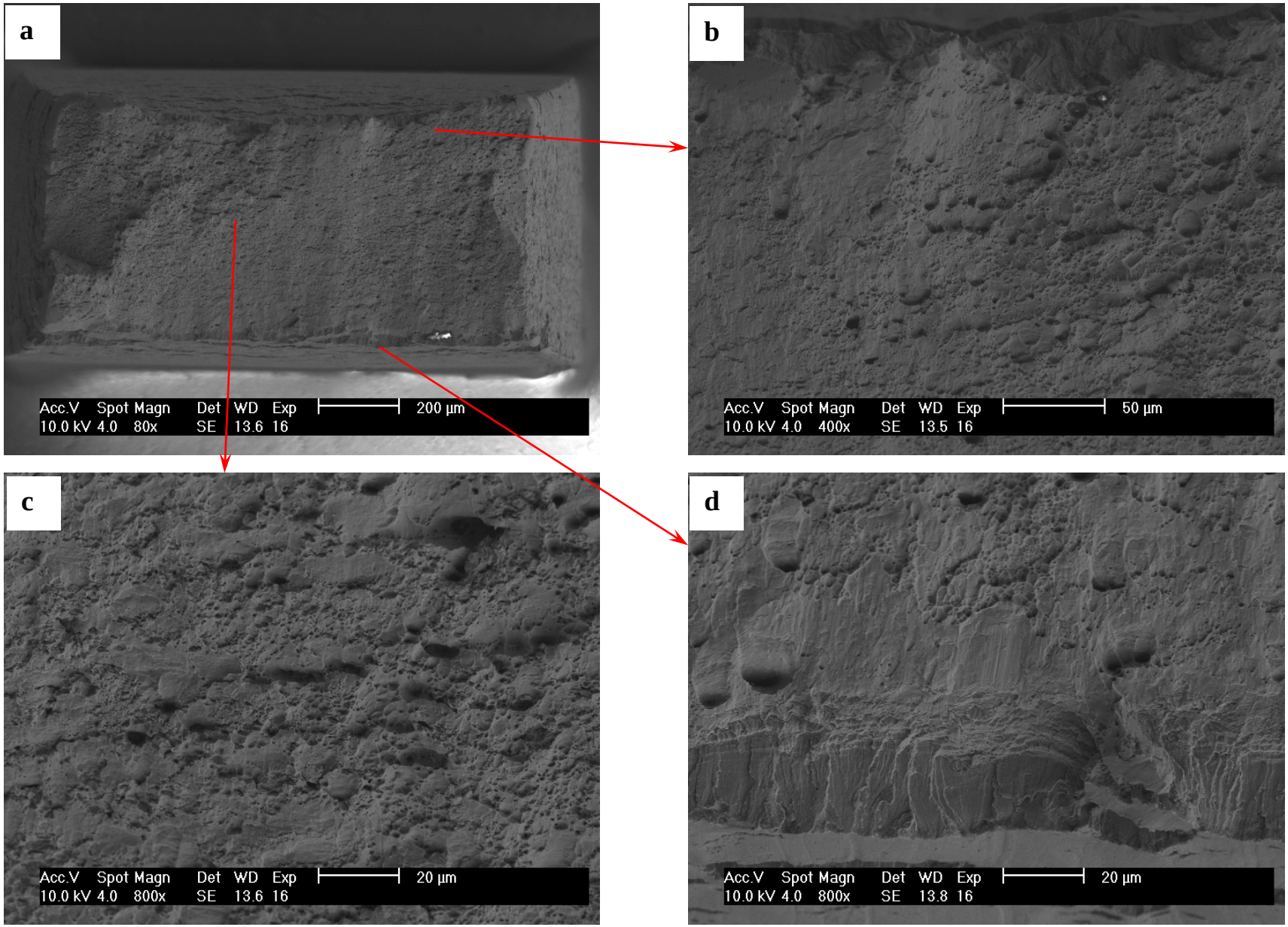

Figure 38. Fracture surface of SA 304 SS irradiated to 4.8 dpa and tested in PWR water (specimen A7-1).

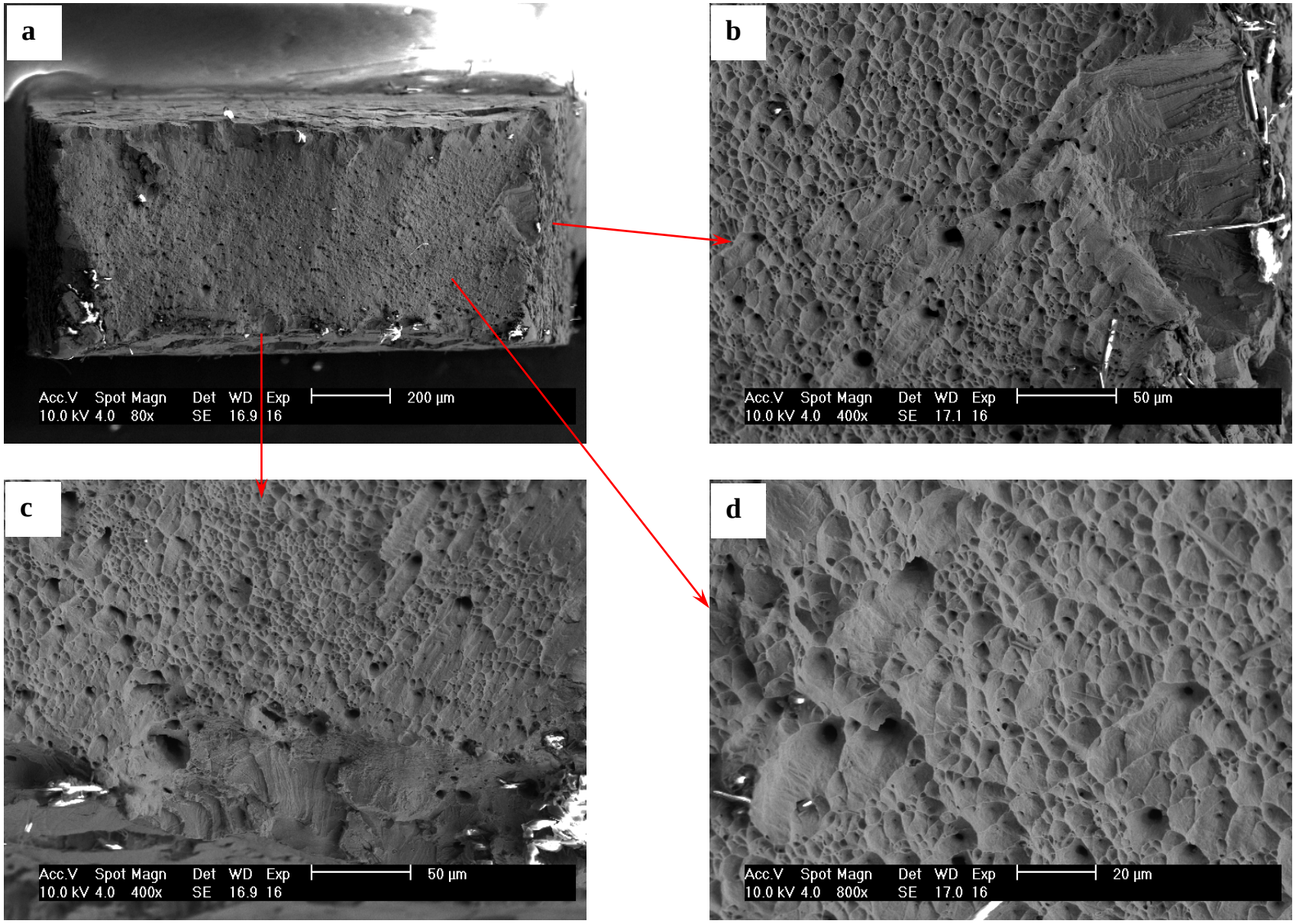

Figure 39. Fracture surface of GBE 316 SS irradiated to 5.5 dpa and tested in PWR water (specimen B8-1).

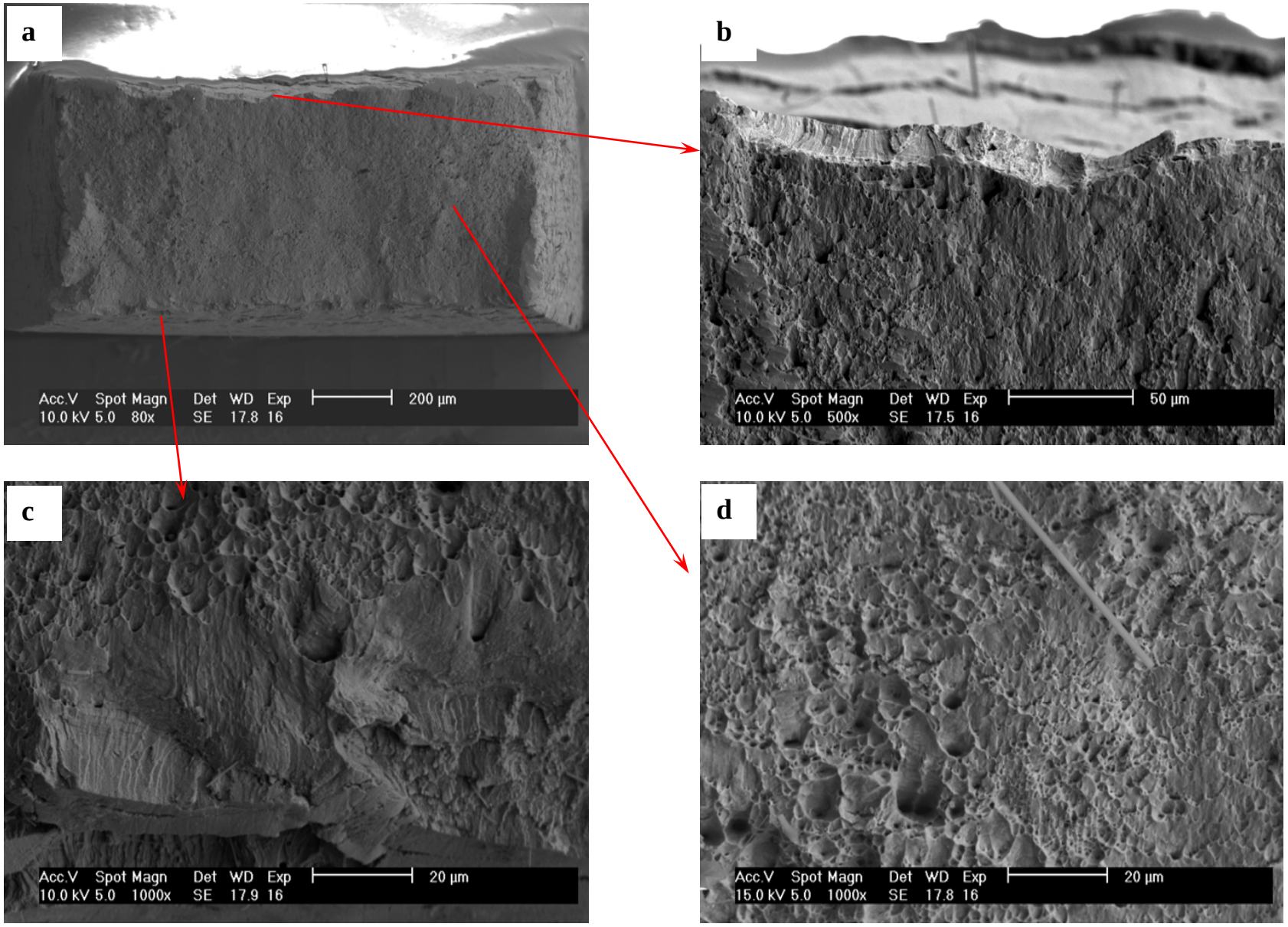

Figure 40. Fracture surface of SA 316 SS irradiated to 4.8 dpa and tested in PWR water (specimen B9-1).

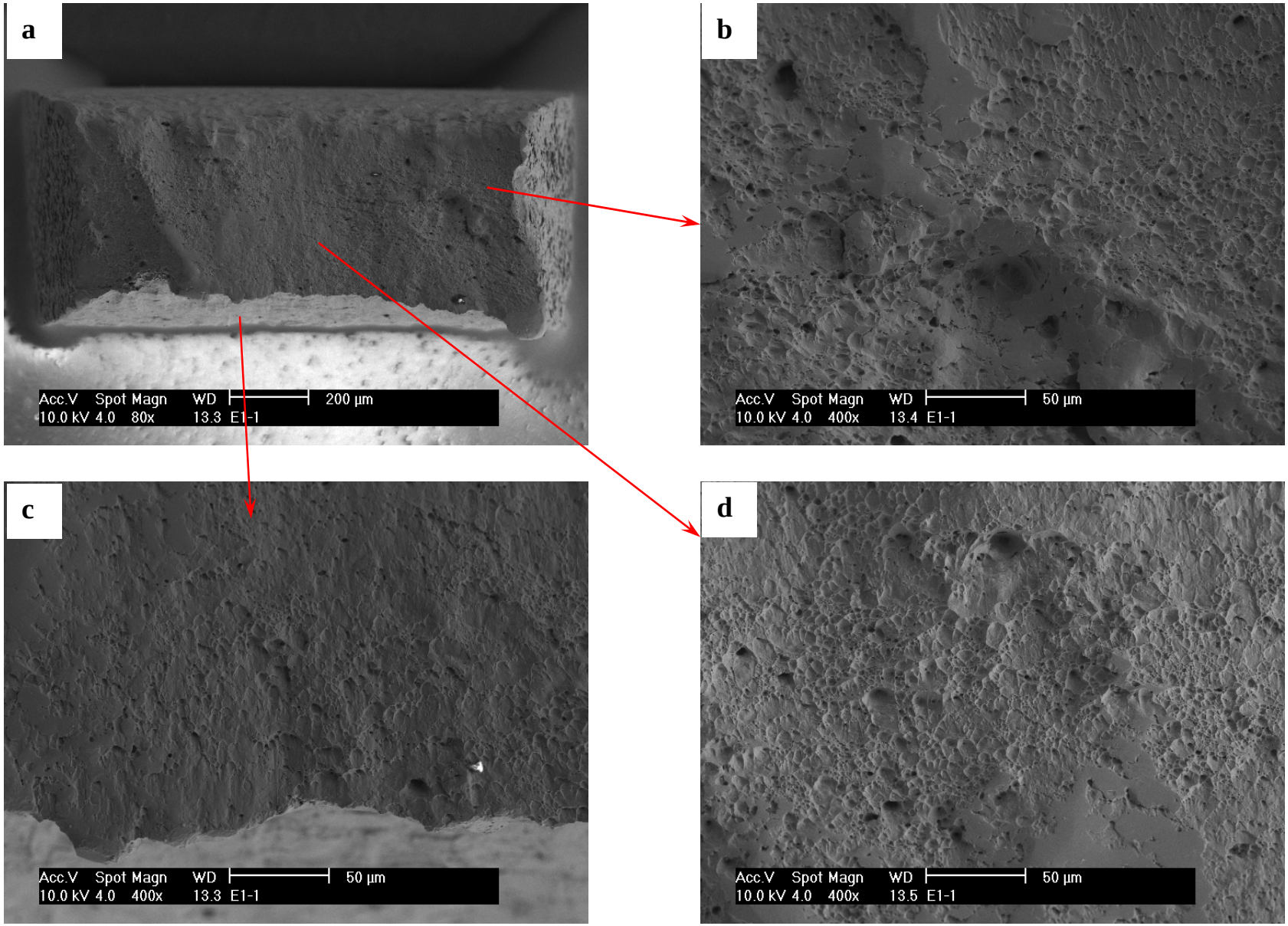

Figure 41. Fracture surface of GBE 690 irradiated to 5.5 dpa and tested in PWR water (specimen E1-1).

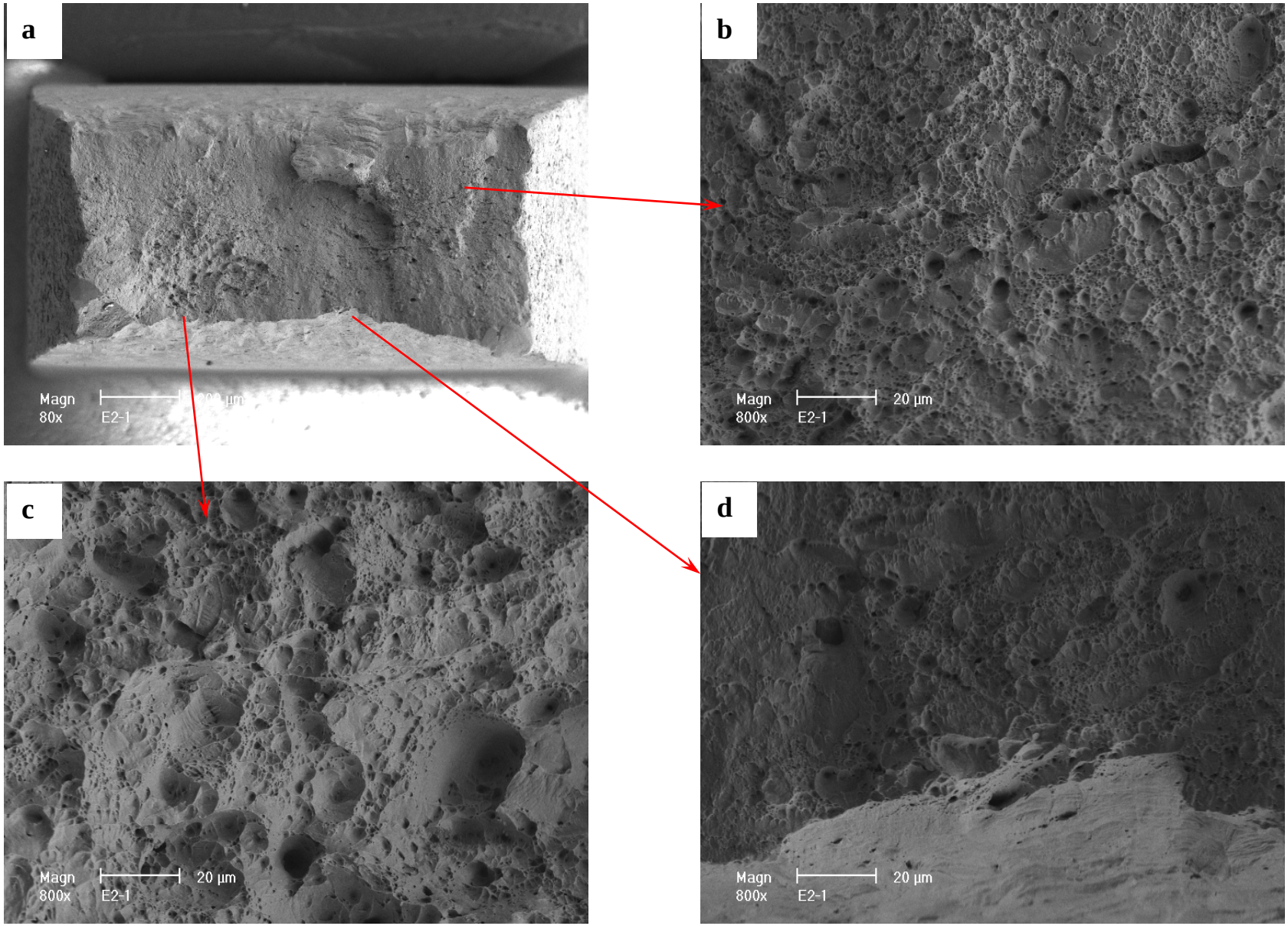

Figure 42. Fracture surface of SA A690 irradiated to 4.8 dpa and tested in PWR water (specimen E2-1).

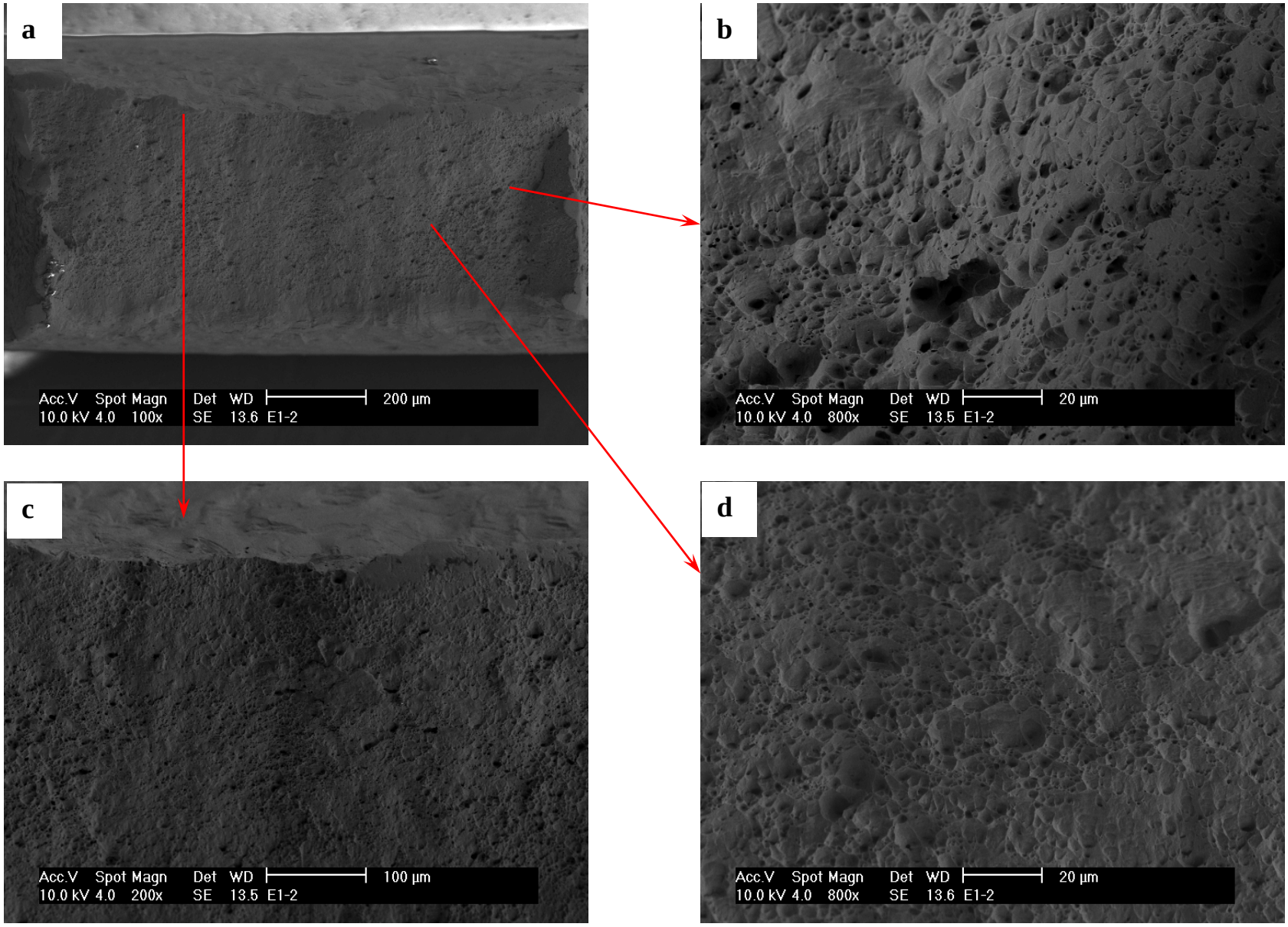

Figure 43. Fracture surface of GBE 690 irradiated to 9.6 dpa and tested in PWR water (specimen E1-2).

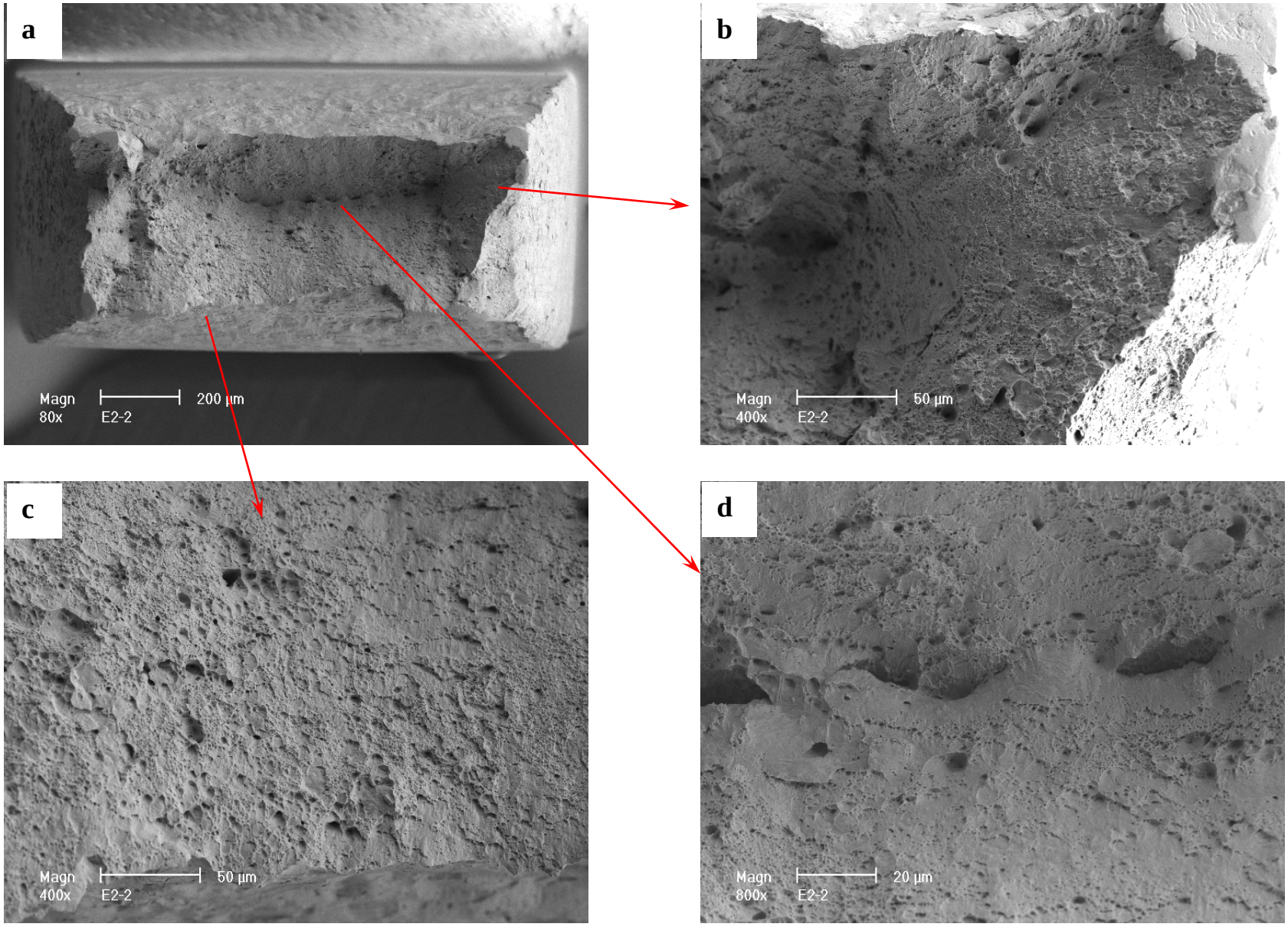

Figure 44. Fracture surface of SA A690 irradiated to 9.6 dpa and tested in PWR water (specimen E2-2).

This page is intentionally left blank.

4 Discussion

All SSRT tests performed on the BOR-60 specimens are summarized in Table 9. The tests carried out in BWR water have been reported previously in reference [27], and the tests carried out in an air atmosphere and in PWR water are included in the current report. Significant hardening is observed in all irradiated tests regardless their test environments. The saturation of irradiation hardening appears to be below ~10 dpa. Meanwhile, the TE continues to decline with increasing dose beyond 10 dpa. The work-hardening capability also decreases considerably in the irradiation specimens. Above ~10 dpa, work hardening is essentially absent among the tested materials. In general, cracking susceptibility is low in PWR water. The effect of prior cold-work on YS remains unchanged after irradiation up to 48 dpa. While IG cracking has been observed extensively in the BWR tests [26], brittle cracking areas are less frequently observed in PWR environments under similar test conditions. Ductile dimple fracture is the predominant morphology for all tests in PWR water. Intergranular cracking is seen in only a few samples (e.g., SA 316 SS at 47.5 dpa, and SA 347 SS at 45 dpa) and in localized regions. Transgranular cleavage cracking has been observed more often in CW and high-dose specimens. The overall fraction of brittle fracture is low (a few percent) among the SSRT tests in PWR water.

Table 9. All SSRT tests conducted on BOR-60 specimens.

Material Type [a]	Heat ID	Material Code	Test Environment [c]		
			5 dpa [b]	10 dpa [b]	40 dpa [b]
347 SA	316642	D1	PWR	PWR, Air	PWR
347 CW	316642CW	D2	-	PWR	-
ABB 304 SA	2333	B1	-	Air	-
ABB 304 CW	2333 CW	B2	-	Air	-
316LN SA	623	B3	PWR	PWR	-
316LN-Ti SA	625	B4	-	-	PWR
316 SA	C21	B5	-	Air	PWR
316 CW	C21 CW	B6	PWR, Air	PWR, Air	PWR
304 SA, low S	C1	A1	BWR	-	-
304 SA, high S	C9	A2	BWR	-	-
304 SA, low S	C12	A3	BWR	-	-
304 CW, low S	C1 CW	A4	BWR	-	-
304 CW, low S	C12 CW	A5	-	-	PWR
304 GBE	304 GBE	A6	PWR	-	-
316 GBE	316 GBE	B8	PWR	-	-
690 GBE	690 GBE	E1	PWR	PWR	-
304 BASE	304 BASE	A7	PWR	-	-
316 BASE	316 BASE	B9	PWR	-	-
690 BASE	690 BASE	E2	PWR	PWR	-
HP 304L SA, high O	945	A8	BWR	PWR	PWR
HP 304L SA, low O	1327	A9	BWR	PWR	PWR
304L SA	C3	A10	BWR	PWR	-
304L CW	C3 CW	A11	BWR	PWR	PWR
304-like alloy	L5	A12	BWR	PWR	PWR

[a] SA = solution-annealed; CW = cold-worked at room temperature; WW = warm-worked at 400°C; GBE = grain-boundary-engineered; BASE = base heat for GBE modification; HP = high-purity.

[b] Doses are target doses. The actual doses received are given in Table 2.

[c] Tests in the BWR environment are reported in Ref. [27].

4.1 Irradiation Hardening and Embrittlement

Irradiation hardening (an increase in YS) and embrittlement* (loss of ductility) have a significant impact on SSRT behavior. To assess the cracking susceptibility of austenitic SSs, dose dependences of irradiation hardening and embrittlement are needed for temperatures and doses relevant to LWRs. To reveal the effects of irradiation dose, all SSRT results in this study are plotted in Fig. 45, along with the previous BOR-60 and Halden results [26,27,42] obtained in a BWR environment of NWC at ~290°C. Significant increases in YSs can be seen in all irradiated tests, as shown in Fig. 45a. The YSs of irradiated specimens are about 200-600 MPa higher than that of nonirradiated SSs (the YSs of nonirradiated specimens are about ~200 MPa for SA SSs, and >500 MPa for CW SSs). The YSs increase rapidly with the damage dose up to ~5 dpa, and eventually saturate at 5-10 dpa. Between 10 and 48 dpa, the YSs are nearly unchanged.

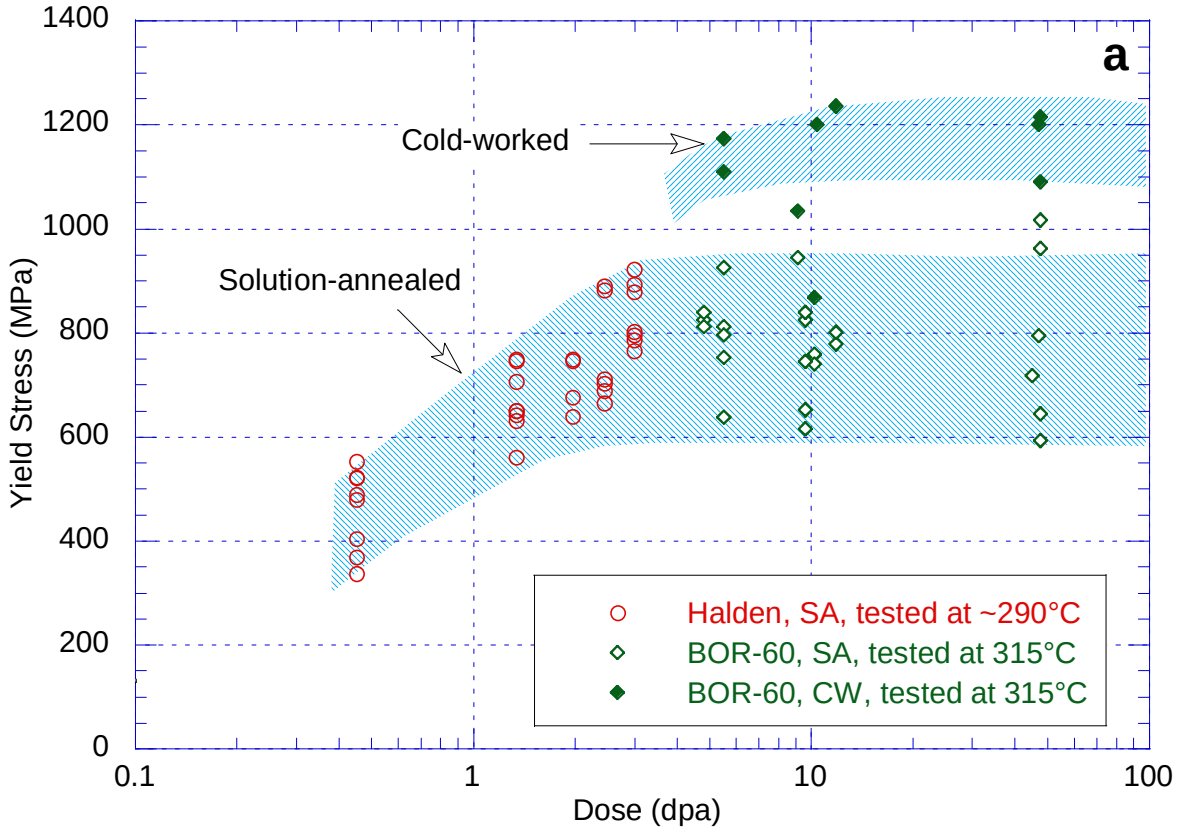

Figure 45. SSRT yield strength as a function of irradiation dose showing the effect of CW: (a) all materials tested on the BOR-60 and Halden specimens, and (b) a single material, Type 316 SS.

* The term of irradiation embrittlement is loosely used here to describe the loss of ductility resulting from radiation damage.

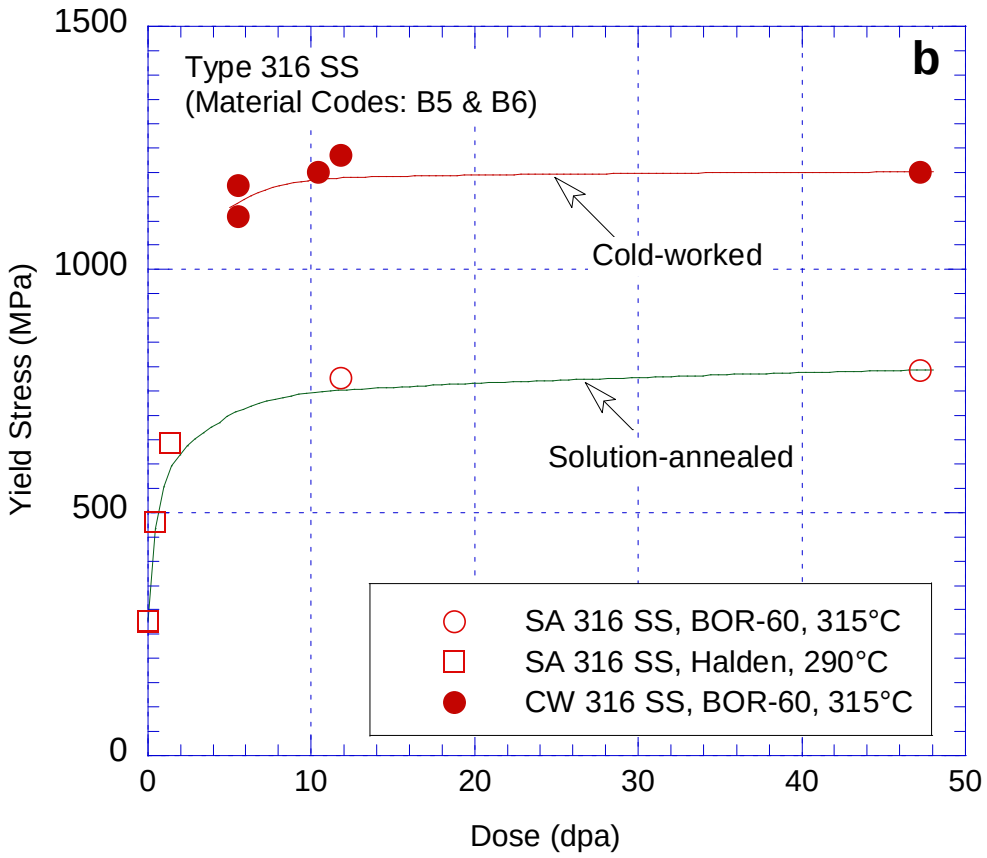

Figure 45. (Contd.)

4.1.1 Irradiation hardening and saturation

It is well accepted that irradiation hardening arises from the interaction between the elastic fields of dislocations and irradiation-induced defects, such as faulted dislocation loops, stacking fault tetrahedra, cavities and voids, or precipitates. These defects act as dispersed barriers of glide dislocations in the Orowan hardening model.[28] The increased line tension of bowing-out dislocation segments between pinning obstacles gives rise to the hardening. Based on the same principle, Seeger [29] proposed that an additional shear stress required to drive a dislocation to overcome irradiation-induced defects is given by

$$\Delta\sigma_y = \alpha M \mu b (Nd)^{1/2} \qquad (1),$$

where α is the hardening coefficient, M is the Taylor factor (3.06 for fcc), μ is shear modulus, b is Burgers vector, and N and d are the number density and diameter of irradiation defects, respectively. At low doses, the value of Nd is proportional to the neutron fluence. Thus, irradiation hardening should increase with the square root of neutron fluence or dpa. When the dose increases further, impingement or overlapping of displacement cascades can no longer be ignored, and a reduced efficiency in generating obstacles is expected. Assuming an exclusion zone around an existing irradiation defect where a new defect is prohibited, the saturation of irradiation hardening can be quantitatively described by [30]

$$\Delta\sigma_y = A[1-\exp(-B*dpa)]^{1/2} \qquad (2),$$

where *A* and *B* are constants. Data from many irradiated materials can be fit well with this correlation, implying the accuracy of the model. For SSs irradiated at ~300°C, Odette and Lucas [31] found that *A* is about 670 MPa and *B* is 1/2.

In a companion microstructural study of the current work,[32] irradiation defect structure of SSs was examined with transmission electron microscopes (TEMs) between ~5 and 45 dpa. The TEM samples were also irradiated at the BOR-60 reactor under conditions identical to those of the SSRT samples. It was found that faulted dislocation loops on {111} crystal graphic planes are the dominant irradiated defects. No voids or cavities were observed at the irradiation temperature up to ~45 dpa. Only a few fine precipitates may be present among these specimens at doses above ~25 dpa. On the basis of this microstructural information, it is reasonable to assume that faulted dislocation loops are the main source of irradiation hardening for the SSRT tests performed in this study. For the 5- and 10-dpa SA samples, the measured size and density of dislocation loops are about 8-9 nm and 3-6×10^{22} m^{-3}, respectively.[32] Assuming an α value of 0.45 for dislocation loops [33] and an nonirradiated YS of ~200 MPa for SA specimens, the estimated yield strengths strengthened by faulted dislocation loops are between 500 and 600 MPa. This value is reasonably close to the low bound of the SA data band at 5-10 dpa level (shown in Fig. 45a). The slightly higher strengths measured in SSRT tests may be attributed to pre-existing network dislocations in nonirradiated materials. A considerable amount of network dislocations and sometime even dislocation cell structures were observed in several archive nonirradiated SA samples, suggesting an inadequate annealing treatment prior to irradiation.[32]

The TEM study also shows that, while the mean size of dislocation loops does not change considerably above ~5 dpa, the density of dislocation loops increases from ~5 to ~10 dpa and becomes saturated above 10 dpa around 5×10^{22} m^{-3}. This dose dependence is consistent with the saturation of irradiated yield strength displayed in Fig. 45, confirming that faulted dislocation loops are the main hardening sources for irradiated SSs at PWR-relevant temperatures and doses.

Solution-anneal vs. cold-work

With the increase of irradiation dose, irradiation-induced dislocation loops continue to grow in size and eventually interact with neighboring loops or network dislocations. The interactions lead to un-faulting of the dislocation loops, which become glissile and contribute to the population of network dislocations in materials.[21] The initial dislocation microstructure may not be maintained during this process. A steady state of dislocation microstructure that is independent of the starting state may develop. For Type 316 SS, Garner[34] showed that the overall dislocation densities for SA and CW samples approach the same level above ~20 dpa. Several examples given in reference [35] also show that the YSs of SA and CW samples are similar beyond 10-20 dpa. This dislocation recovery mechanism relies on the growth rate of dislocation loops, which peaks around 500°C for an LWR dose rate, and decreases sharply at both high- and low-temperature regimes.

In our SSRT tests, the SA and CW data fall into two scatter bands with a few exceptions (see Fig. 45a). In general, the irradiated YSs obtained in these tests are higher for the CW than for SA materials. Becsause a wide range of austenitic SSs with different initial microstructures is included in these results, heat-to-heat variation may contribute to the large scatter of the results. Thus, the difference in YSs between SA and CW materials is better illustrated with a single alloy, as shown in Fig. 45b. The YSs of CW 316 SS are much higher than that of CW 316 SS at all doses. The fact that that SA and CW curves remain separate up to 48 dpa indicates that dislocation mobility was too low at this irradiation temperature, and thus dislocation recovery was restricted during irradiation. The initial microstructure is still an important factor affecting irradiation hardening at PWR temperatures at 48 dpa. This observation is also consistent with the TEM study, where no network dislocations were seen in a significant amount in the BOR-60 irradiation.[32] Faulted dislocation loops are still the dominant defects in these specimens up to ~ 45 dpa.

4.1.2 Irradiation embrittlement

Thanks to its high close-pack density, austenitic stainless steel has good ductility and can be plastically deformed to a large extent before fracturing. This capability of carrying plastic flow is greatly reduced after neutron irradiation. A much lower fracture toughness is detected for irradiated SSs as a consequence.[36] While various irradiation effects can lead to the loss of ductility, the underlying mechanisms of irradiation embrittlement are not fully understood at present. Because no significant changes in local fracture mode are observed after irradiation, irradiation embrittlement is largely considered a consequence of the different stress-strain behavior of irradiated materials.[37] As shown in Fig. 5, significant strain hardening can be observed in nonirradiated SSs. The stress-strain behavior of SSs can be described by a power law:

$$\sigma_t = k\varepsilon_t^{\,n} \qquad (3),$$

where k is a material constant; σ_t and ε_t are the true stress and true strain, respectively; and n is the strain-hardening exponent. The flow stress increases from the YS to UTS, and the sample is deformed uniformly before the onset of tensile instability (i.e., necking). The true strain at the end of the uniform elongation is numerically equal to the strain-hardening exponent n. In irradiated SSs, however, the increase in YS is much greater than the increase in UTS (e.g. Fig. 5). As a result, the strain-hardening rate decreases significantly. If the YS becomes the same as the UTS, there will be no uniform elongation, and strain-softening occurs immediately. The SSRT results in Section 3 show that strain hardening is very limited in the tests at ~5 dpa, and is completely absent in most of the tests above ~10 dpa. Because of this change in the stress-strain behavior of irradiated SSs, the onset of plastic instability appears at a much lower strain level, and thus the TE is much shorter than found in their nonirradiated counterparts.

While the loss of capability to be work-hardened is the reason of declining elongation, the exact micro-mechanism that is operating in irradiated SSs and leading to this behavior is not entirely clear. Coarse deformation bands have been observed in irradiated SSs.[38] Transmission electron microscopy also shows that a deformed irradiated microstructure is often inhomogeneous and contains well-defined defect-free channels.[39,40] It is believed that the formation of dislocation channels contributes to localized deformation. When an irradiated material is under plastic deformation, leading dislocations interact and "swap away" irradiation defects, leaving behind defect-free channels. Consequently, a much lower stress is needed for additional dislocations to propagate along these channels. A significant amount of plastic flow can take place within these channels, while little dislocation activity occurs outside. This microscopically inhomogeneous slip behavior leads to a higher local strain rate and a stronger triaxial state of stress at the intersections of dislocation channels and grain boundaries or free surfaces.[41] Both conditions are favorable for prompting cracking or brittle fracture. For this reason, irradiation materials appear to be more brittle and macroscopic ductility is greatly reduced.

Figure 46a shows the TEs as a function of dose for all BOR-60 and Halden specimens tested between 290 and 320°C. A decreasing trend of TE can be seen with increasing dose (shaded area). While irradiation hardening has been saturated above ~10 dpa (see Fig. 45), the TE continues to decrease up to 48 dpa. This observation implies that irradiation embrittlement continues to evolve beyond the saturation of irradiation hardening. It should be noted that the reported elongations are not directly comparable between the Halden and BOR-60 specimens because of their different gauge dimensions. The ratio of cross-section area to gauge length is about 20% greater for the BOR-60 specimens, and thus higher elongations are expected for the BOR-60 specimens under the same test condition. This geometrical difference contributes to the "mismatch" between the Halden and BOR-60 data sets around 3-5 dpa (red line vs. green line in Fig. 46a). Nonetheless, the general declining trend is evident for both data sets in Fig. 46a. The TEs are also different for the CW and SA materials. As shown in Fig. 46b, the SA 316 SS has significantly higher TE than that of CW 316 SS.

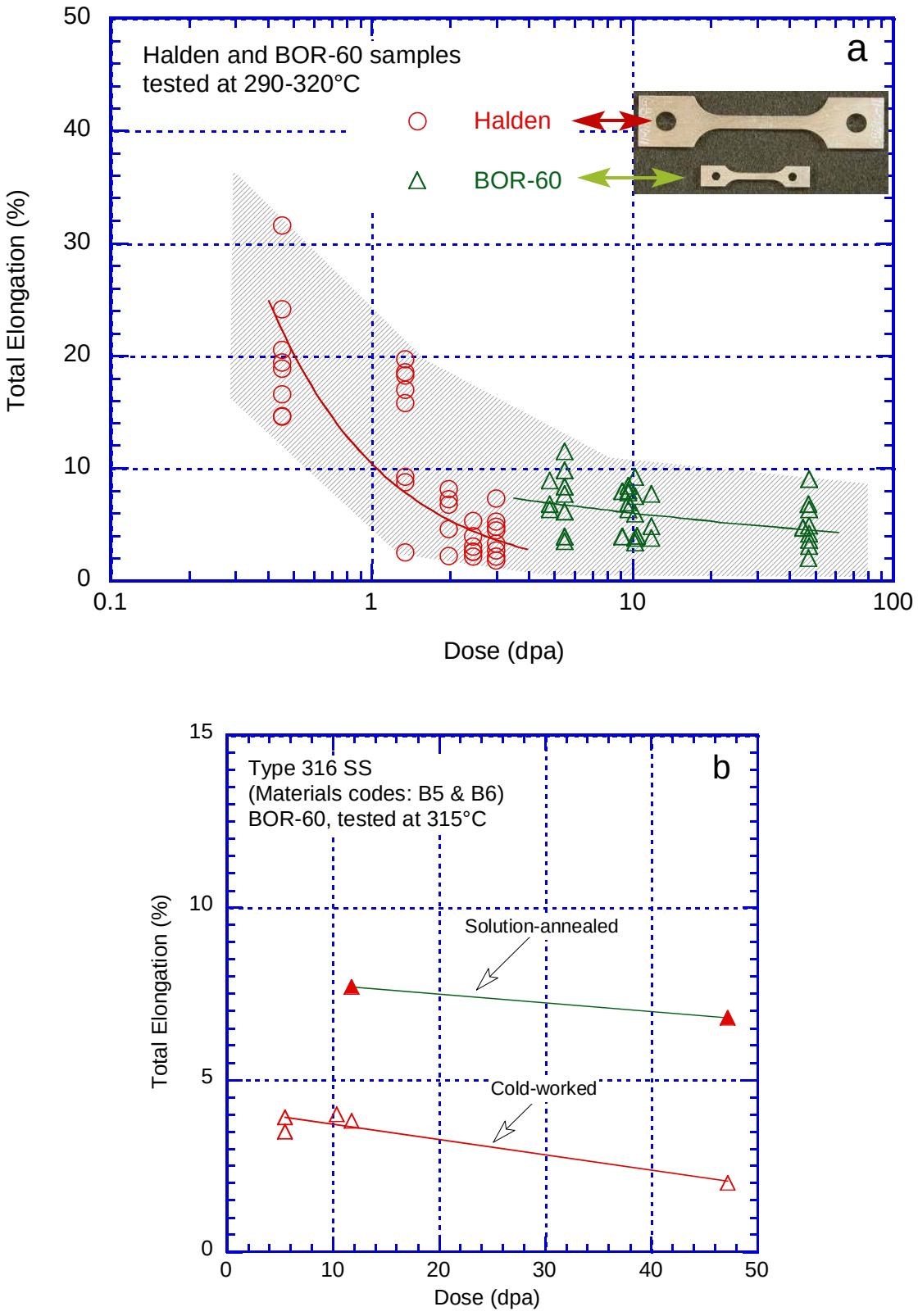

Figure 46. Total elongations as a function of irradiation dose for BOR-60 and Halden specimens.

The effect of CW on flow localization is not very clear.[33] While strain softening can be seen in both SA and CW tests, a very limited amount of strain hardening remains in several CW tests. Well-defined yield points are more often seen in SA tests than in CW tests (e.g., Fig. 5). The CW SSs seem less prone to flow localization than the SA SSs. It is possible that pre-existing dislocation networks in the CW samples play an important role in the development of deformation channels. When complex dislocation networks are present, such as in CW SSs, mobile dislocations interact with network dislocations to increase flow stress. The resulting hardening effect may suppress the strain-softening or flow localization to some extent. This effect may be the reason for the slightly different stress-strain behavior observed in SA and CW tests.

In addition to elongation, reduction in area (RA) is also reported in Tables 4-8 as a measure of ductility. Depending on the materials, the measured RAs vary from 20 to 80%. The large data scatter is attributed to different initial microstructures and heat-to-heat variations. Because little uniform elongations are present in these irradiated tests, the high values of RA imply significant deformation after the onset of plastic instability. Figure 47 shows the RAs for Types 304, 316, and 347 SSs. The CW samples have RAs of 20-30%, whereas all SA samples show RAs of higher than 40%. For a given material, irradiation dose seems to have little effect on the RAs. Similar values of RA are observed at all doses. The fact that RAs are insensitive to irradiation dose suggests that fracture mode does not change significantly between 5 and 48 dpa.

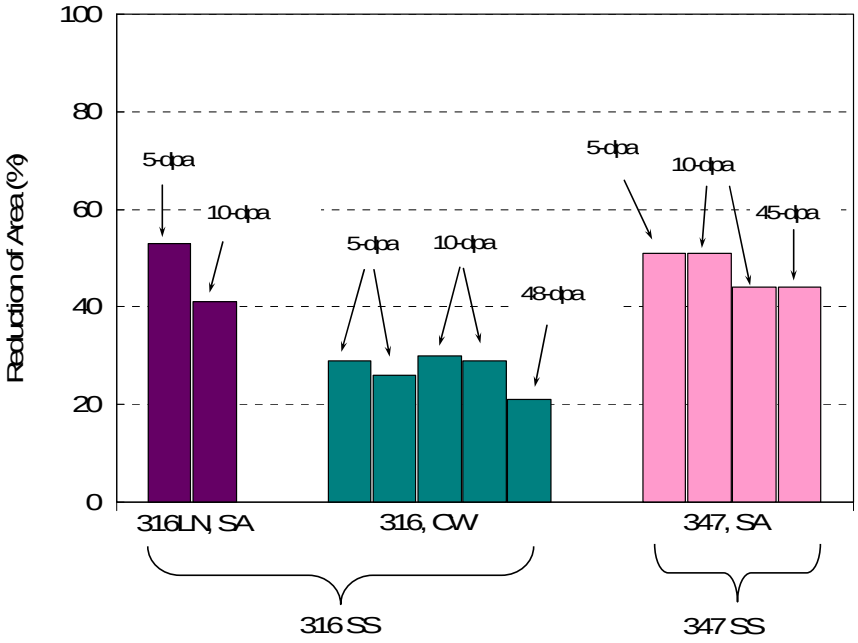

Figure 47. Similar reduction of area results at different doses for selected alloys.

4.2 Cracking Susceptibility in the PWR Environment

4.2.1 Fracture morphology

As shown in Section 3, ductile dimple fracture is the dominant morphology for most of the SSRT tests performed in the PWR environment. Small areas of TG and cleavage cracking can be seen in many CW and high-dose samples. Intergranular cracking is only observed in the 47.5-dpa SA 316 SS and 45-dpa 347 SS. The overall fraction of brittle fracture is low in the specimens examined. In general, cracking susceptibility is low for

the specimens tested in PWR water. The low cracking susceptibility in the current SSRT tests seems to be consistent with field observations that cracking is reported for internals at much higher doses in PWRs than in BWRs. While IG cracking has been observed extensively in the previous SSRT tests in BWR water,[26,43] brittle fracture areas are less frequently seen in PWR environments under similar test conditions. An example of this difference is given in Fig. 48. It has been shown that HP 304L SS with high-O is highly susceptible to cracking at ~5 dpa in BWR water with NWC. The same heat irradiated to a higher dose (~10 dpa) and tested in the PWR environment, however, shows a ductile dimple fracture. Although one-to-one comparisons between identical materials are not always available, the drastically different fracture morphologies are also observed for other materials tested in BWR and PWR environments. In general, cracking susceptibility of the tested materials is much lower in PWR than in BWR environments.

The lower cracking susceptibility in PWR primary water can be inferred from the effect of corrosion potential. Assuming slip/dissolution as the operating mechanism, the oxide film ruptures periodically to expose the fresh metal surface, and the crack advances by anodic dissolution at the crack tip.[6,14] It has been shown that the crack tip dissolution rate can vary considerably with corrosion potential in oxygenated water. By lowering the corrosion potential of a material/environment system, the oxidization rate is reduced significantly. Crack growth rate (CGR), which is controlled by the dissolution rate, is thus a strong function of corrosion potential.[6,14] Under a constant-load condition, CGRs were found to be more than one order of magnitude lower in low-potential environments than in high-potential environments.[44,45] The predicted CGR response to corrosion potential seems to be consistent with the low cracking susceptibility observed in the current SSRT tests in the PWR environment.

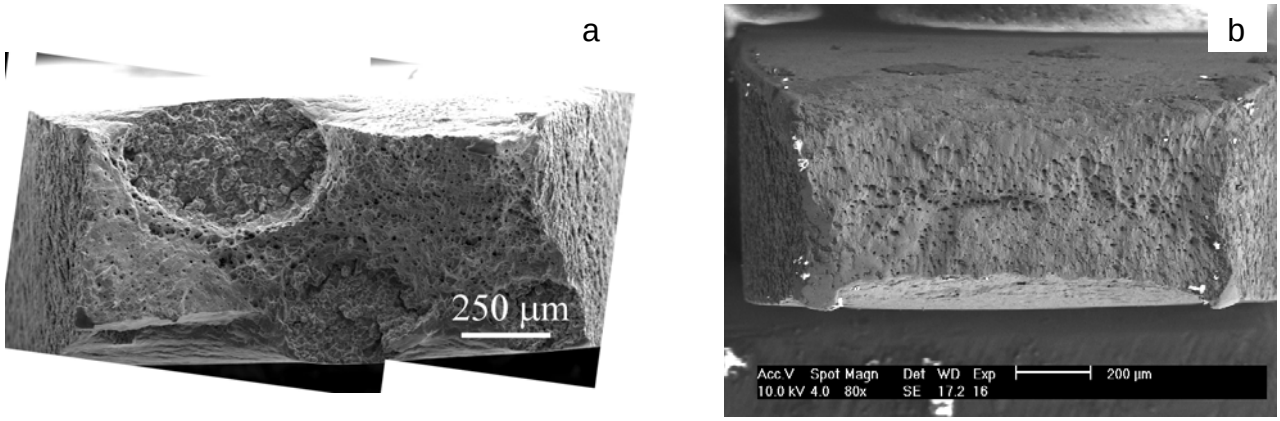

Figure 48. Fracture surfaces of HP 304L SS with high-O, (a) 5-dpa, tested in BWR NWC, and (b) 10-dpa, tested in PWR water.

Despite the low cracking susceptibility, brittle cracking does occur in the SSRT tests in a PWR environment. Mixed-mode TG and cleavage cracking are the most common brittle features identified on the fracture surfaces. While mixed-mode TG cracking is also observed in BWR water tests,[26,43] cleavage fracture is only observed among PWR water tests. Because cleavage cracking represents a form of low-energy fracture that is not normally associated with ductile materials such as austenitic SSs, the observation of cleavage indicates severe embrittlement among these samples.

Cleavage cracking seems to develop readily among all materials tested in this study except Alloy 690. A few examples of cleavage cracking with typical river patterns can be seen in Figs. 13d and 16d-g for 316 SS, Figs. 25c and 37b-d for 304 SSs, and Figs. 32b-d and 34b for 347 SSs. Cold-worked or higher-dose specimens seem more prone to cleavage fracture in PWR water tests. Because many of the cleavage areas are located at the

sample/water interfaces, an environmental contribution to the cracking is speculated. Meanwhile, irradiation effects cannot be ignored. Irradiation hardening and flow localization must also play a crucial role in cleavage cracking. A high local strain rate and triaxial state of stress resulting from deformation channels are all favorable conditions for cleavage cracking. It is possible that both irradiation hardening/embrittlement and environmental effects are needed for cleavage cracking in PWR water tests.

Among all specimens tested in PWR water, IG cracking is identified in only two cases: one is in a Type 316 SS and another is in a Type 347 SS. Both specimens are in solution-annealed condition and irradiated to high doses (47.5 dpa for the 316 specimen, and 45 dpa for the 347 specimen). IG cracking (indicated by the white arrow in Fig. 16e) is very limited in the 316 sample. It appears that the IG crack started from the sample surface but quickly changed to a cleavage fracture as it advanced deeper into the sample. For the 347 specimen, the IG morphology is located in a large area mixed with void coalescence (Fig. 35c) and cleavage cracking (indicated by the white arrow in Fig. 35d). The grain size of this sample is also fairly large as can be seen in the figure. The overall coverage of IG cracking is much higher in 347 SS than in 316 SS.

For both 316 and 347 SSs, IG cracking is observed in high-dose SA specimens but not in CW samples (see Fig. 15 vs. Fig. 16 for 316 SS, and Fig. 34 vs. Fig. 35 for 347 SS). This difference between the SA and CW samples may suggest that flow localization resulting from dislocation channeling plays a key role in IG cracking. As we discussed in Section 4.1.2, CW microstructure may restrain flow localization to some extent in irradiated materials. Thus, if flow localization is a crucial factor for IG cracking, the SA specimens should be more susceptible to IG cracking than the CW samples. It is well understood that localized slip in dislocation channels generates stress concentrations at barriers such as grain boundaries.[41] A pileup of dislocations within channels can produce high local stress to fracture grain boundaries, especially for materials with large grain size. It has been speculated that such a stress concentration can also be related to IG cracking.[21] While the exact mechanism remains unclear, Jiao and Was[46] have shown recently that channel heights can be correlated well with cracking susceptibility. This result is a strong indication that flow localization is important for elevating cracking susceptibility in irradiated materials. The difference between the SA and CW samples shown in our SSRT tests seems to support this argument.

4.2.2 Time to failure

Because brittle fracture areas are limited and scattered on fracture surfaces for the specimens tested in PWR water, it is difficult to use the fraction of brittle areas as a measure to evaluate cracking susceptibility. For this reason, we use the time duration of SSRT test as a quantity to characterize the relative cracking susceptibility among these samples. Time to failure (TF) of each SSRT test is reported in Tables 4-8. To eliminate the influence of an initial idle period in a test, the starting time is defined as when the load reaches 10 lbs (~38 MPa for the BOR-60 specimens). The end of test is simply defined as the final fracture of the sample.

Figure 49 shows all SSRT tests in the PWR environment at three doses. Similar materials are grouped together to form four types of SSs (304 SS, 316 SS, 347 SS, and Alloy 690). Different thermo-mechanical treatments or different compositions within the same type of material are not distinguished. These four types of SSs are represented by different colors, as shown in Fig. 49. The values of TF vary considerably from one test to another. It is of note that the extremely low TF of HP 304L SS with high-O should be disregarded because the sample's thickness was nearly 50% lower than that of other samples. In general, at a given dose, the TFs of Alloy 690 are higher than that of 304 and 316 SSs with a few exceptions (the GBE 316 SS at 5 dpa, and the 304-like model alloy at 48 dpa). The TFs of 347 SS are among the lowest at each dose level. Despite a large variation

among different materials, a general trend of declining TFs with increasing dose can be seen. This dose-dependent behavior is more evident for Type 316 SS (green) and Type 347 SS (brick) in Fig. 49.

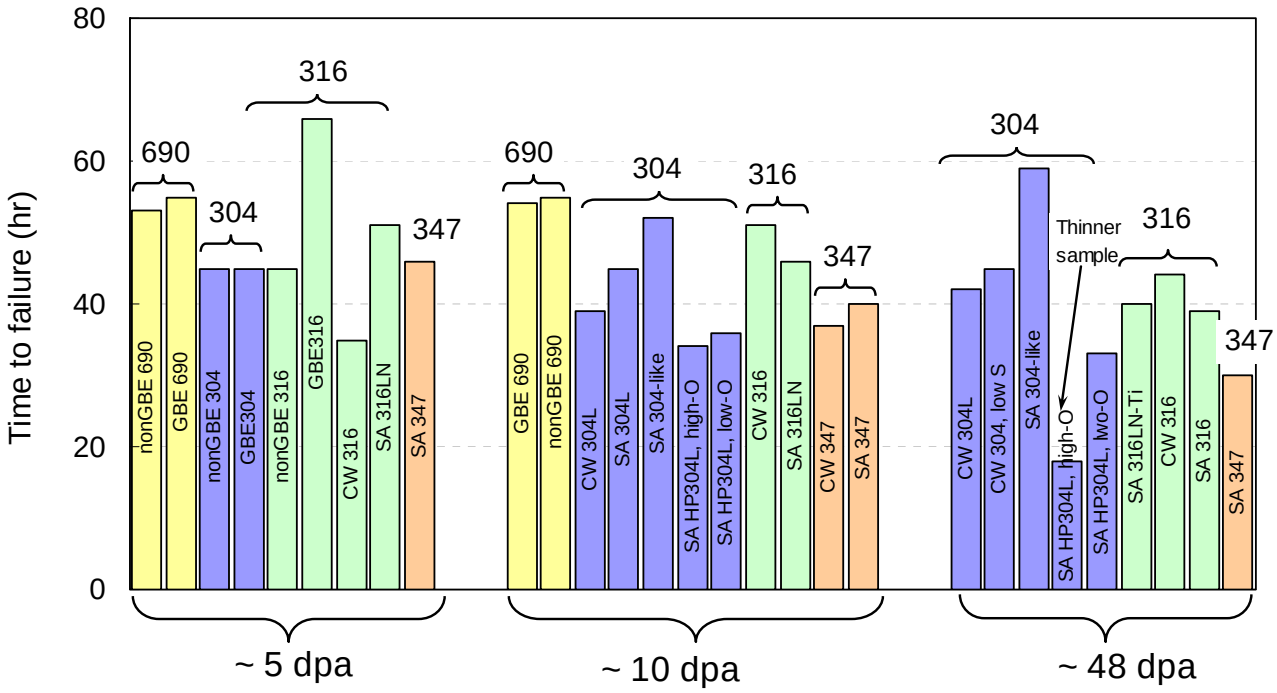

Figure 49. Time to failure of tests in PWR water at three doses.

The effect of CW on TF is shown in Fig. 50. All materials, except GBE/non-GBE pairs, are plotted in two groups, and the color coding for different material types remains the same. For each type of materials, the TFs of SA specimens are always higher than those of the CW samples, except the four HP 304L specimens with different oxygen contents. These specimens were specially designed to investigate the effect of oxygen content. Therefore, the thermal-mechanical treatment employed may be different from a typical SA treatment applied to other samples. This speculation is verified by their noticeably different SSRT behaviors as discussed in Section 3.3. Another low TF value on the SA side of the plot is the 45-dpa 347 SS. The sample contains a large area of IG and mixed-mode cracking (see Fig. 35). Thus, both fractographic and TF results indicates that SA 347 SS can become highly susceptible to cracking in a PWR environment above 45 dpa.

In addition to SA and CW, another thermal-mechanical treatment examined in this study is GBE. The TF values of the GBE specimens and their non-GBE counterparts are plotted in Fig. 51. It is evident that GBE has no effect on Alloy 690 and 304 SS. The TF of GBE 316 SS is longer than that of non-GBE 316 SS. There seems to be a beneficial effect of GBE treatment on 316 SS. However, a previous study on GBE materials showed a conflicting result. Whereas a beneficial effect was observed on fracture toughness, the CGRs of GBE 316 SS and GBE304 SS were actually higher than those of their non-GBE counterparts.[47] It is believed that an inadequately executed GBE treatment can elevate cracking susceptibility by introducing brittle precipitates and enlarging grain size. Because there is no clear evidence from fractographic examination showing different fracture morphologies between the GBE and non-GBE 316 SS in the current study, the effect of GBE treatment remains unclear.

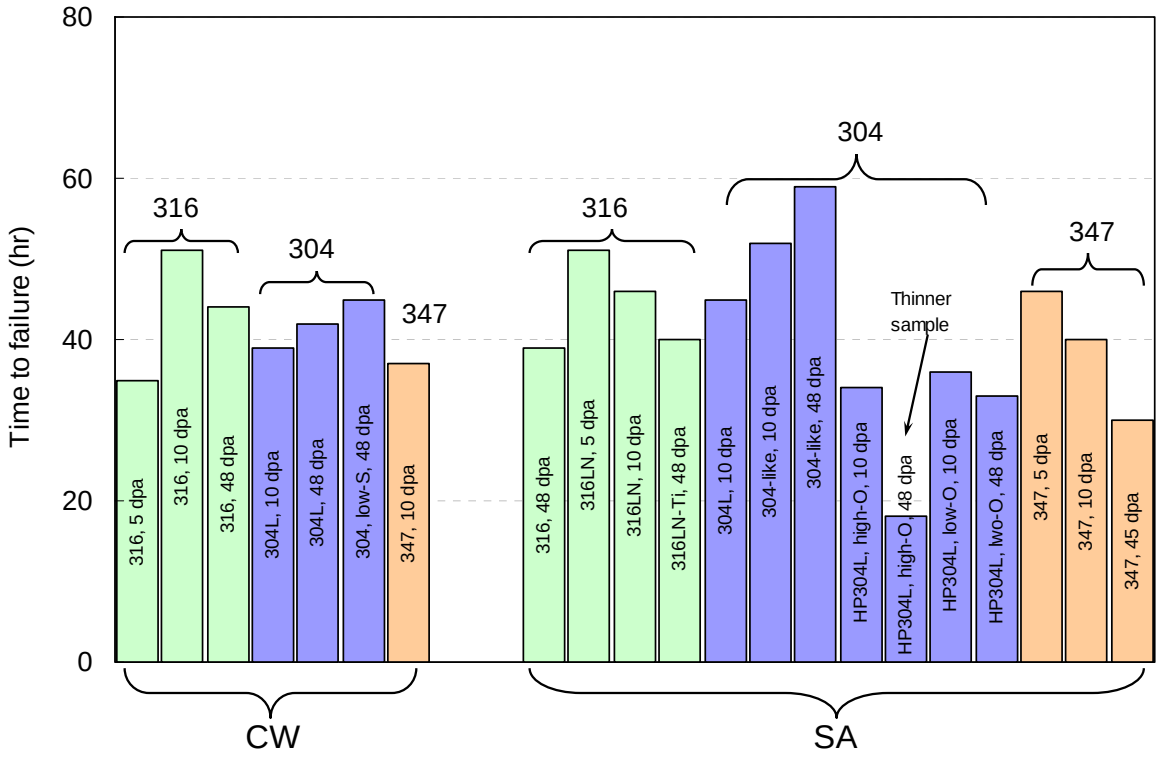

Figure 50. Comparison of time to failure between CW and SA samples (dpa values are approximate doses).

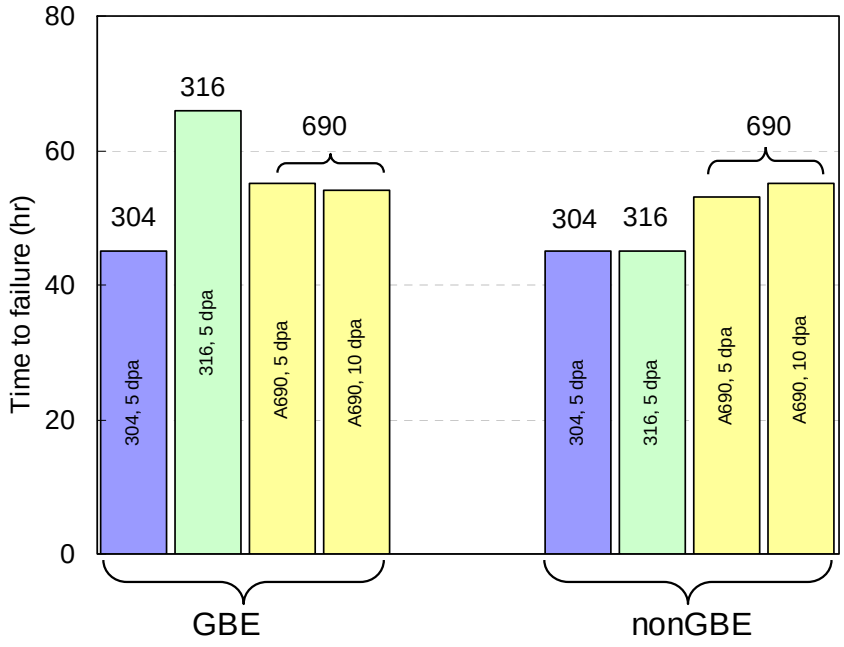

Figure 51. Comparison of time to failure for GBE alloys (dpa values are approximate doses).

4.3 Deformation Rate and Irradiation Spectrum

Stress corrosion cracking is sensitive to crack tip strain rate and oxidization rate. With a given material/environment system, SCC can be revealed at a certain range of applied strain rates.[48,49] If a test was performed at too high a strain rate, there is not enough time for SCC to develop. On the other hand, if the strain rate is too low, the film-rupture rate would be too slow and an active condition at the crack tip cannot be maintained. The applied strain rate in this study ($\sim 7.4\times10^{-7}$ s^{-1}) was used in a previous IASCC study in a BWR environment. For comparison, the same strain rate was used for the PWR-water tests. With an environment of lower corrosion potential such as PWR primary water, it is possible that this applied strain rate is close to or above the upper limit of strain rate for SCC in these materials. The lack of brittle cracking in most of the PWR water tests seems to suggest that a much lower strain rate would be needed to induce SCC in a PWR environment. Intergranular cracking was reported in irradiated SSRT tests conducted at a strain rate of 6.7×10^{-8} s^{-1} in PWR water.[50] Because IG cracking was also observed in the same study in argon atmosphere, the exact role of the PWR environment in prompting IG cracking is uncertain. Nonetheless, it shows that under certain conditions, extensive IG cracking can be developed in highly irradiated SSs.

Because cracking susceptibility is low in a low-potential environment, it is reasonable to assume that irradiation effects have a more important role for IASCC in PWR water. Due to this crucial role of irradiation, it is important to recognize the differences in the microstructural evolution of different irradiation experiments. In this study, the specimens were irradiated in a fast breeder reactor whose neutron spectrum is harder than that of PWRs. This difference in neutron spectra may lead to some subtle differences in the development of damage and RIS in irradiated SSs. Whether or not these differences will affect SSRT behavior in a PWR environment is not clear at present. Nonetheless, we should note that irradiation conditions employed in the current study are not identical to that experienced by LWR core internals. The displacement damage rate of a typical fast reactor irradiation is about one order of magnitude higher than that of PWRs. At the same irradiation temperature, a lower defect survival rate and a stronger RIS effect would be anticipated for a higher damage rate.[51,52] In the meantime, because of the different fast-to-thermal neutron ratios, transmutation helium and hydrogen production rates in a fast reactor irradiation could also be different from that found in PWR irradiation. Consequently, defect microstructure and RIS may be affected as well. Some limited data have shown that grain-boundary segregations are somewhat sensitive to neutron spectra.[53] Additional work that evaluates the effect of neutron spectra would be valuable to validate the SSRT results in the current study.

This page is intentionally left blank.

5 Summary

A total of 29 SSRT tests were performed on 15 materials in a simulated PWR environment at three dose levels (5, 10, 48 dpa). Several tests were also conducted in the air atmosphere for reference. The samples are miniature tensile specimens of various SSs commonly used in reactor internal components. Solution-annealed, cold-worked, and GBE treated materials are included in the study. The SSRT tests were conducted at 315-320°C with a constant strain rate of 7.4×10^{-7} s^{-1}. After each test, the fracture surface of the tested sample was examined with a shielded SEM. Using fracture morphology and time to failure, cracking susceptibility was assessed at three doses for different materials and thermal-mechanical treatments.

All irradiated SSRT tests show significant hardening at all doses. The saturation of irradiation hardening appears to be below ~10 dpa. Meanwhile, the total elongation continues to decline slowly beyond 10 dpa. The effects of prior cold-work on strength and ductility remain unchanged after irradiation up to 48 dpa. In addition to irradiation-induced hardening, work hardening capability also decreases considerably in the irradiation specimens. Above 10 dpa, work hardening is essentially absent among all tested materials. Flow localization resulting from dislocation channeling is believed to be responsible for the loss of ductility.

Ductile dimple fracture is the dominant morphology for all SSRT tests in PWR water. Small areas of TG cleavage cracking can be seen in most CW and high-dose samples. Intergranular cracking is observed in high-dose SA Types 316 and 347 SSs. The overall fraction of brittle fracture is low for all SSRT tests, suggesting a low cracking susceptibility of SSs in the PWR environment. Nonetheless, a general trend of increasing susceptibility to cracking is found with increasing dose and cold-work condition.

This page is intentionally left blank.

References

1. U.S. NRC, "Generic Aging Lessons Learned (GALL) Report – Final Report," NUREG-1801, Rev. 2, 2010.
2. Cheng, C. F., "Intergranular Stress-Assisted Corrosion Cracking of Austenitic Alloys in Water-Cooled Nuclear Reactors," J. Nucl. Mater., **56** (1975): 11–33.
3. Garzarolli, F., H. Rubel, and E. Steinberg, "Behavior of Water Reactor Core Materials with Respect to Corrosion Attack," Proc. Intl. Symp. on Environmental Degradation of Materials in Nuclear Power Systems – Water Reactors, NACE, Houston, TX, pp. 1–24, 1984.
4. Garzarolli, F., D. Alter, and P. Dewes, "Deformability of Austenitic Stainless Steels and Nickel-Base Alloys in the Core of a Boiling and a Pressurized Water Reactor," Proc. Intl. Symp. on Environmental Degradation of Materials in Nuclear Power Systems – Water Reactors, American Nuclear Society, La Grange Park, IL, pp. 131–138, 1986.
5. Berge, Ph., and F. de Keroulas, "The Present Situation Regarding Environmental Degradation of Components in Pressurized Water Reactors," Proc. 4th Int. Symp. on Environmental Degradation of Materials in Nuclear Power Systems - Water Reactors, NACE, Houston, TX, pp. 1-11, 1990.
6. Andresen, P. L., F. P. Ford, S. M. Murphy, and J. M. Perks, "State of Knowledge of Radiation Effects on Environmental Cracking in Light Water Reactor Core Materials," Proc. 4th Intl. Symp. on Environmental Degradation of Materials in Nuclear Power Systems - Water Reactors, NACE, Houston, TX, pp. 1.83-1.121, 1990.
7. Nelson, J., and P. Andresen, "Review of Current Research and Understanding of Irradiation-Assisted Stress Corrosion Cracking," Proc. 5th Int. Symp. Environmental Degradation of Nuclear Power Systems, ANS-NACE-AIME, 1992.
8. Scott, P., "A Review of Irradiation Assisted Stress Corrosion Cracking," J. Nucl. Mater., **211 (**1994): 101-122,
9. Bruemmer, S. M., and G. S. Was, "Microstructural and Microchemical Mechanisms Controlling Intergranular Stress Corrosion Cracking in Light-Water-Reactor Systems," J. Nucl. Mater., **216 (**1994): 348-363.
10. Was, G. S., and P. L. Andresen, "Stress Corrosion Cracking Behavior of Alloys in Aggressive Nuclear Reactor Core Environments," Corrosion, 63 (1), (2007): 19.
11. Jacobs, A. J., G. P. Wozadlo, K. Nakata, T. Yoshida, and I. Masaoka, "Radiation Effects on the Stress Corrosion and Other Selected Properties of Type-304 and Type-316 Stainless Steels," Proc. 3rd Intl. Symp. Environmental Degradation of Materials in Nuclear Power Systems--Water Reactors, G. J. Theus and J. R. Weeks, eds., The Metallurgical Society, Warrendale, PA, pp. 673-680, 1988.
12. Garzarolli, F., D. Alter, P. Dewes, and J. L. Nelson, "Deformability of Austenitic Stainless Steels and Ni-Base Alloys," Proc. 3rd Intl. Symp. on Environmental Degradation of Materials in Nuclear Power Systems--Water Reactors, G. J Theus and J. R. Weeks, eds., The Metallurgical Society, Warrendale, PA, pp. 657-664, 1988.
13. Chung, H. M., R. V. Strain, and R. W. Clark, "Slow-Strain-Rate-Tensile Test of Model Austenitic Stainless Steels Irradiated in the Halden Reactor," Environmentally Assisted Cracking in Light Water Reactors Semiannual Report July 2000-December 2000, NUREG/CR-4667, Vol. 31, ANL-01/09, pp. 22-32, 2002.
14. Ford, F. P., and P. L. Andresen, "Development and Use of a Predictive Model of Crack Propagation in 304/316L, A533B/A508 and Inconel 600/182 Alloys in 288°C Water," Proc. 4th Intl. Symp. on Environmental Degradation of Materials in Nuclear Power Systems - Water Reactors, The Metallurgical Society, 1988.

15. Ford, F. P., "Quantitative Prediction of Environmentally Assisted Cracking," Corrosion, Vol. 52, No. 5, 1996.

16. Jacobs, A. J., R. E. Clausing, M. K. Miller, and C. Shepherd, "Influence of Grain Boundary Composition on the IASCC Susceptibility of Type 348 Stainless Steel," Proc. 4th Intl. Conf. on Environmental Degradation of Materials in Nuclear Power Systems - Water Reactors, NACE, 1990.

17. Chung, H. M., and W. J. Shack, "Irradiation-Assisted Stress Corrosion Cracking Behavior of Austenitic Stainless Steels Applicable to LWR Core Internals," NUREG/CR-6892, ANL-04/10, Jan. 2006.

18. Andresen, P. L, and M.M. Morra, "Effects of Si on SCC of Irradiated and Unirradiated Stainless Steels and Nickel Alloys," Proc. 12th Intl. Conf. on Environmental Degradation of Materials in Nuclear Power System – Water Reactors, Minerals, Metals, & Materials Society, 2005.

19. Busby, J. T., G. S. Was, and E. A. Kenik, "Isolating the Effect of Radiation-Induced Segregation in Irradiation-Assisted Stress Corrosion Cracking of Austenitic Stainless Steels", J. Nucl. Mater., **302**, 20-40, 2002

20. Busby, J. T., and G. S. Was, "Irradiation-Assisted Stress Corrosion Cracking in Model Alloys with Solute Additions," Proc. 11th Int. Symp. on Environmental Degradation of Materials in Nuclear Power Systems--Water Reactors, NACE, Houston, TX, pp. 995-1014, 2003.

21. Was, G. S., *Fundamentals of Radiation Materials Science – Metals and Alloys*, Springer, Berlin Heidelberg New York, 2007.

22. Watamane, T., "Approach to Grain Boundary Design for Strong and Ductile Polycrystals," Res. Mechanica: Inter. J. Struct. Mech. Mater. Sci., **11** No.1 (1984): 47.

23. Palumbo, G., E. M. LEHOCKEY, and P. LIN, "Applications for Grain Boundary Engineered Materials," JOM, **50** No.2 (1998): 40

24. Randle, V., "Twinning-Related Grain Boundary Engineering," Acta Materialia, **52** (2004): 4067

25. Electric Power Research Institute, "CIR II Program: Description of the Boris 6 and 7 Experiments in the BOR-60 Fast Breeder Reactor," Report No. 1011787, Palo Alto, CA, 2005.

26. Chen, Y., O. K. Chopra, W. K. Soppet, N. L. Dietz Rago, and W. J. Shack, "IASCC Behavior of Austenitic Stainless Steels and Alloy 690 form Halden Phase-II Irradiations," NUREG/CR-6965, ANL-07/11, 2008

27. Chen, Y., O. K. Chopra, W. K. Soppet, W. J. Shack, Y. Yang and T. Allen, "Cracking Behavior and Microstructure of Austenitic Stainless Steels and Alloy 690 Irradiated in BOR-60 Reactor, Phase I," ANL/09-32, 2007.

28. Hirth, J. P. and J. Lothe, *Theory of Dislocations*, 2nd Ed., Krieger Publishing Company, Malabar, FL, 1992.

29. Seeger, A., "The Mechanism of Glide and Work Hardening in Face-Centered Cubic and Hexagonal Close-Packed Metals," in *Dislocations and Mechanical Properties of Crystal,* New York, J. C. Fisher et al., Ed., Wiley and Sons Inc., 1957.

30. Makin, M. J., and F. Minter, "Irradiation Hardening in Copper and Nickel,"Acta Metallurgica, Vol. **8**, No. 10 (1961): 691.

31. Odette, G. R., and G. E. Lucas, "The Effects of Intermediate Temperature Irradiation on the Mechanical Behavior of 300-series Austenitic Stainless Steels," J. Nucl. Mater., **179-181** (1991): 572.

32. Chen, Y., Y. Yang, Y. Huang, T. Allen, B. Alexandreanu, and K. Natesan, "Void Swelling and Microstructure of Austenitic Stainless Steels Irradiated in the BOR-60 Reactor," NUREG/CR-7128, ANL-11/27, 2012.

33. Lucas, G. E., "Evolution of Mechanical Property Change in Irradiated Austenitic Stainless Steels," J. Nucl. Mater., **206** (1993): 287-305.

34. Garner, F. A., "Evolution of Microstructure in Face-Centered Cubic Metals during Irradiation," J. Nucl. Mater., **205** (1993): 98.

35. Garner, F. A., "Irradiation Performance of Cladding and Structural Steels in Liquid Metal Reactors," in *Materials Science and Technology - A Comprehensive Treatment*, R. W. Cahn, P. Haasen, and E. J. Kramer, eds., VCH Publishers Inc., New York, 1994.

36. Mills, W. J., "Fracture Toughness of Type 304 and 316 Stainless Steels and Their Welds," International Materials Reviews, **4** No.2 (1997): 45.

37. Bloom, E. E., and J. R. Weir Jr., "Effect of Neutron Irradiation on the Ductility of Austenitic Stainless Steel," Nucl. Tech., **16**, No. 1 (1972): 45.

38. Fukuya, K., K. Fujii, Y. Kitsunai, "Deformation Structure in 316 Stainless Steel Irradiated in a PWR," Proc. 12th Intl. Conf. on Environmental Degradation of Materials in Nuclear Power System – Water Reactors, Minerals, Metals, & Materials Society, 2005.

39. Farrell, K., T. S. Byun, and N. Hashimoto, "Deformation Mode Maps for Tensile Deformation of Neutron-Irradiated Structural Alloys," J. Nucl. Mater., **335** (2004): 471.

40. Karlsen, W., K. Dohi, and T. Onchi, "Observations if Channel Deformation in Mildly-Deformaed Low-dose 304L Austenitic Stainless Steel," 13th International Conference on Environmental Degradation of Materials in Nuclear Power Systems, Whistler, British Columbia, Aug. 19 - 23, 2007.

41. Luft, A., "Microstructural Processes of Plastic Instabilities in Strengthened Metals," Progress in Materials Science, **35** (1991): 97.

42. Chen, Y., O. K. Chopra, W. K. Soppet, N. L. Dietz Rago, and W. J. Shack, "IASCC Susceptibility of Austenitic Stainless Steels and Alloy 690 in High Dissolved Oxygen Water Environment," Proc. 13th Intl. Symp. on Environmental Degradation of Materials in Nuclear Power Systems - Water Reactors, 2007.

43. Chen, Y., A. S. Rao, B. Alexandreanu, and K. Natesan, "Slow Strain Rate Tensile Tests on Irradiated Austenitic Stainless Steels in Simulated Light Water Reactor," Transactions, SMiRT 21, Nov. 6-11, 2011, New Delhi, India.

44. Chen, Y., W. J. Shack, B. Alexandreanu, E. E. Gruber, and A. S. Rao, "Cracking Behavior of Irradiated Heat-Affected Zone Specimens of Type 304 and 304L Stainless Steel Welds in High-Purity Water," 14th Int. Conf. on Environmental Degradation of Materials in Nuclear Power Systems, Virginia Beach, VA, Aug. 23-27, 2009.

45. Chen, Y., O. K. Chopra, Y. Yang, W. J. Shack, B. Alexandreanu, E. E. Gruber, and A. S. Rao, "Crack Growth Behavior of Irradiated Type 316 SS in Low Dissolved Oxygen Environment," 15th Int. Conf. on Environmental Degradation of Materials in Nuclear Power Systems, TMS, 2011.

46. Jiao, Z., and G. S. Was, "Impact of Localized Deformation on IASCC in Austenitic Stainless Steels," J. Nucl. Mater., **408** (2011): 246.

47. Chen, Y., O. K. Chopra, Y. Yang, W. J. Shack, B. Alexandreanu, E. E. Gruber, and A. S. Rao, "Crack Growth Rates and Fracture Toughness of Neutron Irradiated Grain-Boundary-Engineered Austenitic Stainless Steels," 14th Int. Conf. on Environmental Degradation of Materials in Nuclear Power Systems, Virginia Beach, VA, Aug. 23-27, 2009.

48. Parkins, R. N., "Development of Strain-Rate Testing and Its Implications," ASTM-STP 665, ASTM 1977.

49. Ikeda, A., M. Ueda, and H. Okamoto, "The Role of Slow Strain Rate Testing on Evaluation of Corrosion Resistant Alloys for Hostile Hot Sour Gas Production," ASTM STP 1210, ASTM 1993.

50. Nishioka, H., K. Fukuya, K. Fujii, and T. Torimaru, "IASCC Properties and Mechanical Behavior of Stainless Steels Irradiated up to 73 dpa," Proc. 13th Intl. Symp. on Environmental Degradation of Materials in Nuclear Power Systems - Water Reactors, 2007.

51. Greenwood, L. R., "Neutron Interactions and Atomic Recoil Spectra," J. Nucl. Mater., **216** (1994): 29-44.

52. Simonen, E. P., D. J. Edwards, and S. M. Bruemmer, "Dose Rate Effects on Microchemistry and Microstructure Relevant to LWR Components," Proc. 12th Intl. Conf. on Environmental Degradation of Materials in Nuclear Power System – Water Reactors, Minerals, Metals, & Materials Society, 2005.

53. Edwards, D., E. Simonen, S. Bruemmer, "Radiation-Induced Segregation Behavior in Austenitic Stainless Steels: Fast Reactor versus Light Water Reactor Irradiations," Proc. 13th Intl. Symp. on Environmental Degradation of Materials in Nuclear Power Systems - Water Reactors, 2007.

Nuclear Engineering Division
Argonne National Laboratory
9700 South Case Avenue
Argonne, IL 60439

www.anl.gov

Argonne National Laboratory is a U.S. Department of Energy laboratory managed by UChicago Argonne, LLC